Universiteit Gent
Faculteit Wetenschappen
Vakgroep Subatomaire en Stralingsfysica

Gamow-Teller strength distributions in ^{64}Co and ^{64}Cu studied via the ^{64}Ni$(d,^2\mathrm{He})$ and ^{64}Ni$(^3\mathrm{He},t)$ reactions

Lucia-Ana Popescu

Thesis submitted for the degree of Doctor in Science: Physics
Academic year 2005 – 2006

Promotor: Prof. Dr. D. De Frenne
Co-promotor: Prof. Dr. E. Jacobs

Nederlandse Samenvatting

Ladingsuitwisselingsreacties (CE reacties) zijn belangrijke hulpmiddelen in de studie van spin-isospin excitaties in kernen. Voor intermediaire energie van de inkomende deeltjes en voor uiterst voorwaartse hoeken (dicht bij 0°) is de spin-isospin-flip centrale term van de effective nucleon-nucleon wisselwerking de dominante componente. Dit betekent dat de pieken die corresponderen met Gamow-Teller (GT) overgangen het spectrum zullen domineren bij die kleine hoeken. Wij hebben 2 CE reacties uitgevoerd op ^{64}Ni met als doel de GT overgangen ($\Delta L = 0$, $\Delta S = 1$, $\Delta T = 1, \Delta J^{\pi} = 1^{+}$) te bestuderen zowel in de β^{+} als β^{-} richting. Voor het onderzoek in de β^{+} richting werd gekozen voor de ^{64}Ni(d,^{2}He)^{64}Co reactie bestudeerd in het Kernfysisch Versneller Instituut (KVI), Groningen, gebruik makend van een 171 MeV deuteronen bundel. De uittredende ^{2}He deeltjes werden geanalyseerd met de "Big Byte Spectrometer" voorzien van de "EuroSuperNova" detector. De complementaire reactie, ^{64}Ni(^{3}He, t)^{64}Cu, werd onderzocht in het Research Center for Nuclear Physics (RCNP), Osaka. Daar werd een 420 MeV ^{3}He bundel gebruikt. De uittredende tritium deeltjes werden geanalyseerd met de "Grand Raiden Spectrometer" en de RCNP detector.

De bekomen resultaten zijn van belang voor verschillende onderzoeksdomeinen. Door de eenvoud van de GT overgangen zullen de bevestigde sterktes, $B(GT^{\pm})$, toelaten verschillende theoretische modellen te testen. In het geval van de ^{64}Ni(^{3}He, t)^{64}Cu reactie waren wij de eersten om de $B(GT^{-})$ distributie te bepalen. Sterktes naar individuele niveaus in ^{64}Co werden ook voor het eerst gegeven in dit werk. Vroegere studies die gebruik maakten van (n, p) reacties faalden hierin omdat de energie resolutie (FWHM $>$ 800 keV) onvoldoende was.

Omdat de bestudeerde kernen behoren tot het gebied van de fp-schil, hebben de bekomen $B(GT)$ waarden belangrijke implicaties voor astrofysica. Deze grootheden zijn nodig in b.v. theoretische berekeningen over de mate waarin electronenvangst plaatsvindt in het laatste stadium van een supernova explosie.

Naast de bepaling van de GT-overgangssterkte, werd belangrijke spectroscopische informatie bekomen voor zowel ^{64}Co als ^{64}Cu kernen. Dit is tewijten aan de zeer uitgeproken selectiviteit van de reacties en de zeer goede energieresolutie bekomen voor de 2 reacties: FWHM=110 keV voor ^{64}Ni(d,^{2}He)^{64}Co en FWHM=35 keV in het geval van ^{64}Ni(^{3}He, t)^{64}Cu. Toestanden gelegen in het excitatiegebied dat gekenmerkt is door een grote niveaudichtheid, konden voor het eerst worden onderscheiden. Gebaseerd op de selectiviteit van de reactie en een hoekdisitributie analyse, die toeliet het L karakter van de straling te bepalen, kon op die manier de informatie gekend in de literatuur vervolledigd of bevestigd worden.

Eerdere (d,^{2}He) en (^{3}He, t) reacties, uitgevoerd bij vergelijkbare energieën, hebben aangetoond dat de werkzame doorsnede bij 0° proportioneel is met de GT overgangssterkte voor de twee CE reacties die we bestudeerd hebben. Maar de experimentele bepaling van de proportionaliteitsfactor, ook eenheids-werkzame doorsnede genaamd, is niet altijd mogelijk, aangezien dat alleen kan als de $B(GT)$ waarde van een sterke overgang goed gekend is. Beide reacties ^{64}Ni(d,^{2}He)^{64}Co en ^{64}Ni(^{3}He, t)^{64}Cu hebben het voordeel dat er een absolute calibratie kan uitgevoerd worden: beide overgangen, van ^{64}Co g.s. en van ^{64}Cu g.s., zijn toegelaten overgangen waarvan de logft goed gekend is [Fir96]. Daarom kunnen de $B(GT)$s voor deze overgangen berekend worden met een grote precisie, zodat we direct de eenheids-werkzame doorsnede kunnen meten. Deze waarden kunnen dan als standaard gebruikt worden in het gebied van de fp-schil.

Daar we in onze studie de GT distributies startend van de grondtoestand van ^{64}Ni zowel in de β^- als β^+ richting hebben bepaald, kan de model-onafhankelijke Ikeda somregel worden geverifieerd [Ike63]. Die somregel zegt dat het verschil tussen de gesommeerde sterktes in de β^- en β^+ richting gelijk moet zijn aan S_{β^-} - S_{β^+} = 3(N-Z). De op die manier voorspelde totale sterkte werd niet teruggevonden in onze experimenten. Het ontbreken van sterkte (de zogenaamde quenching) is een bekend fenomeen. Maar de vorige experimenten suggereerden dat door deze quenching ongeveer 60% [Ost92] van de sterkte zou teruggevonden worden terwijl wij slechts 29% terug vinden in onze studie. Een mogelijke verklaring voor dat quenching fenomeen is gegeven door Arima [Ari99]. Door de koppeling van 2deeltjes-2gat (2p-2h) excitaties tot de GT mode, kan een gedeelte van de sterkte verschoven zijn naar hogere excitatieënergieën. Een onderzoek bij deze hogere excitatieënergieën, tot ongeveer 50 MeV, kan meer informatie opleveren. Daar echter de vorm en de amplitude van de continue achtergrondstraling bij hogere energieën nog steeds een onderwerp van studie is, blijft de experimentele bepaling van de

GT sterkte in dat gebied en daardoor ook de totale sterkte nog steeds een probleem.

Naast de studie van de sterkte van GT overgangen naar ^{64}Co en ^{64}Cu, zijn de experimenten die voorgesteld worden in dit werk een onderdeel van de studie van Isobare Analoge Toestanden (IAS) in de ^{64}Co - ^{64}Ni - ^{64}Cu kernen aangeslagen in de (d,^{2}He) CE reactie, de (p, p') inelastische verstrooiing (IE) reactie en de (^{3}He, t) CE reactie op ^{64}Ni. Omdat het excitatie kwantum isospin $\tau = 1$ heeft, met projectie $\mu_\tau = 0, \pm 1$, kunnen toestanden met 3 verschillende isospin waarden worden geëxciteerd in die reacties: T = $T_0 - 1$, T_0, $T_0 + 1$, waarbij T_0 de isospin is van de g.s. van ^{64}Ni. Daar de isospin van de ^{64}Co g.s. $T_0 + 1$ is kunnen enkel de toestanden met T = $T_0 + 1$ worden aangeslagen in ^{64}Co in de reactie ^{64}Ni(d,^{2}He)^{64}Co. Analoog, kunnen toestanden met T = T_0 en $T_0 + 1$, worden aangeslagen in de ^{64}Ni(p, p') reactie. Daar T = $T_0 - 1$ voor de g.s. van ^{64}Cu worden de 3 isospin componenten aangeslagen in de ^{64}Ni(^{3}He, t)^{64}Cu reactie. De toestanden die gekenmerkt worden door dezelfde isospin, maar die in verschillende kernen optreden noemt men Isobare Analoge Toestanden; ze moeten optreden bij dezelfde excitatieënergie in de verschillende kernen, nadat gecorrigeerd werd voor het verschil in Coulomb energie. De intensiteiten van de overgangen van ^{64}Ni naar de IAS's in ^{64}Co, ^{64}Ni en ^{64}Cu worden bepaald door de isospin Clebsch-Gordon coëfficiënten. De verschillende isospin componenten worden op een verschillende manier aangeslagen in de verschillende reacties. Het relatief grote neutronenoverschot brengt mee dat elk van de hogervermelde reacties slechts bruikbaar is voor het onderzoek van de laagste isospin componente aangeslagen in iedere respectievelijke reactie. Daarom zijn alle 3 de reacties nodig voor een complete studie van spin-isospin overgangen uitgaande van ^{64}Ni g.s.

De spin en spin-isopin excitaties (M1) van T = T_0 en $T_0 + 1$ toestanden in ^{64}Ni zullen bestudeerd worden via de reactie ^{64}Ni(p, p'). Daarbij zijn metingen bij extreem voorwaartse hoeken absoluut noodzakelijk voor de bepaling van de M1 overgangssterktes. Door de typische problemen bij (p, p') metingen bij 0° zijn er maar enkele faciliteiten in de wereld waar dergelijke metingen kunnen uitgevoerd worden. Wij hebben een zeer succesvolle testmeting uitgevoerd by E_p = 300 MeV in RCNP (Osaka-Japan). Bovendien hebben we heel wat vooruitgang geboekt in een testmeting by E_p = 220 MeV in iThemba LABS (Kaapstad-Zuid Afrika). We hebben er alle vertrouwen in dat ook hier zeer binnekort (p, p') metingen zullen kunnen uitgevoerd worden bij 0°.

In dit werk geven we enkele suggesties voor de identificatie van IAS toestanden van ^{64}Ni in ^{64}Cu gebaseerd op onze experimentele (^{3}He, t) resultaten voorgesteld in deze thesis. Een nauwkeurige identificatie van de T = T_0 en

$T_0 + 1$ toestanden kan slechts gegeven worden door de resultaten van de ^{64}Ni(^{3}He, t)^{64}Cu en ^{64}Ni(p, p')^{64}Ni spectra van de testmeting te vergelijken. Een vorig ^{64}Ni(p, p')^{64}Ni experiment, uitgevoerd bij een verstrooiingshoek van 4° door de groep van Marty et al. [Mar83] suggereerde dat de eerste T=5 toestand in ^{64}Ni (IAS van ^{64}Co g.s.) zich bevindt bij 15.62 MeV. Dit resultaat wordt bevestigd door onze 0° meting in RCNP. De 15.62 MeV toestand is heel duidelijk te zien, als een sterk aangeslagen toestand op de top van de dipool reuzenresonantie in ^{64}Ni. Daar de IAS van ^{64}Ni g.s. in ^{64}Cu zich bevindt bij 6.826 MeV, verwacht men de overgangen naar de T = $T_0 + 1$ toestanden in ^{64}Cu in het energiegebied $E_x \geq 22.4$ MeV. In de huidige ^{64}Cu(^{3}He, t) spectra werd geen aanduiding gevonden van de IAS van ^{64}Co g.s. Dit is in overeenstemming met de verwachte zeer zwakke intensiteit van die overgang: volgens de isospin CG coëfficiënten zou slechts 2% van de totale GT sterkte in ^{64}Cu terug te vinden zijn in die overgangen naar de T = $T_0 + 1$ niveaus. Dit is de reden waarom de IAS van ^{64}Co g.s. verscholen zit in de continue achtergrond.

Een analoge studie werd reeds uitgevoerd door H. Fujita voor ^{58}Ni [Fuj01a], door de metingen van ^{58}Ni(^{3}He, t) uitgevoerd in RCNP [Fuj01a, Fuj02b], te combineren met de ^{58}Ni(p, p') metingen bij 0° in IUCF [Fuj01a] en de ^{58}Ni(d,^{2}He) metingen in het KVI-Groningen [Hag01, Hag05].

De studie van de IAS toestanden zal uitgebreid worden tot andere Ni isotopen om de systematische energiespreiding tussen de verschillende isospin componenten te begrijpen alsook hun relatieve intensiteiten. Met deze bedoeling hebben we de ^{60,62}Ni(^{3}He, t) reactie bestudeerd in RCNP. De analyse van de data is nog bezig. Ook ^{60,62}Ni(p, p') metingen zijn gepland in de nabije toekomst. Deze gegevens moeten verder gecombineerd worden met ^{60,62}Ni(d,^{2}He) data.

Contents

Chapter 1

Introduction

The spin- and isospin-flip excitations in which nucleons and their spins are collectively excited are modes of nuclear vibration. A schematic picture of these modes in the frame of the hydrodynamical model is given in fig. 1 [MK94]. The vibrational modes characterized by no change in isospin ($\Delta\ T = 0$) are called *isoscalar* and those for which $\Delta\ T = 1$ are called *isovector*. In the *isoscalar* modes (fig. 1 *a*) and *c*)) the protons and neutrons are moving in phase and in the *isovector* modes (fig. 1 *b*) and *d*)) in opposite phase. Similar oscillations appear in the spin space: the nucleons with spin up and down can move either in phase (fig. 1 *a*) and *b*): $\Delta\ S = 0$ - the *spin-scalar* modes), or in opposite phase (fig. 1 *c*) and *d*): $\Delta\ S = 1$ - the *spin-vector* modes, called also *spin-flip* excitations). Furthermore, the vibrations can be characterized by the angular momentum transfer during the excitation: the *monopole* modes (with no angular momentum transfer $\Delta\ L = 0$), *dipole* modes ($\Delta\ L = 1$), *quadrupole* modes ($\Delta\ L = 2$)...

Understanding the modes of nuclear vibration provides valuable information, not only in nuclear structure physics, but also in astrophysics and neutrino physics [Ost92, Rap94, Ful80]. An investigation of these resonances in the particular case of ^{64}Co and ^{64}Cu nuclei represents the topic of the study presented in this thesis. We are especially interested in the $0\hbar\omega$ *monopole isovector spin-flip* modes ($\Delta\ L = 0$, $\Delta\ T = 1$, $\Delta\ S = 1$). These are 1^+ excitations usually known from β-decay as allowed Gamow-Teller (GT) transitions. Their study provides important nuclear structure information as their reduced matrix elements, $B(GT)$'s, directly show the relation between the quantum states of neutrons and protons in nuclei. Due to the simple structure of these

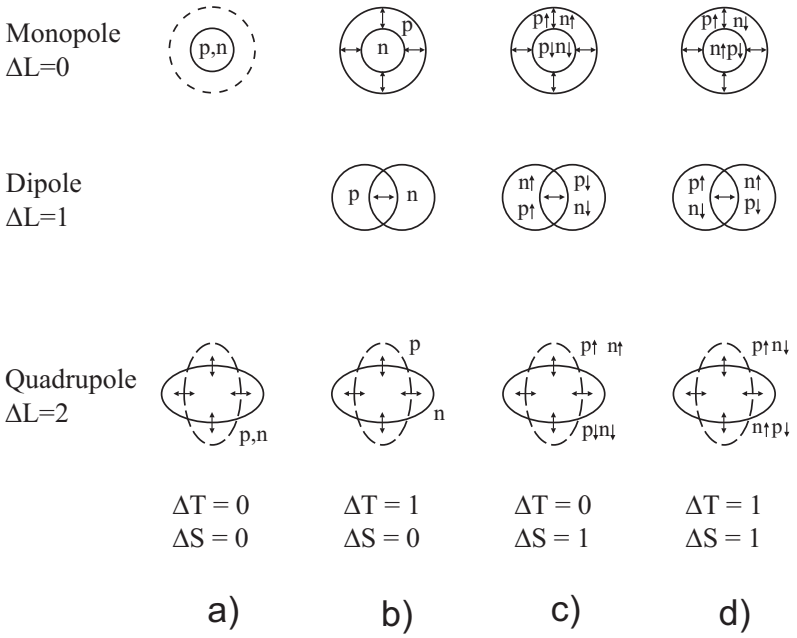

Figure 1.1 Schematic representation of different vibrational modes in the hydrodynamical model. Picture taken from [MK94].

resonances, their experimental study gives a very good opportunity for testing different theoretical models, like, e.g., those developed in the framework of the shell model. There are also astrophysical implications of the study as these matrix elements allow to determine the rates of electron capture processes that appear in a certain stage of supernova explosions. Concerning the implications in neutrino physics, the neutrino detection is based on the absorption of neutrinos by nuclei through GT transitions; therefore the GT matrix elements for specific nuclei are fundamental quantities for determining the detection efficiency of (solar) neutrinos.

Three types of interaction can mediate these nuclear vibrations: the weak, the strong and the electromagnetic interaction. The dominant force acting between nucleons is the strong interaction, but also the weak and the elecromagnetic interactions contribute in determining the properties of nuclei. Field theory explains the interaction between two particles by the exchange of a field quantum between them. The field quanta involved in each of these three types of interaction are different. For the case of two nucleons strongly interacting with each other the field quantum is the meson. A photon is exchanged in the electromagnetic interaction and a W^+, W^- or Z^0 boson in the weak interaction. The mass of the exchanged quanta determine the range of the interaction. The photon has no mass and, as a consequence, the electromagnetic interaction has an infinite range. In contrast, the bosons exchanged in the weak interaction have a very large mass (the rest mass energy is $\sim$ 100 GeV, while the rest-mass of nucleons, e.g., is $\sim$ 1 GeV), therefore the weak interaction has a short range.

In the case of *the weak interaction* the axial-vector component of the interaction couples to the spin of the nucleon and induces the GT transitions of nuclear β-decay. Because the present work is dedicated to spin-isospin-flip transitions in the A=64: Co-Ni-Cu system, we will briefly present as an example the β-decay of these nuclei (see also fig. 1.2):

$$^{64}Co \longrightarrow ^{64} Ni + e^- + \overline{\nu_e} \tag{1.1}$$

and

$$^{64}Cu \longrightarrow ^{64} Ni + e^+ + \nu_e \tag{1.2}$$

The first case is a β^- transition, in which a proton is changed into a neutron and an electron and an antineutrino are emitted. The second case corresponds to a β^+ transition: a neutron is changed into a proton and a positron and a

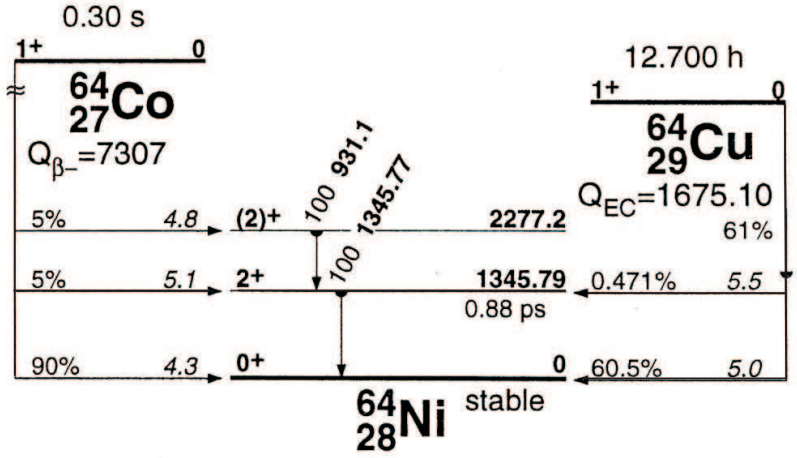

Figure 1.2 The A=64: Co, Ni and Cu system. The logft values together with the branching ratios for the β transitions are indicated. Figure taken from ref. [Fir96].

neutrino are emitted in this process. These transitions are mediated by the spin-isospin operator $g_A \sigma \tau_{\pm}$, with g_A - the axial-vector coupling constant.

The investigation of GT excitations via β-decay is however limited by the Q-value to a narrow low energy region, missing the main part of the giant GT resonance predicted by Ikeda, Fuji and Fujita [Ike63] in 1963. Therefore probes that allow the independent variation of energy and momentum transfer to the target are needed. Hadronic probes like (p, n) or (n, p) charge-exchange (CE) reactions can do so. Also the inelastic scattering (IE) reactions can be used for this purpose.

The interaction involved in CE and IE hadronic reactions is mediated by the strong forces. Due to the structure of the spin and isospin of the nucleon, *the strong interaction* has several components allowing the investigation of different types of nuclear excitations. In terms of the field theory, the π- and ρ-mesons are the exchanged quanta generating the spin-isospin dependent interaction terms. However, the CE and IE reactions can be connected to β-decay only if the GT cross section is measured at very small momentum transfer $\mathbf{q}$, as the allowed β decay takes place at $\mathbf{q}$=0. In these reactions the exchanged quantum between the projectile nucleus and target nucleus,

that excites the nuclear spin-isospin degrees of freedom at small momentum transfers, is the π-meson; this one has a small mass and therefore can be exchanged over large distances. Even in the early '80's there were several (p,n) experiments [And80, Goo80, Gaa81], performed at E_p=200 MeV, at the Indiana Cyclotron Facility (IUCF) showing the existence of the giant GT resonance predicted by Ikeda, Fuji and Fujita [Ike63]. It was impossible to study these GT resonances via β-decay.

The third possibility to excite the isovector spin-flip vibrational modes is by using *the electromagnetic interaction*. For understanding the spin-isospin oscillations mediated by the electromagnetic interaction, we should note that the spin of the nucleon has an associated magnetic moment (μ_p = 2.79 for the proton and μ_n = -1.91 for the neutron) so it can interact through the electromagnetic field. The coupling between the electromagnetic field and the spin of the nucleon is mediated by the nuclear magnetization current, having an isoscalar part proportional to $(\mu_p + \mu_n)$ $[\boldsymbol{\sigma} \times \mathbf{q}]^{(1)}$ and an isovector part proportional to $(\mu_p - \mu_n)$ $[\boldsymbol{\sigma} \times \mathbf{q}]^{(1)}\tau_3$, where $\mathbf{q}$ is the momentum transfer. As $(\mu_p - \mu_n) = 4.71$ is much larger than $(\mu_p + \mu_n) = 0.88$, the electromagnetic interaction favor the spin-isospin excitations. The momentum transfer $\mathbf{q}$ and the spin operator σ couple transversally, therefore a very good probe for this study are the backward-angle inelastic electron scattering experiments.

As already mentioned, the aim of the present study is an investigation of the GT modes in ^{64}Co and ^{64}Cu excited in the $(d,^2\mathrm{He})$ and $(^3\mathrm{He},t)$ CE reactions starting from the gs of ^{64}Ni. These reactions are of the (n,p)- and (p,n)-type and they show several advantages over basic (n,p) and (p,n) reactions. The main advantage is the better energy resolution due to the acceleration and detection of charged particles. A more detailed discussion will be given in Chapter 2.

The best facilities available at the moment have been chosen for these experiments. The ^{64}Ni$(d,^2\mathrm{He})^{64}$Co reaction was studied at the *Kernfysisch Versneller Instituut* (KVI), Groningen, with a 171 MeV deuteron beam, using the *Big-Bite Spectrometer* and the *EuroSuperNova detector* (see section 4.1 for details). An energy resolution of about 110 keV was achieved. The *Research Center for Nuclear Physics* (RCNP), Osaka, was the best place to perform the ^{64}Ni$(^3\mathrm{He},t)^{64}$Cu experiment. A 420 MeV ^{3}He beam was used and the tritium particles were analyzed with the *Grand Raiden Spectrometer* and the RCNP detector (see section 4.2 for details). An energy resolution of about 35 keV characterizes the obtained ^{64}Cu spectrum.

Several physical aspects where motivating the start of our study:

• It will be discussed in Chapter 2 that the cross section of these CE reactions becomes proportional to the transition strength, $B(GT)$, at zero momentum transfer. The proportionality factor, called "unit cross section", is mass and reaction dependent and it was determined for several nuclei measured in (d,^{2}He) and (^{3}He,t) experiments. As the unit cross section cannot be directly measured for every nucleus, but only for those cases where the $B(GT)$ of a strong well identified transition is already known, it is ideal to determine its evolution with the mass number for both CE reactions mentioned above. Both transitions, from ^{64}Co g.s. and ^{64}Cu g.s. to ^{64}Ni g.s., are allowed β transitions with logft-values of respectively 4.3 and 5.0, measured with good precision in β-decay studies [Fir96] (see fig. 1.2). Therefore the present study will give good calibration values allowing a more accurate determination of the mass dependence of the unit cross section both for β^+ (the (d,^{2}He) reaction) and β^- direction (the (^{3}He,t) reaction).

• Due to the high energy resolution achieved in the two experiments and based on the absolute calibration from β-decay results, the GT strength distribution in ^{64}Co and ^{64}Cu can be determined with good precision. By combining the two experimental results, the Ikeda sum rule can be checked. According to this sum rule, the difference in the summed strengths in the β^- (the (^{3}He,t) measurement) and the β^+ (the (d,^{2}He) measurement) direction should be equal to 3(N-Z) = 24 $B(GT)$ units.

• The present study will increase substantially the spectroscopic information about the mass 64 nuclei. The existent information on the level scheme of ^{64}Co is scarce. Only a few levels in the energy region below 2.05 MeV are known and apart from the g.s. no J^π assignments. The information obtained in the different studies up to now is also contradictory. The present (d,^{2}He) measurement intend to elucidate and complete it. For levels in ^{64}Cu several J^π assignments can be given, by using the high energy resolution and selectivity of the present (^{3}He,t) zero degree measurement.

• The existence of the isobaric analogue states (IAS's) is a proof of the symmetry in nuclear force. The study of the IAS's in ^{64}Co - ^{64}Ni - ^{64}Cu nuclei is another aspect of the present work. These are states in the three different nuclei which have similar properties. The existence and properties of IAS's will be discussed in Chapter 2. Symmetry is also expected among transitions for which the initial or final states are replaced by IAS's. These analogue transitions should idealy have the same energy (correcting the excitation energy of the states for the Coulomb displacement) and corresponding

strength. Therefore the IAS's can be investigated by comparing the energies and the strengths of analogous transitions. This comparison is easier if one considers a transition which selects a specific J^π value, like, e.g., the GT transitions for which $\Delta\ J^\pi = 1^+$. A complete picture of IAS's in ^{64}Co - ^{64}Ni - ^{64}Cu nuclei will be given when combining the information obtained in the present CE experiments with the one from an IE (p, p') experiment on ^{64}Ni, measuring the analogue of GT transitions (the M1 excitations) in ^{64}Ni. (p, p') test runs at 0° have been performed at RCNP and iThemba Labs (Cape Town), further experiments being scheduled for the near future.

• From the point of view of the astrophysics there is a tremendous interest in fp-shell nuclei. ^{64}Co, ^{64}Ni and ^{64}Cu are fp-shell nuclei. The $B(GT)$ distribution in ^{64}Co measured in the $(d,^2\mathrm{He})$ experiment serves as input for theoretical calculations. These strengths are directly connected to the electron capture rates of the weak-interaction processes which play an essential role in the early stage of the collapse of supernovae [Cau99a, Lan00, Lan01]. Nowadays several research groups are investigating the birth, the life and the death of stars.

Motivated by the present $^{64}\mathrm{Ni}(^3\mathrm{He}, t)^{64}\mathrm{Cu}$ experiment, the double β-decay study of ^{64}Zn to ^{64}Ni was initiated by the Münster group within the EuroSuperNova Collaboration [ea]. With this aim, the complementary $^{64}\mathrm{Zn}(d,^2\mathrm{He})^{64}\mathrm{Cu}$ experiment was later performed at KVI.

The structure of the thesis is the following: After this introductory chapter, the second chapter gives a general description of CE and IE scattering reactions and describes more in detail the $(d,^2\mathrm{He})$ and $(^3\mathrm{He}, t)$ reactions used in this work. The third chapter discusses the isovector spin-flip collective excitations (known as "giant resonances") that can be present in the measured ^{64}Co and ^{64}Cu spectra. Details about the quasi-free scattering continuum region are also included. The experimental set-ups for the two experiments are discussed in the fourth chapter. Chapter 5 will present the analysis procedure and results of the $^{64}\mathrm{Ni}(d,^2\mathrm{He})^{64}\mathrm{Co}$ measurement. This chapter includes also a discussion of the experimental results obtained with this reaction. The analysis procedure and results of the $^{64}\mathrm{Ni}(^3\mathrm{He}, t)^{64}\mathrm{Cu}$ measurement together with a discussion of the obtained results is given in Chapter 6. The last chapter deals with a discussion of the combined experimental results. The expected further developments are also discussed here.

Chapter 2

Charge-exchange reactions

Similar to β-decay, the CE reactions replace a proton in a nucleus by a neutron (the inverse reaction of β^- decay) or a neutron by a proton (the inverse of β^+ decay) (see fig. 2.1). Although the charge exchange processes involve strong interactions, the matrix elements that enter into the reaction rates are the same as in the case of the β-decay mediated by the weak interactions. The main advantage over β-decay is that the obtainable information is not limited by the Q-value to lower energy final states: a complete picture of the spin-isospin transitions up to high excitation energies can be given.

The simplest CE reactions are the (p,n) and (n,p) reactions. The (p,n) reaction is complementary to β^- decay:

$$p + {}^{A}_{Z}X_N \longrightarrow {}^{A}_{Z+1}Y_{N-1} + n$$

while the (n,p) reaction is complementary to β^+ decay:

$$n + {}^{A}_{Z}X_N \longrightarrow {}^{A}_{Z-1}Y_{N+1} + p$$

These are the most direct and simple CE reactions exciting GT states in nuclei, but they are burden by the disadvantage of the chargeless character of neutrons making them difficult to be detected with good resolution and efficiency (nowadays, the energy resolution that characterizes (p,n) spectra being around FWHM = 200 keV) and difficult to be delivered in a beam with good intensity and good energy resolution. Usually n-beams are secondary beams, produced in charged particle induced reactions and the resolution obtained in (n,p) spectra is FWHM $\geq$ 800keV.

As indicated in fig. 2.1, GT transitions can be induced also via other (p,n)- or (n,p) -type reactions.

The $({}^3\mathrm{He},t)$ is an alternative for the (p,n) reaction. At the moment, the most competitive facility in the world for performing $({}^3\mathrm{He},t)$ reactions is the

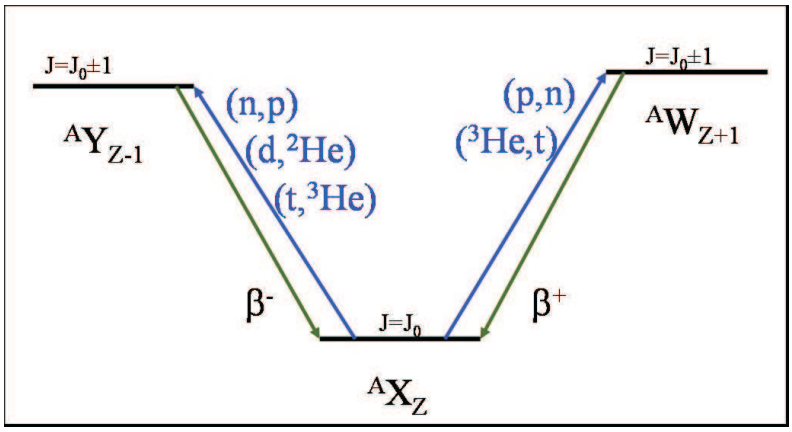

Figure 2.1 Schematic drawing of GT transitions between ground states either via β-decay, or via different CE reactions.

Ring cyclotron combined with the WS course beam line and the Grand Raiden Spectrometer in RCNP, Osaka. The energy resolution obtained in the $(^3\mathrm{He}, t)$ spectra measured at RCNP and discussed in this thesis is FWHM $\sim$ 35 keV.

The $(t,^3He)$ and $(d,^2\mathrm{He})$ are (n,p) -type reactions. Tritium beams are not commonly used, because of the radiation safety problems associated with the use of tritium. $(d,^2\mathrm{He})$ is the most suitable (n,p)-type reaction for studying GT transitions. Compared to (n,p), the use of a primary beam results in a considerable improvement of the energy resolution (FWHM $\sim$ 110keV for the $(d,^2\mathrm{He})$ spectra measured at the KVI, Groningen, and discussed in this thesis). Besides, the $(d,^2\mathrm{He})$ reaction is a very good filter for spin-isospin-flip excitations, as the deuteron is mainly in a triplet state $^3S_1$, with $S = 1$ and $T = 0$, and the detected ^{2}He is in a singlet state $^1S_0$, with $S = 0$ and $T = 1$ (see fig. 2.4). This is mainly the case when the relative energy of the two protons is smaller than 1 MeV, in which case only a few % of the higher order configurations are contributing [Rak02, Kox93]. But from the experimental point of view there are several difficulties in using this reaction. First of all it requires a complicated detection system, as the ^{2}He is unbound and the two protons have to be detected at the same moment in the focal plane of the spectrometer. This coincidence detection is done in the presence of a huge proton background from the break-up reactions of the incoming deuterons. Indeed the cross section of the break-up processes is several orders of magnitude larger than the one of the $(d,^2\mathrm{He})$ reaction at zero degrees. Therefore a performant acquisition system, which already makes an on-line

selection of the "good" events, is required. Furthermore the data analysis procedure should take care of the track reconstruction, background subtraction and efficiency corrections.

2.1 Schematic description of the one-step scattering reaction. The nucleon-nucleon effective interaction

The transition of the scattering system from the initial to the final reaction channel is described by the transition matrix element [Sat83]. The transition amplitude for the transition of the system from an initial to a final state under the action of an operator $\mathcal{T}$ is given by:

$$\mathcal{T}_{fi} = \langle \mathbf{k}_f, \mathrm{J}_f \mathrm{M}_f, \frac{1}{2} m_f | \mathcal{T} | \mathbf{k}_i, \mathrm{J}_i \mathrm{M}_i, \frac{1}{2} m_i \rangle \tag{2.1}$$

where $\mathbf{k}_i$ and $\mathbf{k}_f$ are the projectile momenta before and after reaction, J and M represent the total angular momentum and projection quantum numbers of the target, m is the spin projection of the projectile or ejectile with intrinsic spin $\frac{1}{2}$ and $\mathcal{T}$ represents the interaction mediating the transition from the initial state $|\Psi_i\rangle$ to the final state $|\Psi_f\rangle$. As only (p,n) and (n,p) type reactions are considered, only one nucleon in the total projectile interacts with the target. The transition amplitude can be related to the scattering amplitude [Ost91]:

$$\mathcal{M}_{fi} = -\frac{\mu}{2\pi\hbar^2} \sqrt{\frac{k_f}{k_i}}\ \mathcal{T}_{fi} \tag{2.2}$$

with μ the reduced mass (for CE and IE reactions $\mu_i{=}\mu_f{=}\mu$). From the scattering amplitude the reaction differential cross section can be calculated. For an unpolarized projectile and an unpolarized target, the reaction cross section will be function of the scattering angle θ between $\mathbf{k}_i$ and $\mathbf{k}_f$:

$$\begin{aligned} \frac{d\sigma(\theta)}{d\Omega} &= \frac{1}{2(2J_i+1)} \sum_{M_f M_i m_f m_i} |\langle J_f M_f, \frac{1}{2} m_f | \mathcal{M} | J_i M_i, \frac{1}{2} m_i \rangle|^2 \\ &= \Big[\frac{\mu}{2\pi\hbar^2}\Big]^2\ \frac{k_f}{k_i}\ \frac{1}{2(2J_i+1)} \sum_{M_f M_i m_f m_i} |\ \mathcal{T}_{M_f M_i m_f m_i}\ |^2 \end{aligned} \tag{2.3}$$

The transition operator, $\mathcal{T}$ is, in general, a very complicated many-body operator that contains information on the nuclear structure as well as on the reaction mechanism and cannot be fully calculated. Therefore, when performing CE reactions, it is very important to find those conditions that simplify the transition operator and favor the specific information on the nuclear structure that is of interest.

Reactions performed at low incident energies have, in general, a multi-step nature, but at incident energies above 100 MeV per nucleon the reaction mechanism is preferentially of a direct (one-step) nature [Ost92]. This simplifies the transition operator and the transition between initial and final states in a CE reaction can be evaluated in an effective interaction between the projectile nucleon p and the nucleons j in the target t:

$$V_{pt} = \sum_{j=1}^{A} V_{pj} \tag{2.4}$$

V_{pj} represents the bare nucleon-nucleon (NN) effective interaction.

The approximation in which the incident nucleon interacts with only one nucleon in the target, without interacting with the others, is known as the Impulse Approximation (IA).

But, in general, the interaction V_{pt} has large matrix elements, describing the relative motion of projectile and target before and after scattering. Their effects can be included to infinite order in the calculations by inserting these potentials into the corresponding one-body Schrödinger equation that generates the projectile scattering wave functions in the elastic and inelastic channels, leading to the Distorted Wave Approximation (DWA). The transition amplitude is now expressed as:

$$\mathcal{T}_{fi}^{DW} = \langle \chi^{(-)}, \Psi_f | \sum_{j=1}^{A} V_{pj} | \chi^{(+)}, \Psi_i \rangle, \tag{2.5}$$

where the $|\chi^{\pm}\rangle$ are the distorted incoming and outgoing waves, $|\Psi_i\rangle$ and $|\Psi_f\rangle$ are the wave functions of the initial and final states of the target nucleus.

The equation 2.5 assumes distinguishability between the projectile nucleon and the nucleons in the target. Therefore the knockout exchange amplitudes have to be included by replacing V_{pj} with $V_{pj}(1 - \mathcal{P}_{pj})$, where $\mathcal{P}_{pj}$ is the operator that exchanges the incident projectile p with the j^{th} nucleon in the target nucleus. Although this leads to a nonlocal effective interaction, for high incident energies the operator can be approximated by a local form [Pet86]

and the transition amplitude can be factorized into a nuclear structure part and a nuclear reaction part (for details see refs. [Sat83, Pet86, Ost91]).

If the distorted incoming, $\chi^{(+)}$, and outgoing, $\chi^{(-)}$, waves from eq. 2.5 are replaced by plane waves, the Plane Wave Approximation (PWA) is obtained. In this approximation the transition amplitude has the form:

$$\mathcal{T}_{fi}^{PW}(\mathbf{q}) = V(\mathbf{q})\rho_{J_f J_i}(\mathbf{q}), \tag{2.6}$$

with $\mathbf{q} = \mathbf{k}_f - \mathbf{k}_i$ the momentum transfer between the incoming projectile and the outgoing ejectile and $\rho_{J_f J_i}$ represents the transition density defined as:

$$\rho_{J_f J_i} = \langle J_f M_f | \sum_{j=1}^{A} \delta(\mathbf{r} - \mathbf{r}_j) | J_i M_i \rangle$$

where $\mathbf{r} - \mathbf{r}_j$ is the relative distance between the projectile nucleon and the target nucleon j.

In order to extract the nuclear structure information from the transition amplitude, $\mathcal{T}_{fi}$, the effective interaction, V_{pj}, has to be known. The structure of the transition amplitude in this single-scattering-approximation is essentially the same for different probes. Still, there are important differences among the probes due to the dynamic and symmetry properties of the different couplings V_{pj}, but also due to the fact that the distortion will depend on the characteristics of the probe [Pet80, Pet81].

According to Petrovich et al. [Pet81], the simplest complete interaction that is consistent with the free NN scattering amplitude must contain both spin-independent and spin-dependent central terms, non-central tensor terms and spin-orbit terms.

$$\begin{aligned} V_{NN} \;=\; & V_0^C(r) + V_\tau^C(r)\boldsymbol{\tau}_1 \cdot \boldsymbol{\tau}_2 + V_\sigma^C(r)\boldsymbol{\sigma}_1 \cdot \boldsymbol{\sigma}_2 + V_{\sigma\tau}^C(r)\boldsymbol{\sigma}_1 \cdot \boldsymbol{\sigma}_2 \boldsymbol{\tau}_1 \cdot \boldsymbol{\tau}_2 \\ & + [V_0^T(r) + V_\tau^T(r)\boldsymbol{\tau}_1 \cdot \boldsymbol{\tau}_2]\mathbf{S}_{12} \\ & + [V_0^{LS}(r) + V_\tau^{LS}(r)\boldsymbol{\tau}_1 \cdot \boldsymbol{\tau}_2]\mathbf{L}_{12} \cdot (\boldsymbol{\sigma}_1 + \boldsymbol{\sigma}_2) \end{aligned} \tag{2.7}$$

where r is the relative distance between the projectile and target nucleon. $\boldsymbol{\tau_1}$ and $\boldsymbol{\sigma_1}$ represents the tensor and spin operators for the projectile nucleon and $\boldsymbol{\tau_2}$ and $\boldsymbol{\sigma_2}$ those of the target nucleon. The C, T and LS notations have been introduced to mark the central, tensor and spin-orbit components, respectively. The $\boldsymbol{S}_{12}$ and $\boldsymbol{L}_{12}$ are the usual tensor and angular momentum operators between the projectile and target nucleons [Ber77]. This formula can

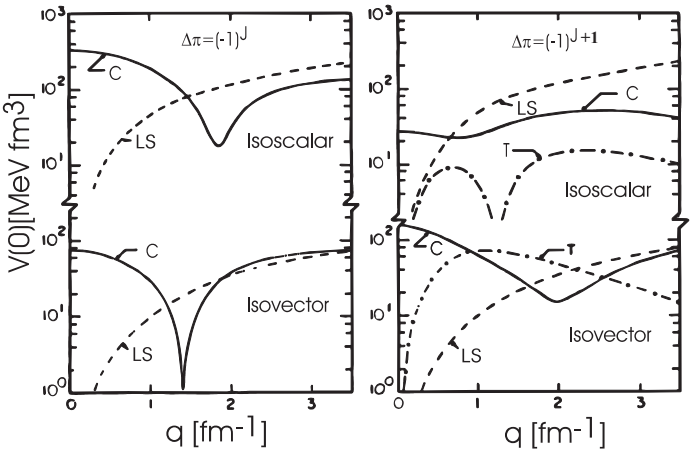

Figure 2.2 The nucleon-nucleon effective interaction components for the scattering of a proton beam at 135 MeV as a function of the momentum transfer. C, T and LS represents the central, the tensor and the spin-orbit parts, respectively. Picture taken from [Pet81].

be used for describing the spin-isospin-flip processes. The terms that contains the operators $\boldsymbol{\sigma}_1 \cdot \boldsymbol{\sigma}_2$, $\boldsymbol{\sigma}_1 + \boldsymbol{\sigma}_2$ or $\mathbf{S}_{12}$ (the spin operators) describe the spin-flip transitions, while the terms that contain the operator $\boldsymbol{\tau}_1 \cdot \boldsymbol{\tau}_2$ (the isospin operator) describe the isospin-flip transitions.

Figure 2.2 shows the results of the calculations performed by Petrovich and Love [Pet81] for the case of the (p, n) reaction at $E_p = 135$ MeV. The considerations are restricted to $0^+ \rightarrow J^\pi$ transitions. The left pannel presents the case of natural parity transitions $[\Delta\pi = (-1)^J]$. In this case $L = J$ and S=0,1. The right pannel presents the case of unnatural parity transitions $[\Delta\pi = (-1)^{J+1}]$. In this case $L = J \pm 1$ and S=1. The later one is the case of GT transitions in CE and IE reactions. The decomposition of the complete interaction into central, tensor and spin-orbit components as function of the momentum transfer is shown. At zero momentum transfer the central component is dominating the tensor and spin-orbit component being negligible. As only the central part of the interaction contributes to isovector spin-flip transitions, the limit $\mathbf{q}$=0 is imposed for studying the GT strengths.

In the figure 2.3, the relation between the intensities of different central components of the effective NN interaction, at zero momentum transfer, as function of the incident energy is given. The values are based either on the free NN t_f matrix interaction (for incident energies above 100 MeV), or on the

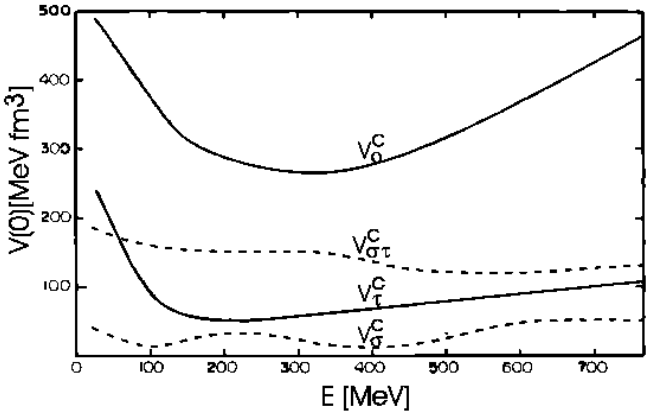

Figure 2.3 Energy dependence of the volume integrals of the central components of the NN effective interaction at zero momentum transfer. Picture taken from [Pet81].

density-dependent G-matrix interaction (for incident energies below 100 MeV, where the multiple scattering can occur) [Pet81]. As can be seen from the picture, at intermediate incident energies starting from about 100 MeV/u up to about 400 MeV/u, the isovector spin-flip component clearly dominates the isoscalar spin-flip component and the isovector non-spin-flip one. As the GT transitions are mediated by the $\boldsymbol{\sigma\tau}$ operator, this is the suitable energy region for studying the GT strength distributions. In this energy region also the isoscalar non-spin-flip component of the interaction reaches its minimum. The non-central components are not included in the picture as they vary slowly with the energy.

The central isovector spin-flip term that mediates the GT transitions in CE and IE reactions is:

$$\sum_i V_{\sigma\tau}(r)\boldsymbol{\sigma}_1 \cdot \boldsymbol{\sigma}_2 \boldsymbol{\tau}_1 \cdot \boldsymbol{\tau}_2$$

This term is similar to the corresponding GT β-decay operator:

$$g_A \sum_i \boldsymbol{\sigma}_i \boldsymbol{t}_i^{\pm}$$

where g_A is the axial vector coupling constant. The same situation holds for the isovector non-spin-flip transitions, associated to the Fermi (F) transitions.

The isovector non-spin-flip operator from CE and IE reactions:

$$\sum_i V_\tau(r)\boldsymbol{\tau}_1 \cdot \boldsymbol{\tau}_2$$

is similar to the corresponding F β-decay operator:

$$g_V \sum_i \boldsymbol{t}_i^{\pm}$$

where g_V is the vector coupling constant.

2.2 Gamow-Teller strength extracted from the experimental data

A proportionality between the CE reaction cross section and the GT transition strength was expected. It was demonstrated empirically in the cases where the transition strength was already known from β-decay studies [Goo80, Pet80, Sat80, Tad87].

The β-decay transition strengths are obtained from the β-decay lifetimes:

$$(g_V)^2 B(F) + (g_A)^2 B(GT) = \frac{K}{ft} \tag{2.8}$$

where the f is the statistical rate function, t is the partial half-life for the transition, $K/(g_V)^2 = 6144.4 \pm 1.6\ s$ [Tow02] and $(g_A/\boldsymbol{g}_V) = -1.266 \pm 0.004$ [Sch95].

The CE reaction cross section depends on the beam energy, the number of nucleons in the target nucleus A(N,Z), the momentum transfer $\boldsymbol{q}$, the energy loss $\omega = E_x - Q$ and, also, on the structure of the initial and final nuclear states. It can be described by the formula:

$$\sigma = \hat{\sigma}_\alpha(E_{beam}, A) F_\alpha(q, \omega) B(\alpha) \tag{2.9}$$

where α corresponds either to F or to GT transitions. The proportionality factor $\hat{\sigma}$ is called "unit cross section" and it's a function of the beam energy and the nature of the target. The factor F_α is used to extrapolate the cross section to zero momentum transfer and zero energy loss. It describes the shape of the cross section distribution and it goes to 1 at vanishing momentum transfer and energy loss. It is obtained by theoretical calculations (e.g. calculations in the Distorted Wave Born Approximation (DWBA)).

One of the main aspects of correlating the experimental CE reaction cross section to the GT strength distribution is the determination of the unit cross section. The unit cross section can be either determined experimentally or calculated theoretically. As $\hat{\sigma}$ is constant within a nucleus [Tad87], experimentally, it is determined from a transition with known $B(GT)$. The most accurate calibration comes from β-decay.

As GT β-decay is a pure $\boldsymbol{\sigma\tau}$ transition, the reduced transition strength is given in ref. [Fuj99a] by:

$$B(GT^{\pm}) = \frac{1}{2J_i+1}\ \frac{1}{2}\ |\langle J_f T_f T_{zf}||\sum_{j=1}^{A}\boldsymbol{\sigma}_j\boldsymbol{\tau}_j^{\pm}||J_i T_i T_{zi}\rangle|^2 \tag{2.10}$$

with $J_{i,f}$,$T_{i,f}$,$T_{zi,zf}$ - the spin, the isospin and the z component of the isospin of the initial and, respectively, final state. By applying the Wigner-Eckart theorem in the isospin space, one gets:

$$B(GT^{\pm}) = \frac{1}{2J_i+1}\ \frac{1}{2}\ \frac{C_{GT}^2}{2T_f+1}\ |\langle J_f T_f|\ ||\sum_{j=1}^{A}\boldsymbol{\sigma}_j\boldsymbol{\tau}_j||\ |J_i T_i\rangle|^2 \tag{2.11}$$

where C_{GT} is the isospin Clebsch-Gordan coefficient for the corresponding transition (see eq. 2.27).

While the GT transition in CE reaction is the inverse of the β-decay transition, the initial and final states will be reversed. As the reduced matrix element is the same, the GT strength in CE reaction $B(GT^{\pm})$ will be related to the GT strength in β-decay $B(GT^{\mp})$ by:

$$B(GT^{\pm}) = \frac{2J_f+1}{2J_i+1}B(GT^{\mp}) \tag{2.12}$$

the i and f denoting the initial and final states in the CE reaction. The $B(GT^{-})$ is determined in CE (n,p)-type reactions while the $B(GT^{+})$ is determined in CE (p,n)-type reactions.

A theoretical calculation of the unit cross section is presented in ref. [Tad87]. The CE reaction cross section is obtained by Satchler [Sat80] from the transition matrix, as follows:

$$\sigma = \frac{E_i E_f}{(2\pi\hbar^2c^2)^2}\frac{k_f}{k_i}\frac{1}{2}\frac{1}{2J_i+1}\sum|T(M_f M_i m_i m_f)|^2 \tag{2.13}$$

where $E_{i,f}$ is the initial (final) energy and the sum is over the spin projections of the projectile and target. In the DWBA the reaction cross section will have

the form:

$$\frac{d\sigma(q,\omega)}{d\Omega} = K(E_{beam},\omega)N_{\sigma\tau}^{D}|\mathbf{J}_{\sigma\tau}|^2 B(GT) \tag{2.14}$$

where

$$K(E_{beam},\omega) = \frac{E_i E_f}{(\pi\hbar^2 c^2)^2}\frac{k_f}{k_i} \tag{2.15}$$

is a kinematic factor, $\mathbf{J}_{\sigma\tau}$ is the volume integral of the $V_{\sigma\tau}$ nucleon-nucleus interaction component and $N_{\sigma\tau}^{D}$ is the *distortion factor*, defined by the ratio of plane-waves and distorted-waves cross sections:

$$N_{\sigma\tau}^{D}(q,\omega) = \frac{\sigma(DW;q,\omega)}{\sigma(PW;0)} \tag{2.16}$$

In equation 2.14, the distortion factor corrects also for the low momentum transfer dependence of the interaction and transition density and the kinematic dependence on $K(E_{beam},\omega)$. In the limit $(q,\omega) \longrightarrow 0$, it becomes

$$N_{\sigma\tau}^{D} = \frac{\sigma(DW;0)}{\sigma(PW;0)} \tag{2.17}$$

and the unit cross section becomes:

$$\hat{\sigma}(E_{beam},A) = K(E_{beam},0)N_{\sigma\tau}^{D}|\mathbf{J}_{\sigma\tau}|^2 \tag{2.18}$$

2.2.1 The $(d,^2\mathrm{He})$ reaction

The $(d,^2\mathrm{He})$ reaction acts as a (n,p) reaction by replacing a proton in the target nucleus by a neutron. This reaction can be seen as proceeding through the formation of the unbound nucleus ^{2}He, which immediately decays in two protons, as shown in figure 2.4.

$$^2d_1 \ + \ ^AX_Z \ \longrightarrow \ ^AY_{Z-1} \ + \ ^2\mathrm{He}_2 \longrightarrow \ ^AY_{Z-1} \ + \ ^1p_1 \ + \ ^1p_1$$

This reaction can be denoted also as $(d,2p)$.

As mentioned above, this reaction is a good filter for the GT transitions, as the deuteron is mainly in a triplet state $^3S_1$ ($J^\pi = 1^+,\ T = 0$) and the detected ^{2}He in a singlet state $^1S_0$ ($J^\pi = 0^+,\ T = 1$). The reaction cross section can be related to the GT strength similar as in eq. 2.14 (see ref. [Gre04]):

$$\left(\frac{d\sigma(q=0)}{d\Omega}\right)_{(d,^2He)} = C \times \left[\left(\frac{\mu}{\pi\hbar^2}\right)^2 \frac{k_f}{k_i} N_D \mathbf{J}_{\sigma\tau}^2 B(GT^+)\right] \tag{2.19}$$

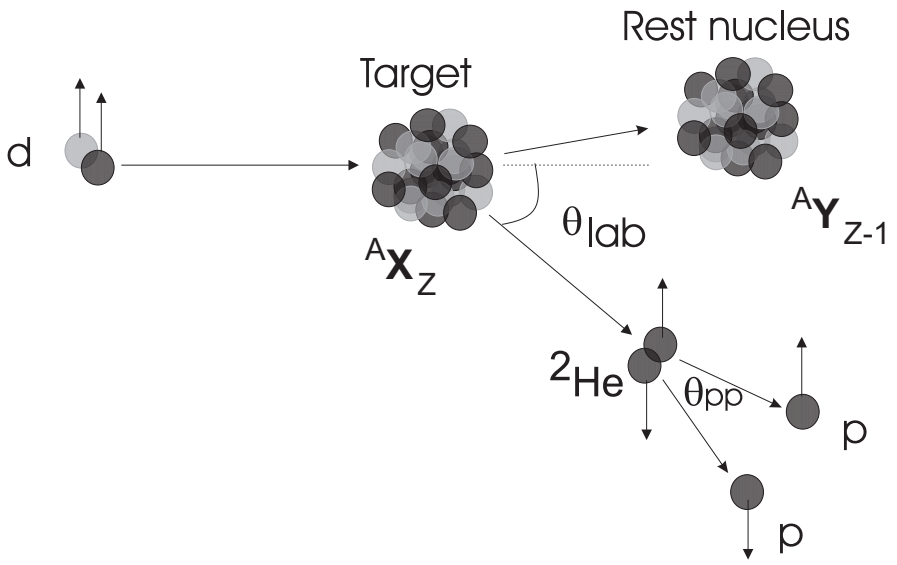

Figure 2.4 Schematic representation of $(d,^2\mathrm{He})$ reaction.

where $\frac{d\sigma(q=0)}{d\Omega} = \left(\frac{\sigma(q=0)}{\sigma(\theta,\ q)}\right)_{DWBA}\left(\frac{d\sigma(\theta,\ q)}{d\Omega}\right)_{exp}$ is the differential cross section extrapolated to zero momentum transfer and zero energy loss, by using a theoretical calculation in the DWBA. A scaling factor C has been introduced in eq. 2.19 due to the more complicated reaction mechanism of $(d,^2\mathrm{He})$ compared to (p,n) reaction. A series of $(d,^2\mathrm{He})$ experiments performed on nuclei with known $B(GT^+)$ either from β-decay, or from the complementary reaction on a self-conjugate nucleus, shows that the C factor should be constant not only within a nucleus, but it should be not mass dependent. The value of this constant ($C = 0.320 \pm 0.027$) was determined by Grewe et al. [Gre04] as the inverse of the slope of the fit of experimentally obtained values for the reduced cross section $\left(\frac{d\sigma(q=0)}{d\Omega}\right)_{(d,^2\mathrm{He})}\left[\left(\frac{\mu}{\pi\hbar^2}\right)^2\frac{k_f}{k_i}N_D\mathbf{J}^2_{\sigma\tau}\right]^{-1}$ versus the reference $B(GT)$ for GT transitions starting from ^{12}C, ^{24}Mg and ^{32}S nuclei (see fig. 2.5).

2.2.2 The $(^3\mathbf{He},t)$ reaction

The $(^3\mathrm{He},t)$ CE reaction, schematically represented in fig. 2.6, acts as a (p,n) reaction. It replaces a neutron in a nucleus by a proton:

$$^3\mathrm{He}_2 \ + \ ^AX_Z \ \longrightarrow \ ^AY_{Z+1} \ + \ ^3t_1$$

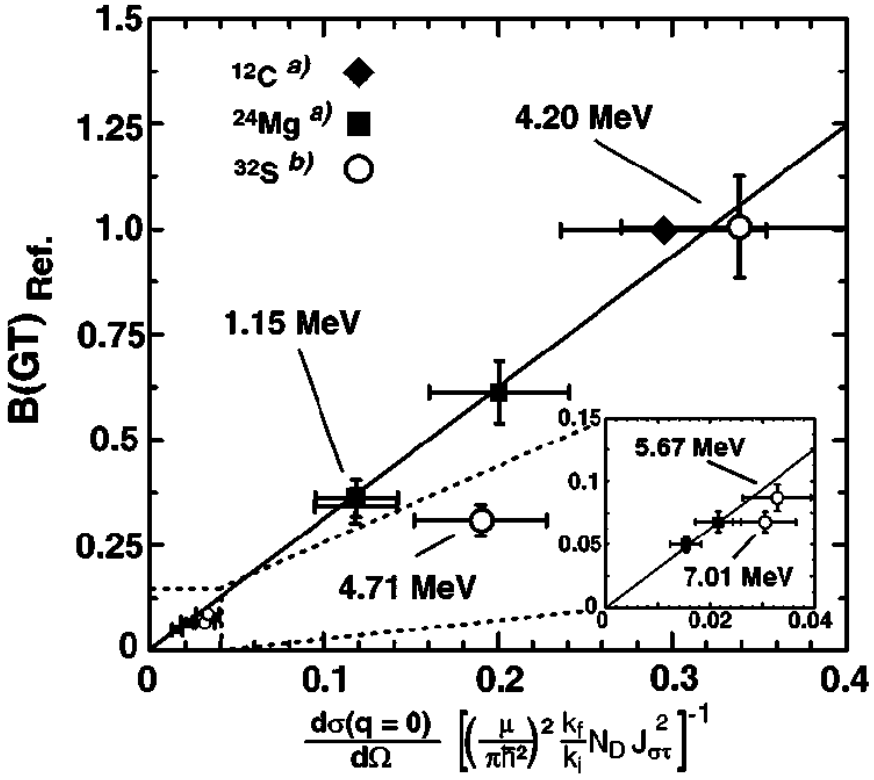

Figure 2.5 The reference B(GT) values as function of the $(d,^2\mathrm{He})$ reduced cross section for GT transitions starting from ^{12}C, ^{24}Mg and ^{32}S nuclei. The fit is linear, the inverse of the slope giving the calibration factor C. Numerical excitation energy values are given only for levels in ^{32}P. The insert represents the low excitation energy region. Te error on the cross sections is of the order of 20%. $B(GT^-)_{Ref}$ values from (p,n) data are known with an accuracy of 12%. Picture taken from ref. [Gre04]

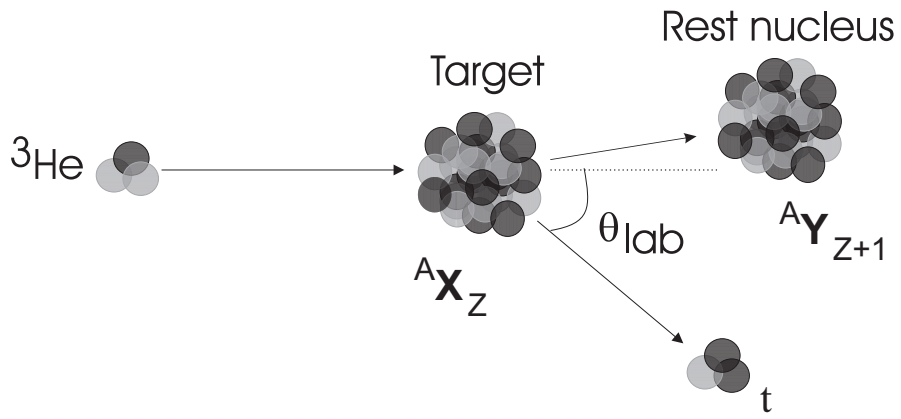

Figure 2.6 Schematic representation of $(^3\mathrm{He}, t)$ reaction.

The isospin-flip character of this reaction is ensured by the change of charge. Both $V_{\sigma\tau}$ and V_τ components of the interaction act in this case, but their separation is usually not difficult. The transitions generated by the V_τ operator are Fermi (F) transitions and, actually, as they appear between the members of an isobaric multiplet (that means the $T_0 \longrightarrow T_0$ transitions), the full Fermi strength will be concentrated in the Isobaric Analogue State (IAS) of the target ground state.

Systematic $(^3\mathrm{He}, t)$ studies on different nuclei at incident energies above 100 MeV/u have shown that, similar to (p, n) reactions, the proportionality between the reaction cross section and the GT- or F- strength remains valid [Fuj96]. Figure 2.7 shows a plot of the $(^3\mathrm{He}, t)$ reduced cross section for transitions in different investigated nuclei as a function of the reference strengths (either Fermi - left pannel, or Gamow-Teller - right pannel). In both cases the linear relation between the cross section and the transition strength values was found as expected theoretically [Goo80, Tad87]:

$$\begin{aligned} \left(\frac{d\sigma(q=0)}{d\Omega}\right)^F_{(^3He,t)} &= \left(\frac{\mu}{\pi\hbar^2}\right)^2 \frac{k_f}{k_i} N_D^\tau \mathbf{J}_\tau^2 B(F) \\ &= \widehat{\sigma}_F(q=0) B(F^-) \end{aligned} \tag{2.20}$$

and

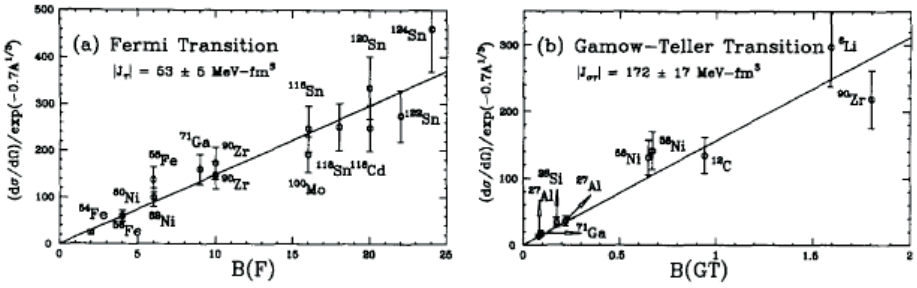

Figure 2.7 The $(^3\mathrm{He}, t)$ reduced experimental cross section over *a*) B(F) or *b*) B(GT) values for various target nuclei. The factor $exp(-xA^{1/3})$ is an approximation to the distortion factors N_D^τ and $N_D^{\sigma\tau}$. An average value of $x = 0.7$ was empirically determined (see [Fuj96] for details). Picture taken from ref. [Fuj96].

$$\left(\frac{d\sigma(q=0)}{d\Omega}\right)^{GT}_{(^3He,t)} = \left(\frac{\mu}{\pi\hbar^2}\right)^2 \frac{k_f}{k_i} N_D^{\sigma\tau} \mathbf{J}^2_{\sigma\tau} B(GT^-) = \widehat{\sigma}_{GT}(q=0) B(GT^-) \tag{2.21}$$

We define R^2, the ratio of the GT and F unit cross sections:

$$R^2 = \frac{\widehat{\sigma}_{\mathrm{GT}}(q=0)}{\widehat{\sigma}_{\mathrm{F}}(q=0)} = \frac{\sigma_{\mathrm{GT}}(q=0)}{\sigma_{\mathrm{F}}(q=0)} \frac{B(F)}{B(GT)} \tag{2.22}$$

Given the linear proportionality shown in fig. 2.7, it is expected for R^2 to be a constant. However, more recent $(^3\mathrm{He}, t)$ experiments performed at RCNP indicate that there is a dependence of the R^2 on the mass number, which is not linear. These experiments were performed by using the recently developed WS beam-line and are, therefore, characterized by a better energy resolution. The plot of R^2 as function of the mass number for several measured nuclei is given in fig. 2.8.

By using this parameterization, the GT unit cross section can be determined as function of the mass number and Fermi cross section.

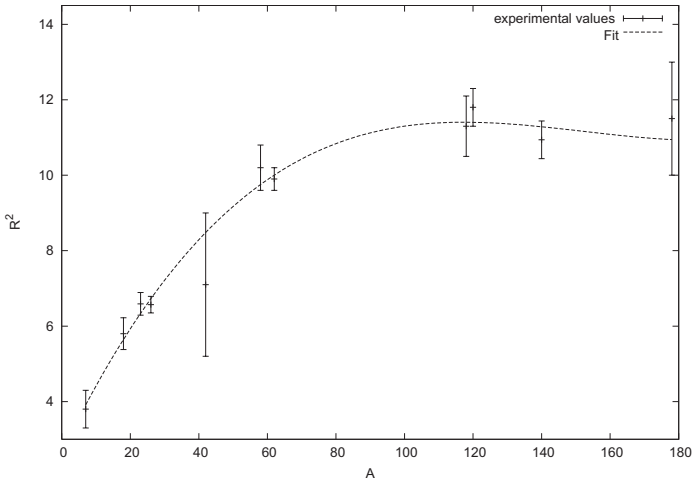

Figure 2.8 The dependence of R^2 on the mass number, as determined in $(^3\mathrm{He}, t)$ experiments performed in RCNP, at 420 MeV [Fuj05]. The experimental values are indicated together with the error bars. The dotted line represents a fit of the experimental values.

2.3 The Gamow-Teller strength distribution over different isospin components. The isobaric analogue states.

In a nucleus, the z-component of the isospin is $T_z = \frac{1}{2}(N - Z)$ and the isospin of the ground and excited states must be $T \geq |T_z|$. The isospin nature of the states excited via CE and IE reactions is discussed in what follows, where we denote by T_0 the z-component of the target isospin.

In terms of one-particle one-hole excitations, the isospin of the quantum of excitation characterizing the isospin-flip transitions will be $\tau = 1$ with an eigenvalue $\mu_\tau = 0, \pm 1$. Therefore the isospin excitations give rise to a triplet of states with: $T = T_0 - 1,\ T_0,\ T_0 + 1$. Figure 2.9 shows possible isospin components excited by different CE and IE reactions starting from a nucleus with ground state isospin $T = T_z = T_0$:

• via the $(^3\mathrm{He}, t)$ reaction the z-component of the isospin of the final nucleus is $T_z = \frac{1}{2}((N - 1) - (Z + 1)) = T_0 - 1$. As a consequence, all three isospin components mentioned above are excited.

• via the $(d,{}^2\mathrm{He})$ reaction the final nucleus has $T_z = T_0 + 1$ and, as for the final states $T \geq T_z$, the $T_0 + 1$ are the only states that can be excited.

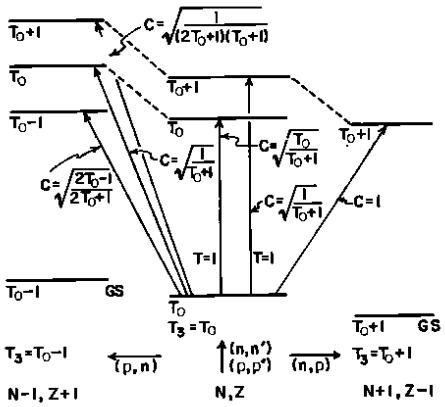

Figure 2.9 Schematic representation of the isospin-flip transitions starting from a nucleus with ground-state isospin T_0=T_z=(N-Z)/2. The corresponding Clebsch-Gordon coefficients (C) [Sat83] for different transitions are indicated.

• an IE reaction, as (p, p'), will excite T_0 and $T_0 + 1$ states in the target nucleus.

In fig. 2.9 the dashed lines connect the states with the same isospin in different nuclei (with the same A but different T_z). These are the so called Isobaric Analogue States; they have similar properties. Symmetry is also expected among transitions for which the initial or final states are replaced by isobaric analogue states. Te correspondence in energy and strength of this kind of analogous transitions is discussed below.

All the low-lying energy levels in the $(^3\mathrm{He}, t)$ spectrum have the minimum isospin $(T_0 - 1)$, while the first $T_0 + 1$ state occur at excitation energies well above the threshold for proton emission [Boh98]. Due to the charge independence of the nucleonic interactions, the binding energy for the lowest state with any given isospin $T > T_z$ can be obtained. The difference in binding energy for states in the same nucleus (so the same A and T_z) and having different values of T is given by the symmetry energy. Therefore the lowest states with $T = T_z + 1$ occur at an excitation energy:

$$E(A, T + 1, T_z = T) - E(A, T, T_z = T) = 4b_{sym}\frac{(T + \frac{1}{2})}{A} \tag{2.23}$$

where b_{sym} ≈50 MeV [Boh98] was deduced by fitting the experimental data. The formula from eq. 2.23 neglects the shell structure and pairing effects.

T	T_0-1=3	T_0=4	T_0+1=5
C^2_{CG}	$\frac{7}{9}$	$\frac{1}{5}$	$\frac{1}{49}$
% of $\sum B(GT)$	77.8%	20%	2.2%
$E_{coupling}$ [MeV]	-7.21	-1.56	6.25

Table 2.1 Relative intensities (as C^2_{CG}) and positions of different isospin components excited in the ^{64}Ni(^{3}He, t)^{64}Cu reaction. The C^2_{CG} as indicated in [Sat83] were used (see fig 2.9). The relative positions were calculated by using eq. 2.28. The amount of the total $B(GT)$ exhausted by each component is also indicated.

In the absence of the coupling between the isospin of the vibration and T_0, the three components would be degenerate and the difference in binding energies between T_0-1, T_0 and T_0+1 members can be estimated by the Coulomb energy difference between the isobaric analogue states:

$$\Delta E_{Coul}(T_0) = E_{Coul}(A, T_0, T_z = T_0 - 1) - E_{Coul}(A, T_0, T_z = T_0) \qquad (2.24)$$

and

$$\Delta E_{Coul}(T_0+1) = E_{Coul}(A, T_0+1, T_z = T_0 - 1) - E_{Coul}(A, T_0+1, T_z = T_0+1), \qquad (2.25)$$

for the case of heavy and medium-heavy nuclei (A$\geq$40) the Coulomb energy being [Boh98]:

$$E_{Coul} \approx 0.7 \frac{Z^2}{A^{1/3}}[1 - 0.76A^{-2/3}]\ MeV. \qquad (2.26)$$

Experimentally it was shown that the deviations of the difference in binding energies and the Coulomb energy difference between isobaric analogue states for the different $T = T_0$ states are small [Ric66].

In this simple approximation, which doesn't take into account the coupling between T_0 and τ, the intensity ratios of the different isospin components are given by the square of the corresponding Clebsch-Gordan (CG) coefficients for those components:

$$C^2_{CG} = |\langle T_i\ T_{z_i}\ \tau\ \mu_\tau \mid T_f\ T_{z_f}\rangle|^2 \qquad (2.27)$$

However, for nuclei with neutron excess an isovector potential is created in the nucleus which acts on the isospin of the vibration, τ, so that the states with low total isospin are favored. In the presence of this coupling, the fundamental shift produced by the neutron excess is [Boh98]:

$$E_{coupling} = \frac{V_1}{A}(\boldsymbol{\tau} \cdot \mathbf{T}_0) = \frac{V_1}{2A}[T(T+1) - T_0(T_0+1) - \tau(\tau+1)] \qquad (2.28)$$

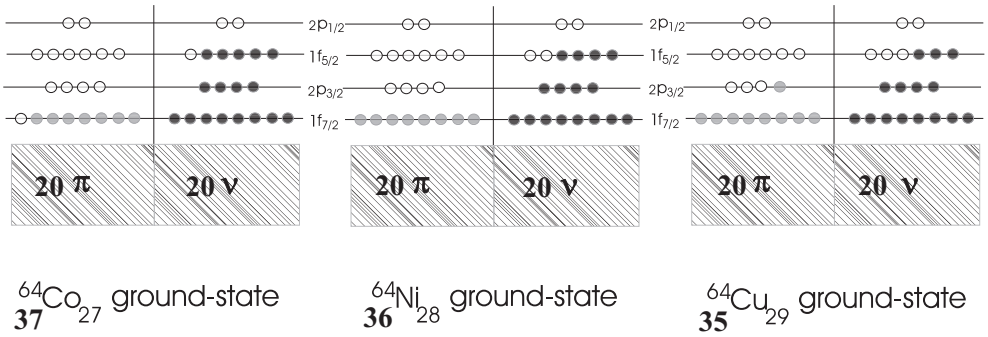

Figure 2.10 Shell model picture of the involved nuclei

whereby V_1 is of the order of 100 MeV. It is clear that the interaction energies given by eq. 2.28 become quite large, even for moderate values of T_0.

Table 2.1 gives the calculated values of the square of the CG coefficients and the displacement energies (calculated using eq. 2.28) for the three isospin components excited in ^{64}Cu via the $(^3\mathrm{He}, t)$ reaction. The difference in energies gives the relative positions of the centroids and the intensity ratios represents the ratios of the summed strengths for different isospin components. The amount of the GT strength exhausted by each isospin component is also indicated.

As can be observed, the $T_0 \longrightarrow T_0+1$ transitions are very much suppressed, only 2.2% of the GT strength going to $T_0 + 1$ states. Most of the strength is exhausted by the $T_0 - 1$ component, that forms the giant GT resonance (GTR).

2.4 Shell model states involved in the ^{64}Ni$(^3$He$, t)$ and ^{64}Ni$(d,^2$He$)$ reactions

Figure 2.10 shows the g.s. configuration of the ^{64}Co, ^{64}Ni and ^{64}Cu nuclei in the most simple shell model picture. In this approximation the nuclei are considered in a spherical shape, all the shells up to $1d_{3/2}$ being filled and the remaining protons and neutrons being distributed over the $1f_{7/2}$, $2p_{3/2}$, $1f_{5/2}$ and $2p_{1/2}$ shells.

In this simple picture, allowed 1particle-1hole (1p1h) configurations for the transitions excited via CE reactions are depicted in fig. 2.11. As ΔL=0, the $\sigma\tau$ excitations starting from the g.s. of ^{64}Ni can only be as follows:

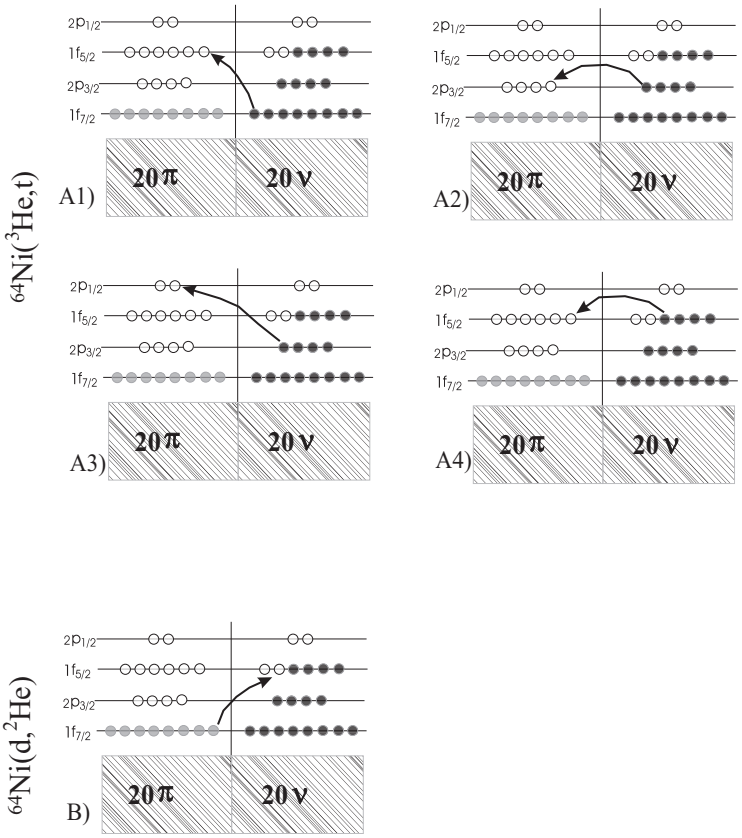

Figure 2.11 Allowed 1p-1h configurations in $A1) - A4)$ ^{64}Ni(^{3}He, t) and $B)$ ^{64}Ni(d,^{2}He) reactions.

- for the (^{3}He, t) reaction
  - $\star$ $(1\nu f_{7/2}^{-1}, 1\pi f_{5/2})$ (fig. 2.11 $A1$)),
  - $\star$ $(2\nu p_{3/2}^{-1}, 2\pi p_{3/2})$ (fig. 2.11 $A2$)),
  - $\star$ $(2\nu p_{3/2}^{-1}, 2\pi p_{1/2})$ (fig. 2.11 $A3$)),
  - $\star$ $(1\nu f_{5/2}^{-1}, 1\pi f_{5/2})$ (fig. 2.11 $A4$))
- for the (d,^{2}He) reaction
  - $\star$ $(1\pi f_{7/2}^{-1}, 1\nu f_{5/2})$ (fig. 2.11 B))

Chapter 3

Isovector spin-flip collective excitations

Especially in medium and heavy mass nuclei the level density is so high that the transition strength is spread over many states and the isovector spin-flip transitions can appear as collective excitations (known as "giant resonances"). Giant resonances have attracted much attention because of their fundamental nature. They provide information not only on the effective nucleon-nucleon interaction but also on other basic properties of nuclei, like the shape and compressibility.

Different vibrational modes of the nucleus have been presented in the introductory chapter. An overview of the isovector spin-flip giant resonances that can be present in the ^{64}Co and ^{64}Cu spectra, obtained via (d,^{2}He) and (^{3}He, t) reactions studied in this thesis, is given in the following sections.

3.1 The Gamow-Teller Giant Resonance

The Gamow-Teller Giant Resonance (GTGR) is defined as a $0\hbar\omega$ collective spin-isospin oscillation in which the excess nucleons coherently change the direction of their spins and isospins without changing the orbital motion [Ost92]. These resonances are characterized by the following changes in quantum numbers: $\Delta J^\pi = 1^+$, ΔL=0, ΔS=1, ΔT=1. As it was discussed in Chapter 2, these resonances are excited by the $V_{\sigma\tau}$ component of the NN interaction (see 2.1).

The GTGR was predicted by Ikeda et al. [Ike63] in 1963, but experimentally it was first recognized in 1980, in (p, n) CE experiments performed at IUCF [Goo80, And80, Gaa81] by using proton beams with energies between

120 and 200 MeV. The spectra of nuclei with neutron excess were dominated by one prominent peak, with a characteristic ΔL=0 shape of the angular distribution, proving that the orbital motion of the nucleons is unchanged in the transition. The isospin transfer is imposed by the reaction (charge exchange) and the spin transfer was derived from the incident-energy dependence of the GT cross section. Therefore the change in quantum numbers that characterize the GTGR were fulfilled.

Actually the presence of the broad bump corresponding to the GTGR was observed already in 1962 by Bowen et al. [Bow62] in the (p,n) spectra measured at 0° on several Cu, U and Pb targets by using a proton beam of 143 MeV. But these authors didn't recognize the nature of the bump. As the experimental resolution was very poor, Ikeda et al interpreted incorrectly this resonance as being the IAS of the target g.s. [Ike62].

In the (p,n) spectra of medium and heavy mass nuclei the GTGR appears as a broad peak, with a width of about 4 MeV, energetically located at 3 - 6 MeV above the IAS of the target ground state for medium-heavy nuclei and at about the same energy as the IAS for heavy targets with large neutron excess. These high-lying states are mainly associated with excitations of neutrons from $j = l + 1/2$ orbits into protons in $j = l \pm 1/2$ orbits. The existence of low-lying GT fragments was also predicted and observed experimentally in neutron-rich nuclei; they are mainly generated by spin-flip transitions of the type: $j = l - 1/2 \rightarrow j = l + 1/2$.

Unlike the GTGR, the IAS is rather sharp. As the IAS is excited by the V_τ component of the NN interaction (see 2.1), there is a large difference in the dependence of the excitation strengths of the two resonances on the incident energy. The difference comes from the strong energy dependence of V_τ term in the projectile-target interaction. V_τ is reduced with increasing energy of the projectile, while $V_{\sigma\tau}$ is almost constant (see also fig. 2.3). This behavior was e.g. observed in the ^{14}C$(p,n)^{14}$N reaction [Rap94].

Experimentally only about 60% of the strength predicted by Ikeda et al. [Ike63] was observed in the energy region where the major GT peaks occur. This so called *quenching* effect (the missing of strength) was observed for many nuclei with different mass numbers, although the Ikeda sum rule: $\sum B(GT^-) - \sum B(GT^+) = 3(N - Z)$ is based on very fundamental assumptions. The results obtained for the total GT strength extracted from 160 MeV (p,n) data of Rapaport and Gaarde is summarized by Osterfeld in ref. [Ost92] (see fig. 3.1).

There are two different attempts to explain the quenching of the total GT strength. The first one is the coupling of Δ-hole states to the one-particle

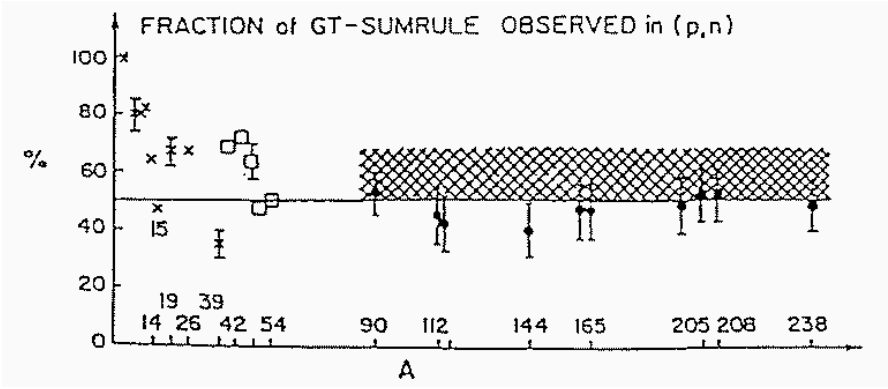

Figure 3.1 Fraction of GT sum-rule strength observed in (p, n) reactions on different targets. For the medium and heavy mass nuclei the points represent the strength concentrated in individual peaks while the marked area includes also an estimation of the strength under the collective states. Picture taken from ref. [Ost92].

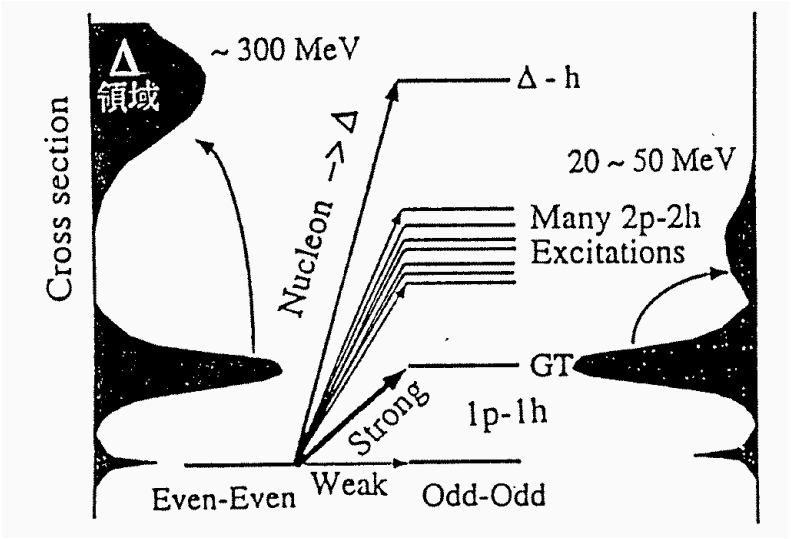

Figure 3.2 Representation of the GT strength function in the two different approximations responsible for the quenching (see text). Picture taken from ref. [Ari99].

one-hole (1p-1h) states, that leads to the shift of the GT strength at about 300 MeV, the position of the Δ resonance [Rho74, Ose79, Knü80] (see fig. 3.2-left). But it was shown by Arima [Ari99] that the short range correlations in Δ-hole interaction are less important than in the 1p-1h channel; therefore the contributions of the Δ-hole excitation to the quenching of the GT strength should be small.

The second explanation of the *quenching* is the configuration mixing effect [Ari99, Ost92, Ram91](see fig. 3.2-right). The GT state is surrounded by a large number of two-particle two-hole (2p-2h) states with the same isospin, which couple destructively into the GT mode leading to a fragmentation of the strength and shifts part of it beyond the GTR. In this case the missing strength will be located in a continuum region (see section 3.4). As the shape and magnitude of the continuum region is still a matter of study, the experimental estimation of the GT strength in this region and the extraction the full strength is still a problem.

Both mechanisms discussed above are strongly dependent on the residual interaction that couples 1p-1h states either to the Δ-hole states or to the 2p-2h states.

Multipole decomposition techniques are used to extract the GT strength in the continuum region. In this way, up to 90% of the predicted strength was obtained e.g. by Wakasa et al in ^{90}Zr in the energy region up to 50 MeV [Wak97]. This result supports the configuration mixing assumption.

As via a (n,p)-type reaction on a nucleus with the ground state isospin T_0 only the T_0+1 component of the collective excitation is measured (see 2.3), by investigating both (p,n) and (n,p)-type reactions on the same target nucleus the Ikeda sum-rule, according to which the difference of the measured cross sections in the two reactions should be proportional to 3(N-Z), can be tested.

3.2 The Spin Isovector Giant Monopole Resonance

The $2\hbar\omega$ collective excitations characterized by $\Delta J^\pi = 1^+$ are named Giant Monopole Resonances (GMR). Experimentally, the first observations were of the isoscalar part of the GMR which was studied in α-scattering experiments on medium and heavy mass nuclei between ^{40}Ca and ^{209}Bi [You77, Har77, Har79, Roz80, You81]. This type of oscillation is called also "the breathing mode" as it is connected with the compression and expansion of the nucleus as a whole, the neutrons and the protons oscillating in phase (ΔT=0).

The isovector part of the GMR is the IsoVector Giant Monopole Resonance (IVGMR) and it was also observed in medium and heavy mass nuclei. It was

observed, e.g., in the $(\pi^{\pm}, \pi^0)$ experiments of Erell et al. [Ere86] on various nuclei between ^{40}Ca and ^{208}Pb. In this mode the neutrons and protons oscillate in opposite phase (ΔT=1). Due to the Coulomb effect the T=T_0+1 component in the (π^-, π^0) reaction is located at relatively lower excitation energies than the T=T_0-1, T=T_0 and T=T_0+1 components in the (π^+, π^0) reaction. The IVGMR appears e.g., in the ^{60}Ni$(\pi^+, \pi^0)^{60}$Cu spectrum at 35.6±2.8 MeV (with a width Γ = 18.4±4.1 MeV) and in the ^{60}Ni$(\pi^-, \pi^0)^{60}$Co spectrum at 25.2±1.7 MeV (Γ = 14.7±2.1 MeV) [Ere86]. In a more recent study of Nakayama et al. [Nak99] of the ^{60}Ni(^{7}Li,^{7} Be)^{60}Co reaction at 65 MeV/u, the IVGMR appears at an excitation energy of 20±2 MeV (Γ = 10±2 MeV).

If, in addition, the nucleons with spin "up" oscillate against the nucleons with spin "down", the spin-flip part of the IVGMR is selected. This is the Spin IsoVector Giant Monopole Resonance (SIVGMR). This resonance implies the same changes in quantum numbers as the GTGR ($\Delta J^\pi = 1^+$, ΔS=1, ΔT=1), but it is a $2\hbar\omega$ excitation. The transition operators of the two resonances are different, the relevant transition operator for the SIVGMR being proportional to $r^2\boldsymbol{\sigma\tau}$ and showing the radial nature of this oscillation. Unlike the GTGR, the SIVGMR can couple to other states with $J^\pi = 1^+$ but with $\Delta L = 2$. In this case there is a mixture of $2\hbar\omega$ modes with $\Delta L = 0$, $J^\pi = 1^+$ and $\Delta L = 2$, $J^\pi = 1^+$. This mixture is mediated by a realistic tensor force [Aue89].

As shown in refs. [Boh98, Aue89], because of the mass conservation and the spherical symmetry of the motion, the radial transition density of any monopole excitation has a specific shape with a node near the nuclear surface (see, e.g., fig. 3.3). The positive peak outside the nuclear surface compensates the negative values in the nuclear interior. In this way the volume integral is vanishing [Boh98]. That means that a strongly absorbed projectile is needed for exciting the monopole resonance, as only the nuclear surface part and not the volume part of the transition density is probed in this way. This explains also the excitation of the IVGMR in pion scattering experiments, as the pions are, at the practiced incident energies, strongly absorbed and cannot penetrate beyond the surface.

The nucleus being rather transparent for protons and neutrons at intermediate energies, the (p, n) CE reaction is not a suitable probe for exciting the SIVGMR. A better choice is the $(^3\mathrm{He}, t)$ reaction, as ^{3}He is strongly absorbed and, at the same time, at intermediate energies, it still shows a good selectivity for isovector spin-flip excitations [Aue71, Aue89].

One of the first experimental evidences of the SIVGMR was the study of Ellegaard et al. [Ell83, Ell85] using the ^{90}Zr$(^3\mathrm{He}, t)$ reaction at 600 MeV. An angular distribution analysis was performed and the existence of the SIVGMR

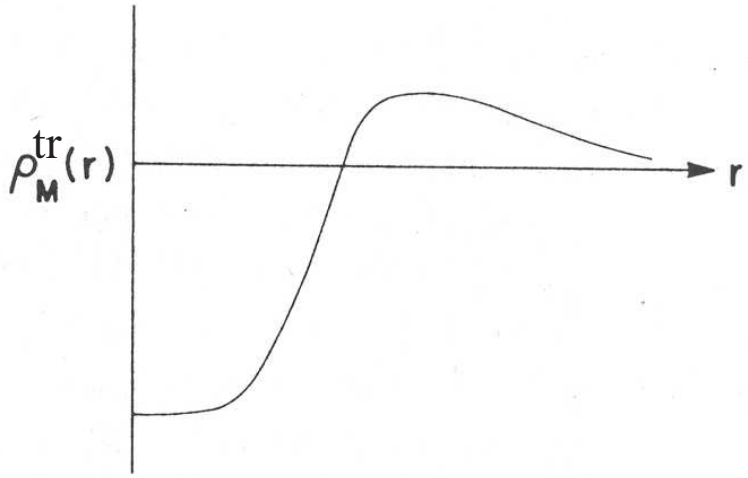

Figure 3.3 The shape of the transition density for the IVGMR in ^{90}Zr. Picture taken from ref. [Aue89]

was proved. The analysis of the 600 MeV, ^{90}Zr(^{3}He, t)^{90}Nb data was reexamined by Auerbach et al. [Aue89] showing that an enhanced background observed around 30 MeV excitation energy is due to the $2\hbar\omega$ SIVGMR, the excitation of this monopole strength being a result of the surface character of the (^{3}He, t) reaction.

A more recent ^{208}Pb(^{3}He, tp) study was performed by Zegers et al. [Zeg00, Zeg03] at E_{3He}=410 MeV with the aim of determining the position and width of SIVGMR in ^{208}Bi. The centroid was found at E_x=37±1 MeV, while the deduced width was 14±3 MeV.

However, the (S)IVGMR is difficult to investigate by charge-exchange reactions because of the large non-resonant background, which is due to quasi-free, pickup-breakup and breakup-pickup reactions underlying the resonance. Also the large width of this resonance makes it very difficult to distinguish between the signal and the background. In addition, as fragments of the GT strength are expected up to about 50 MeV and as the angular distributions of the GTGR and SIVGMR are similar, the estimation of the contribution of the two resonances in this excitation energy region is a problem.

3.3 The Spin Giant Dipole Resonance

The Spin Giant Dipole Resonance (SGDR) is, maybe, the best studied giant resonance, as it appears in most of the nuclei starting from the very light ones (as ^{3}He) to the heavy ones (as ^{208}Pb). The strength of this resonances is fragmented over individual states in light nuclei, while in medium-heavy and heavy nuclei the resonance can be fitted by using a Lorentzian shape, with a width of about 4-5 MeV.

The SGDR is characterized by the following changes in quantum numbers: $\Delta L = 1$, $\Delta S = 1$, $\Delta T = 1$. It consists of $1\hbar\omega$ collective excitations and it can be interpreted as a superposition of three collective modes with J^{π}= 0^{-}, 1^{-} or 2^{-}. Experimentally it is practicaly not possible to resolve the resonance into the three different spin components because the angular distributions are predominantly sensitive to ΔL rather that to ΔJ.

In a (p, n) study at E$_p$=200 MeV on the nucleus ^{90} Zr the SGDR appears at an excitation energy around 25 MeV, having a width of about 10 MeV [Gaa81]. The angular distribution of this resonance has a characteristic L=1 shape with a maximum at 4.5°. The non spin-flip part of the giant dipole resonance (GDR) appears in ^{208}Pb at excitations energies about 5 MeV higher than SGDR, although both modes represent $1\hbar\omega$ excitations. Osterfeld et al. [Ost81] explained the difference by the effect of the residual p-h interaction, that seems to be more repulsive in the τ channel than in the $\sigma\tau$ channel.

In the $(\pi^{\pm}, \pi^{0})$ studies of Erell et al [Ere86] on ^{60}Ni, the GDR is located at 13.5±1.6 MeV, with a width of 4.2±2.0 MeV, in the ^{60}Co spectrum and at 25.3±1.5 MeV, with a width of 6.4±1.7 MeV, in the ^{60}Cu spectrum. Similar positions and widths were found when using ^{40}Ca and ^{90}Zr targets.

The spin-flip part of GDR was observed by Nakayama et al. in the ^{60}Ni(^{7}Li,^{7} Be)^{60}Co reaction at 9±1 MeV (Γ = 7±1 MeV) [Nak99].

In a recent (d,^{2}He) study on ^{58}Ni performed by Hagemann et al. [Hag01, Hag05], a multipole decomposition analysis suggested considerable ΔL=1 strength concentrated around 11.5 MeV. This structure was identified to be the SGDR, by taking into account the isovector spin-flip selectivity of the reaction (see 2.2.1). As the resonance could be extended at higher excitation energies than covered in this experiment, it was not possible to estimate its width.

3.4 The nonresonant continuum background

It was already discussed that an important issue in the study of giant resonances is the understanding and the proper estimation of the nuclear continuum or background underlying the resonance region. The reaction mechanisms that are responsible for the inelastic continuum are still not clear. As for incident energies larger than 100 MeV the reaction mechanism is preferentially single-step scattering [Ost82], multi-step processes are unlikely to contribute to the continuum. It is generally accepted that the main source for the nonresonant continuum is the quasi-free single-step nucleon-nucleon scattering (QFS) [Lis84, McD86, Wat86]. This term is attributed to reactions in which a single nucleon of the projectile scatters on a single nucleon in the target, while the rest of the projectile and target nuclei act just as spectators. Thus, the experimental signature of the QFS processes will follow the kinematics for the free nucleon-nucleon scattering [Kal90].

If the incident particle interacts freely with a nucleon in the target nucleus and the motion of the nucleon in the target nucleus can be regarded simply as the Fermi motion, one expects a broad bump in the energy spectrum with a peak at $E = q^2/2m$ (where m is the nucleon mass and q is the momentum transfered in the QF reaction) and a width determined by the Fermi momentum. This is the so called quasi-free bump. Experimentally, the bump was clearly shown but the peak energy deviates from this simple expectation.

The QFS processes present when performing CE reactions are, mainly, knock-out reactions, schematically illustrated in fig. 3.4. The process detected when performing (d,^{2}He) reactions is the (d,^{2}He n) knock-out reaction on a bound proton (fig. 3.4 left pannel). This proton is ejected together with the proton from the deuteron, forming the detected two-proton system just like in the case of the (d,^{2}He); the neutron is emitted and the residual nucleus remains in a ground or excited single-proton hole state. Similarly, when performing (^{3}He, t) experiments, the (^{3}He, t p) knock-out reaction on a bound neutron (fig. 3.4 right pannel) is detected; a proton is emitted and the residual nucleus remains in a ground or an excited single-neutron hole state. In both cases the Fermi motion of the nucleons inside the nucleus will determine the energy broadening of the quasi-free reaction.

A reasonable description of the QFS spectrum (both for (d,^{2}He) [dH04] and (^{3}He, t) reactions [Jän93]) seems to be obtained by using a semi-phenomenological function developed in the study of pion-induced CE reactions [Ere86, Iro86]. Several ($\pi^{\pm}, \pi^0$) reactions on different targets with mass between 40 and 208 have been measured at different scattering angles between 0° and 30°. The obtained function was based on a consistent treatment of the

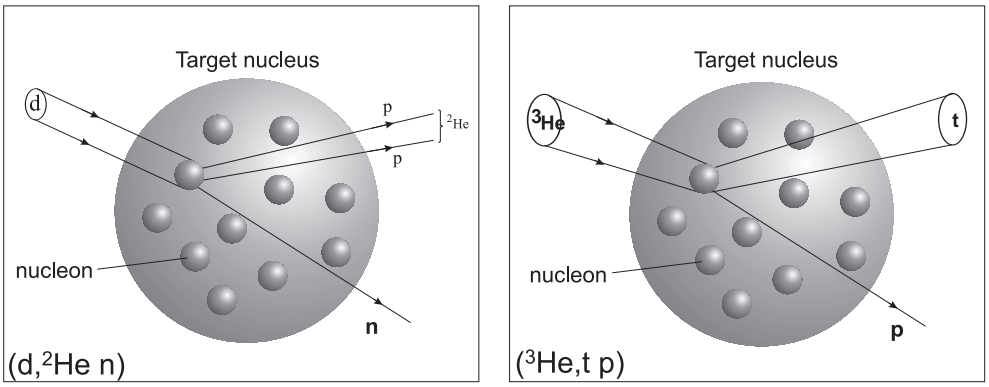

Figure 3.4 Schematic picture of the quasi-free scattering processes accompanying the $(d,^2\mathrm{He})$ and $(^3\mathrm{He},t)$ reactions.

spectra for all targets and angles:

$$\frac{d^2\sigma}{d\Omega dE} = N\frac{1-exp[-(E_x-E_0)/T]}{1+[(E_x-E_{QF})/W_L]^2}, \qquad E_x > E_0, \tag{3.1}$$

where N is a scattering angle dependent normalization factor (it doesn't depend on E_x), E_0 is the separation energy of the last nucleon in the rest nucleus and T is an energy cut-off parameter. E_{QF} is given by the kinematics of the actual reaction ($(d,^2\mathrm{He})$ or $(^3\mathrm{He},t)$ for the present study) on the target nucleon. It represents the centroid of the quasi-free peak, which width is represented by W_L. For the case of the $(d,^2\mathrm{He})$ reaction it can be calculated by [Ere86]

$$E_{QF} = E_{^2He}(free) - (S_n + E_{x_p}), \tag{3.2}$$

where $E_{^2He}(free)$ is the energy of the free process and S_n represents the neutron separation energy of the rest nucleus. The excitation energy of the proton-hole state, E_{x_p}, is zero if the proton is removed from the orbit nearest the Fermi surface. If the proton is removed from another orbit, E_{x_p} is given by the energy difference between its orbit and the Fermi orbit.

For the case of the $(^3\mathrm{He},t)$ reaction, E_{QF} can be calculated by [Ere86, Jän93]:

$$E_{QF} = E_t(free) - (S_p + E_{x_n} + B_{Coul}), \tag{3.3}$$

where $E_t(free)$ is the energy of the free process, S_p is the proton binding energy, E_{x_n} is the excitation energy of the neutron-hole state and B_{Coul} is the

Coulomb barrier for the outgoing free proton. As discussed previously, E_{x_n} is zero only if the proton is removed from the orbit nearest the Fermi surface.

The width of the quasi-free peak W_L is due to the Fermi motion of the proton (respectively, neutron) inside the target nucleus. It is an adjustable parameter in the equation 3.1. N and T are also adjustable parameters that have to be determined by fitting the experimental data.

A good agreement between the estimations using this semi-phenomenological approximation and (d,^{2}He) measurements in coincidence with neutrons was observed in a study on ^{12}C performed by M. de Huu [dH04]. The results of this comparison are given in fig. 3.5.

However high resolution (^{3}He, t) experiments performed recently at RCNP showed that the estimation of the QF continuum region (QFC) by using the eq. 3.1 is more suited for measurements with a not so good energy resolution, while it doesn't fit well the high resolution (^{3}He, t) spectra.

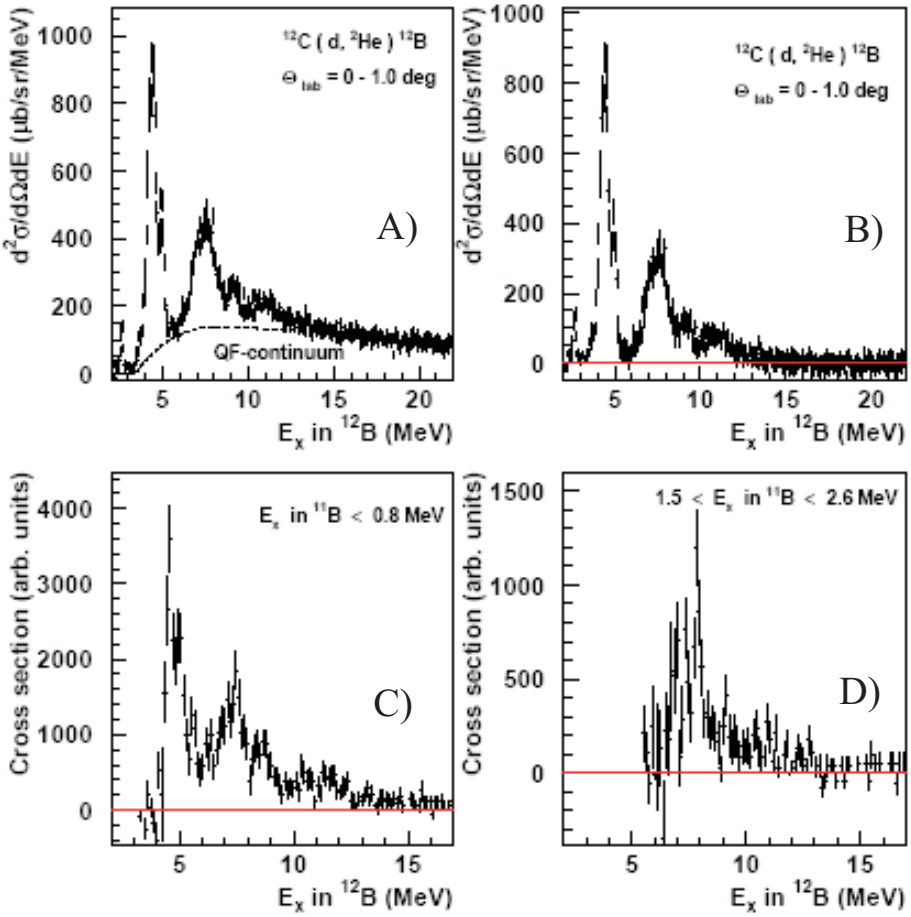

Figure 3.5 Comparison of ^{12}C(d,^{2}He)^{12}B and ^{12}C(d,^{2} He n)^{12}B results. *A*) ^{12}C(d,^{2} He)^{12}B spectrum with continuum background and estimation of the QFC contribution; *B*) ^{12}C(d,^{2}He)^{12}B spectrum after the subtraction of the QFC. Spectra for which a coincidence with the neutron populating the g.s and the first excited state in ^{11}B is required are shown in panels *C*) and *D*). Picture taken from [dH04].

Chapter 4

Experimental setup and methods

4.1 The $(d,^2He)$ experiment

The $(d,^2\mathrm{He})$ experiment presented in this thesis was performed at the KVI, Groningen. Figure 4.1 shows an overview of the AGOR (*Accelerateur Groningen Orsay*) facility existent at the KVI at the moment of our experiment. A deuteron beam produced in the CUPS ion source was accelerated to 171 MeV by the AGOR cyclotron and delivered, through the beam line, to the experimental area used for nuclear physics experiments. This experimental hall contains the small-angle large-acceptance detector (SALAD) and the Big-Bite Spectrometer (BBS) (see 4.1.1).

In the present experiment the BBS was used together with the EuroSuperNova (ESN) detection system (see fig. 4.1). The ESN detector consists of a focal plane detection system (FPDS) and a focal plane polarimeter (FPP) including two scintillator planes. A more detailed description of the detector will be given in section 4.1.4.

The $^{64}\mathrm{Ni}(d,^2\mathrm{He})$ measurements were done at three different angular settings: $\theta_{BBS} = 0°,\ 3°$ and $5°$. The intensity of the beam on the target was: $\sim 0.4\ nA$ for the measurement at $0°$, $\sim 0.6\ nA$ for the $3°$ setting and $\sim 1.6\ nA$ for the $5°$ setting. It was fixed by the rate limitations of the detection system. These limitations came from the dead time of the electronics and data acquisition system, which have to be kept small. The deuteron break-up contributions (see section 5.1) have also to be kept small; the deuteron break-up was the main limitation of the beam current for the measurement at $0°$.

The intrinsic resolution of the beam was about 300 keV. As the cyclotron

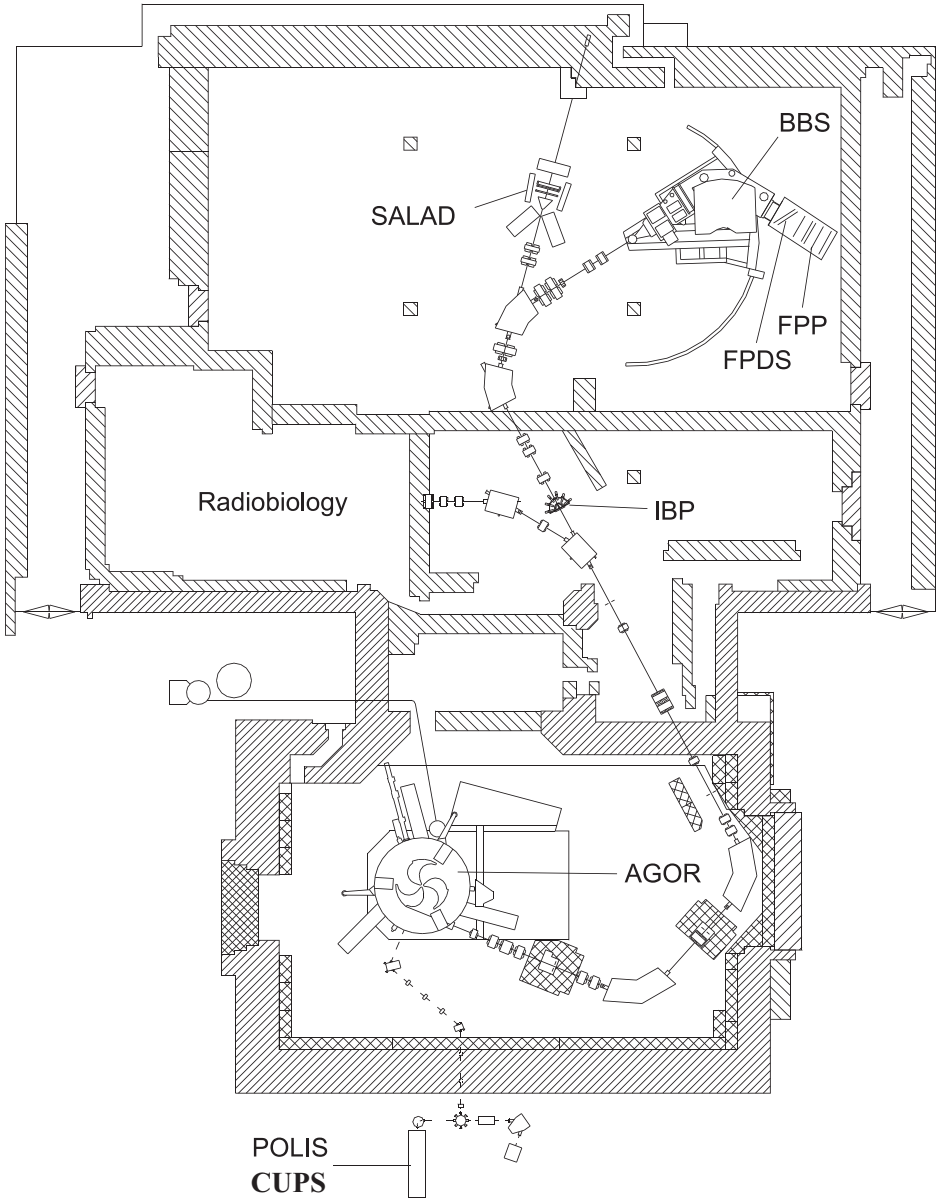

Figure 4.1 KVI floor plan at the moment of our experiment. The two existent ion sources CUPS (producing unpolarized beam) and POLIS (producing polarized beam) are indicated. The in-beam polarimeter (IBP) is used in experiments with polarized beams for determining the degree of polarization of the beam. (see text for a detailed description of the facility used in our experiment)

was operated at a RF frequency of 43.298 MHz, the time difference between two consecutive pulses was about 23 ns, each pulse having a length of about 2 ns. These properties of the primary beam have to be taken into account in the analysis of the acquired data (see chapter 5).

In order to improve the energy resolution the *dispersion-matching* technique was used: the beam line to the spectrometer was tuned to obtain an horizontal dispersion (the deuterons with different momenta arrive at different horizontal positions at the target location), the beam-spot becoming a few millimeters in the horizontal direction and about 1 mm in the vertical direction. This dispersion is then compensated (matched) by the intrinsic dispersion of the BBS. In this way, an energy resolution of about 110 keV was obtained for the ^{64}Ni 0° measurement while the intrinsic resolution of the beam was about 300 keV.

The measured ^{64}Ni target was a self-supporting metal foil with a thickness of 5.2 mg/cm^2 and 96.48 % enrichment. A self-supporting natural carbon foil with a thickness of 9.4 mg/cm^2 was measured for calibration purposes.

4.1.1 The Big-Bite Spectrometer

The BBS is a large momentum and angular acceptance magnetic spectrometer of the QQD-type, with a K value of 430 and a solid angle up to 13 msr. It is schematically drawn in figure 4.2.

The position of the two quadrupole magnets can be varied with respect to the dipole magnet, changing the properties of the spectrometer. Moving the quadrupole doublet closer to the dipole, the momentum acceptance is increased, but the angular acceptance is decreased. This is achieved in the operating mode "A" of the BBS. The inverse effect is obtained by moving the quadrupole doublet closer to the scattering chamber (the operating mode "C" of the BBS). In the present experiment, the BBS was used in the intermediate mode "B". The design parameters of the BBS in this mode are given in table 4.1.

For measurements with the $\Theta_{BBS} = 0°$ angular setting a Faraday cup was mounted inside the dipole, serving as beam stop and providing information about the beam current. For the other BBS angular settings (3° and 5°) the primary beam was stopped before the dipole magnet.

A more detailed description of the BBS can be found in e.g. [vdB95].

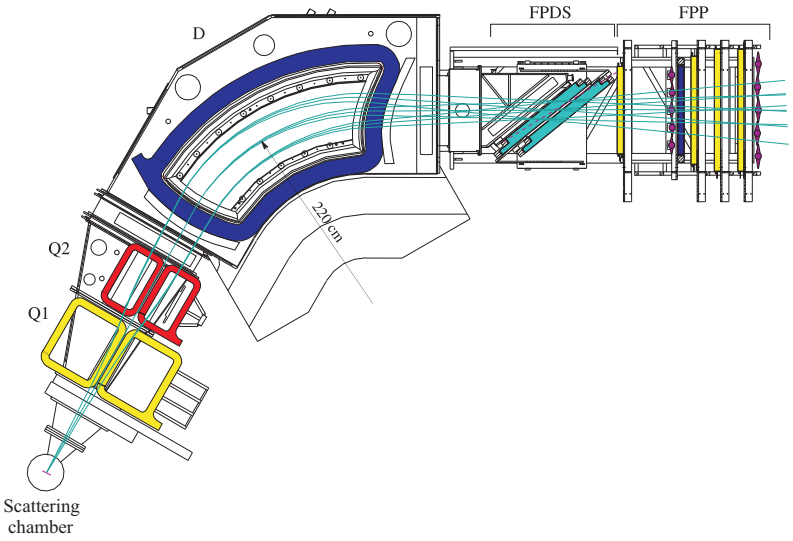

Figure 4.2 Cut through the symmetry plane of the BBS and the ESN detector system, consistng of a focal-plane detection system (FPDS) and a focal plane polarimeter (FPP). Possible particle trajectories are indicated on the figure. Particles with the same momentum are focused at the same position in the focal plane, independent of their initial direction.

Momentum bite $\frac{p-p_0}{p_0}$	19%
Solid angle $\Delta\Omega$	9.2 msr
horizontal opening angle $\Delta\theta$	66 mrad
vertical opening angle $\Delta\phi$	140 mrad
Momentum dispersion $D = (x\|\delta)$	2.54 cm/%
horizontal magnification $M_x = (\theta\|\theta)$	-0.45
vertical magnification $M_y = (\phi\|\phi)$	-10.1
momentum resolution $\frac{\Delta p}{p}$	2×10^{-4}
Radius of curvature ρ_0	220 cm
maximum magnetic field of dipole B	1.4 T
Bending limit K	430 MeV
Distance target – entrance aperture	81.7 cm

Table 4.1 Design parameters for the Big-Bite Spectrometer in mode B [vdB95].

4.1.2 The ion-optics of the Big-Bite Spectrometer

A charged particle can be transported through the BBS from the target position to the focal plane. In the dipole magnet of the BBS, this particle is forced by the magnetic field (B) to follow a circular trajectory with the radius ρ. The rigidity $B\rho$ will be linearly dependent on the momentum (p) of the particle:

$$B\rho = \frac{p}{q} = \frac{mv}{q} \tag{4.1}$$

where m, v and q are the relativistic mass, the velocity and the charge of the particle. The deviation of the momentum p of a particle from the momentum p_0 of a particle following the central track (ρ_0) of the spectrometer is $\delta = \frac{p-p_0}{p_0}$.

The coordinate system that we adopt is the following: The z axis is tangential to the axis defined by ρ_0. The horizontal axis (x) is perpendicular to z in the bending plane. The vertical axis (y) is perpendicular to the xz plane (perpendicular to the bending plane).

The imaging properties of an ion-optical system can be described by a transfer matrix which connects the coordinates at the target position ("the object") with the coordinates in the focal plane ("the image of the object"). The elements of this matrix are given by a Taylor series about the central ray [Han01, dH04]:

$$\alpha_t = \sum_{i,j,k,l} (\alpha \mid x^i\ \theta^j\ y^k\ \phi^l)\ x_{fp}^i\ \theta_{fp}^j\ y_{fp}^k\ \phi_{fp}^l, \tag{4.2}$$

with the target variables $\alpha = \delta_t,\ \theta_t,$ or ϕ_t. The coordinates in the focal plane are denoted by fp and the ones at the target position by t. The coefficients of eq. 4.2 are determined experimentally by using data from measurements with a multi-hole aperture ("sieve-slit") in front of the entrance of the spectrometer. For a detailed description of this procedure see refs. [Han01, dH04]. In the analysis of the data from the present experiment, the coefficients determined in ref. [dH04] have been used.

A precise determination of the scattering angles requires good angular resolution both horizontal and vertical. The good angular resolution is obtained by adjusting the magnetic fields of the quadrupoles. Typical angular resolutions achievable at KVI in $(d,^2\mathrm{He})$ experiments are $\sim 0.31^\circ$ (FWHM) for the horizontal angle (θ_t) and $\sim 0.46^\circ$ (FWHM) for the vertical angle (ϕ_t) [dH04].

4.1.3 The recoil corrections

Due to the kinematics of the reaction, particles leaving the rest nucleus in the same state can be scattered at different angles θ_r. Therefore they will have

different momenta and they will be detected at different positions in the focal plane. This is the effect of kinematic broadening and it has to be corrected for in the data analysis. The effect is described by the kinematic factor:

$$K = \frac{1}{p}\frac{\partial p}{\partial \theta r} \tag{4.3}$$

The factor K is measured in $\left[\frac{1}{\text{mrad}}\right]$ and can be calculated by using two-body kinematics codes like *kinema* developed by M. de Huu in 2000 [dH].

The kinematic broadening effect can be compensated by software corrections. In the present analysis the software corrections of V. Hannen [Han01] have been applied.

4.1.4 The detector and the acquisition system

The two outgoing protons from the (d,^{2}He) reaction were detected by using the ESN detector, which is located next to the focal plane of the BBS (see fig. 4.2 and fig. 4.3). The detector is composed by two different parts: the focal-plane detection system (FPDS) and the focal-plane polarimeter (FPP) including two scintillator planes. For a detailed description of the detector, electronics and acquisition system see refs. [Hag99, Han01, Han03].

The FPDS has two vertical drift chambers (VDC's), each of them consisting of a X- and a U-plane, with the wires of the U-plane tilted relative to the X-plane by 32.86°. In the present experiment the VDC's have been positioned at 39° to the central beam of the spectrometer (nearly parallel to the focal plane of the BBS). By using two VDC's, apart from determining the position, also the angle of the particle track at the focal plane of the spectrometer is determined.

The specifications of the VDC's are summarized in table 4.2.

The VDC's have alternating anode sense and guard wires enclosed by cathode foils. Through the preamplifier cards (see [Krü00]) which are mounted directly on the chambers, the sense wires are read out by time to digital converters (TDC's) type LeCroy3377 mounted on two CAMAC crates and set up for fast FERA (**F**ast **E**ncoding and **R**eadout **A**DC) data transfer mode.

When a proton passes through the VDC, the moving electron and ion clouds that are generated will induce signals on several neighboring wires (∼9 wires for the X plane and ∼7-8 wires for the U plane). Therefore, when acquiring an event, a condition on the number of adjacent wires that give a signal is imposed: at least 5 neighboring wires have to give a signal.

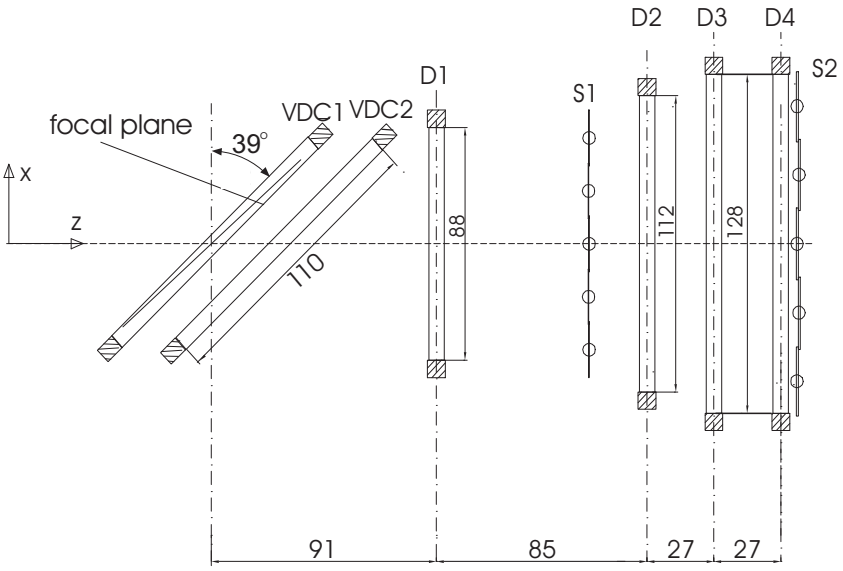

Figure 4.3 Vertical view of the EuroSuperNova detector. The indicated distances are in mm.

By using the information provided by the VDC's, both the angle and position of the particle in the focal plane of the spectrometer can be calculated and transfered to target position information via eq. 4.2.

The FPP has four multi-wire proportional chambers (MWPC's) and two scintillator planes (see fig. 4.3). Initially, the FPP was built for polarization measurements in (p, p') experiments. In this case an additional carbon analyzer is inserted between D1 and S1 as a secondary scatterer. In the case of the $(d,^2\text{He})$ reaction the carbon analyzer was removed and the FPP was used to identify the two protons from ^{2}He.

The specifications of the MWPC's are summarized in table 4.3. Each of the four MWPC's consists of an X and an Y-plane. As they are positioned perpendicular to the central ray, only one or two wires produce a signal when a proton passes. The signal of the wires is read by the LeCroy PCOS III system through the same preamplifier cards as in the case of the VDC's. Only the information about the position of the hit wires in an event is given. In $(d,^2\text{He})$ experiments this information is used for an online event processing that filters the events with single-track signature.

In the off-line data analysis, the information from the VDC's is com-

Table 4.2 Specifications of the VDC's of the ESN FPDS in the KVI (from refs. [Hag01, Han01])

Planes	X,U
Wire configuration	X(0°=horizontal) U(32.86°)
Active detection area	1030 × 367mm^2
Angle between VDC's and BBS central ray	39°
Total number of active wires	960
Number of sense wires	240(X), 240(U)
Wire spacing	4.2 mm
Sence wires thickness	20μm
Guard wires thickness	50μm
Distance wire-plane to cathode-foil	15mm
Spatial resolution (X × Y)	45 μm × 80 μm
Gas mixture	50% argon – 50% isobutane
Readout system	LeCroy
	3377 TDCs (FERA)

Table 4.3 Specifications of the MWPC's of the ESN FPP in the KVI (from refs. [Hag01, Han01])

Planes	X,Y
Wire configuration	X(0°=horizontal) U(90°)
Active detection area MWPC D1	840×400 mm^2
Active detection area MWPC D2	1080×520 mm^2
Active detection area MWPC D3 and D4	1240×960 mm^2
Total number of active wires	2896
Wire spacing	2.5 mm
Wires thickness	20μm
Distance wire-plane to cathode-foil (D1 and D2)	3mm
Distance wire-plane to cathode-foil (D3 and D4)	5mm
Spatial resolution (X × Y)	1.25mm × 1.25mm
Gas mixture	50% argon – 50% isobutane
Readout system	LeCroy
	PCOS III

bined with the one from the MWPC's for accurate track reconstruction (see ref. [Rak02]).

In the present experiment the third MWPC (both X and Y planes) was not used. The information from the other three MWPC's was sufficient for identifying the two protons from ^{2}He.

The two scintillator planes (S1 and S2) are placed between the first and the second MWPC and after the last MWPC. Each scintillator plane is composed of five overlapping plastic scintillator paddles positioned vertically. The scintillators are read out at both ends by Philips XP2262 photo-multipliers. The scintillator signals give information on energy loss of the particles crossing the scintillator and on their time-of-flight. This information is used in the analysis to suppress background events and to allow particle identification. But the main use of the signals produced in the scintillator planes is to serve as event triggers, activating the read-out procedure of the complete detector system (for a detailed description of the trigger scheme see ref. [Bäu04]).

Figure 4.4 gives a general view of the readout electronics and data acquisition system. The signals from the preamplifier cards (ASD-8B) mounted directly on the VDC's and MWPC's are transmitted to the converter modules that converts the LS-ECL signals in standard ECL signals. These are further transmitted to the CAMAC based TDC and PCOS modules, that realize the digital encoding of the data. The readout chain has five data branches: two for the TDC's system, two for PCOS system and one for the scintillator time-of-flight and time-over-threshold readout.

A VME-based readout and online data processing system has been developed in such a way that the acquisition and online processing of an event can be kept below $10\mu s$. The idea of this online data processing system is to acquire the data from the frontend electronics, to filter the valid events and to transmit only these valid events to a storage device.

Each branch transmits the data to a "first-in first-out" (FIFO) module (STR 7090), that buffers the event data and that is capable to handle all PCOS, FERA and TCC 3377 protocols.

The section that follows is composed by an Arbiter module (STR 8090/TRAN) and two digital signal processors (DSP's) based VME modules (STR 8090). The local readout bus (LRB) will realize the communication between the FIFO modules and the Arbiter and between the Arbiter and DSP's. The readout data structure allows to add many DSP modules, if it would be necessary to increase the computing power and to decrease the processing time. The role of the Arbiter is to detect a readiness of a complete event in

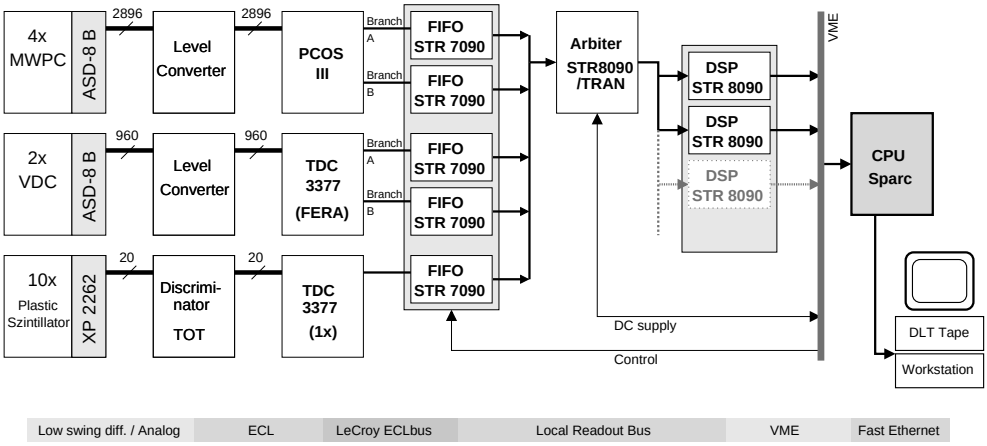

Figure 4.4 Drowing of data acquisition system (picture taken from ref. [Hag99])

the FIFO modules and to indicate the free DSP module for performing the software test. The DSP takes the data from the FIFO's and checks if the data from the MWPC's are consistent with two coincident proton tracks. This check contains the following conditions:

- each MWPC plane has to record at least one hit (except for the D3, that was not used in the present experiment);
- there must be two wire chambers with at least 3 hits.

After processing the event, the selected event data can be accessed by the VME controller. An Alpha *AXP-VME 4/288* CPU, running VxWorks as operating system, is residing in the VME crate. The Alpha is equiped with a fast Ethernet card used for transferring the data to the data acquisition system (a Linux PC) located outside the experimental hall (in the control room). The Linux PC writes all the incoming data to a DLT tape, and, at the same time, it sends a small amount of these data to another Linux PC, used for performing an online analysis of the data and monitoring the acquisition process.

4.2 The (^{3}He, t) experiment

The (^{3}He, t) experiment presented in this thesis was performed at RCNP, Osaka. A 420 MeV ^{3}He beam from the RCNP Ring Cyclotron was scattered on a 0.473 mg/cm^2 ^{64}Ni target. The outgoing tritons were momentum analyzed by the Grand Raiden (GR) Spectrometer and their positions and angles were measured in the focal plane of the GR.

The Ring Cyclotron uses primary beams extracted from the AVF Cyclotron. With this accelerator system various beams are produced: protons, deuterons, ^{3}He, α particles, light or heavy ions beams with total energies from 200 MeV up to 540 MeV, depending on the nature of the beam. The beams extracted from the Ring Cyclotron are transported to three experimental halls (see fig. 4.5). In the (^{3}He, t) experiment the west experimental hall, that contains the WS-course beam line and the Grand Raiden Spectrometer, was used.

4.2.1 The WS beam line

It was designed and built for high resolution spectroscopy experiments. It was built in a collaboration between different institutions: the RCNP, the Department of Physics of Osaka University, the Department of Physics of Kyoto University and Indiana University Cyclotron Facility (IUCF). An overview of this beam line is presented in fig. 4.6.

The WS beam line consists of five sections with dipole and quadrupole magnets:

The first section contains one dipole magnet with a bending angle of 40° and four small aperture quadrupole magnets grouped in pairs: a group is used for vertical focusing and the other for horizontal focusing. In this section the beam is bent 40° counterclockwise from the object point at the exit of the cyclotron and transported to the first double-focusing point BLP1 (Beam Line Polarimeter I).

The second section contains three dipole magnets (two with a bending angle of 41.5° and one with a bending angle of 32°). Four middle aperture quadrupole magnets, grouped in pairs, are situated in this section: two are used for vertical focusing and the other for horizontal focusing. In this section the beam is bent 115° clockwise and is focused on the second double-focusing point BLP2 (Beam Line Polarimeter II).

The third section contains two dipole magnets, one middle aperture quadrupole, that is used only in achromatic mode and one large aperture quadrupole used for vertical focusing. The horizontal focusing is ensured by the rotation of the entrance pole-face of the first dipole magnet of this section.

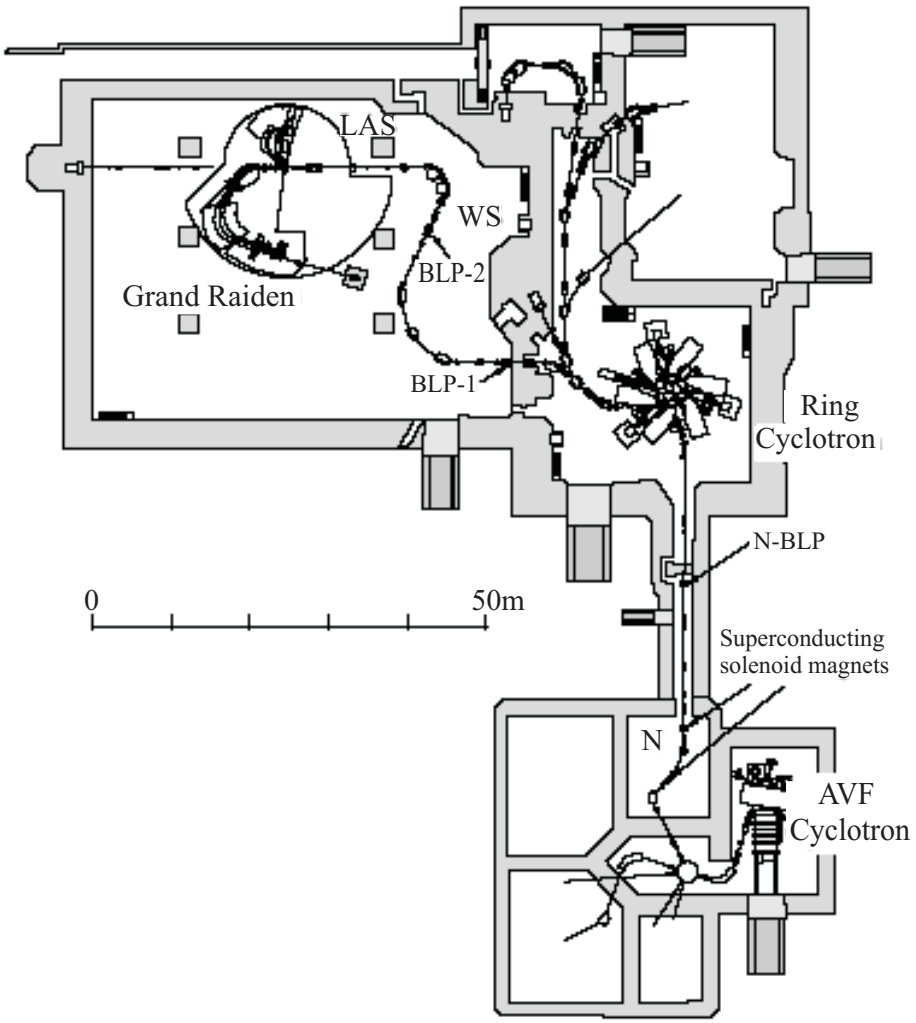

Figure 4.5 Floor plan of the experimental hall at RCNP (see text for details). Picture taken from ref. [Kaw02]

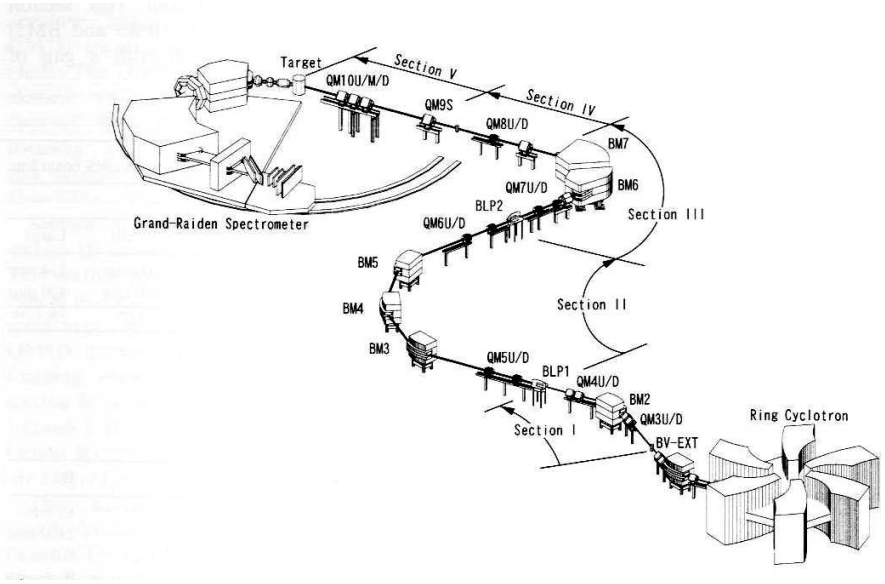

Figure 4.6 The WS-course (see text for details). Taken from ref. [Wak02]

The beam is bent back, 115° counterclockwise, in this section.

The lasts two sections (IV and V) are straight to the target point. Section IV contains a large aperture quadrupole (used for horizontal focusing) and a middle aperture quadrupole (for vertical focusing). The main function of this section is to increase the dispersion produced in the firsts three sections for the matching required for the GR. At the fourth double-focusing point, between section IV and V, a quadrupole magnet is placed. At this position, both horizontal and vertical focusing are accomplished. The horizontal beam size is large, as the dispersion is large, and there is a momentum spread of the beam. This special quadrupole, placed at this point in the beam line, can change the correlation between the momentum and the horizontal angle of the beam, the other ion-optical properties (e.g. the dispersion) remaining nearly untouched. The *angular dispersion matching* is realized with this quadrupole.

The last section has the role to focus the beam before the target. It contains three quadrupole magnets (with large aperture) placed symmetrically: two are used for horizontal focusing and one for vertical focusing.

As the GR spectrometer is characterized by large momentum dispersion and small magnification, a very large beam momentum dispersion at the target position is required in order to achieve the *lateral dispersion matching* (see section 4.2.3). On the other hand, due to the large dispersion, the beam spot

has a large horizontal size causing large scattering angle uncertainties of the order 20-30 mr [Fuj97]. These uncertainties are due to different scattering angles for different positions (at the target location) where the reaction can take place. Therefore an *angular dispersion matching* (see further fig. 4.9 *c*)) is required. The great worth of the WS beam line is the possibility to realize all the matching conditions: *focus* and *lateral dispersion matching* and also *angular dispersion matching* [Fuj02a, Wak02].

Apart from providing the required "matched beam", this beam line is also characterized by the following [Fuj97]:

• a point-to-point focus is achieved in the beam transport from one section to the next one;

• the ion-optical elements are placed symmetrically in order to simplify the adjustment of beam line parameters;

• special locations are foreseen for the accurate measurement of the beam polarization (in the case of an experiment using polarized beam)

4.2.2 The Grand Raiden Spectrometer

Although the RCNP Ring Cyclotron can deliver ^{3}He beams up to energies of 540 MeV (180 MeV/A), the RCNP magnetic spectrometer Grand Raiden imposes a lower limit for the ^{3}He particle energy. The spectrometer can analyze particles with a maximum rigidity $(B\rho)^{max}$=5.4 Tm, which corresponds to an energy of 450 MeV for tritons.

Similar to the WS beam line, the GR spectrometer was designed, constructed and dedicated for high resolution spectroscopy measurements at the Ring Cyclotron facility. A detailed description can be found e.g. in ref. [Fuj99b]. This spectrometer consists of two dipole magnets (D1 and D2), two quadrupole magnets (Q1 and Q2), a sextupole magnet (SX) and a multipole magnet (MP)as schematically drown in fig. 4.7. For the $(^3\mathrm{He}, t)$ experiment discussed in this thesis only the Q1, Q2, D1 and D2 magnets have been used.

The full capacity of the GR spectrometer is obtained when using also the sextupole and the multipole magnets, that could correct for higher order ion-optical aberrations. In the present experiments these corrections have been included in the analysis software.

An additional dipole magnet at the exit of D2, is used in polarized proton inelastic scattering experiments for rotating in-plane components of the polarization vector probes. It was not used in the present experiment.

The GR spectrometer is characterized by a high resolving power of $p/\Delta p$=37000 for a monochromatic beam spot size of 1 mm [Wak02]. Its char-

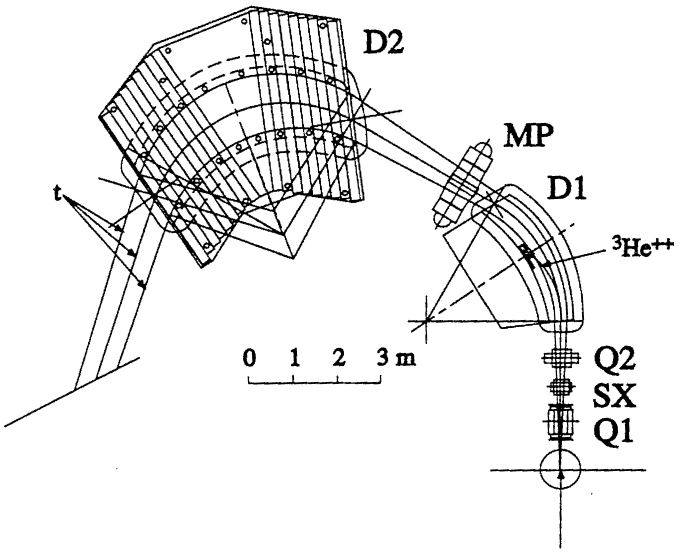

Figure 4.7 Horizontal cut along the mid plane of the Grand Raiden Spectrometer. Possible particle trajectories are indicated on the figure. Picture taken from [Wak].

Table 4.4 Design parameters for the Grand Raiden Spectrometer [Fuj99b, Wak].

Mean orbit radius	3 m
Total deflection angle	162°
Angular range	0° - 90°
Focal plane length	150 cm
Tilting angle of focal line	45.0°
Maximum magnetic field strength	18 Tm
Vertical magnification (M_y)	5.98
Horizontal magnification (M_x)	-0.417
Momentum dispersion (D)	15451 mm
Momentum range	5 %
Momentum resolution	37076
Acceptance angle-horizontal	±20 mr
Acceptance angle-vertical	±70 mr
Solid angle $\Delta\Omega$	5.6 msr
Maximum momentum B*ρ	5.5 Tm
Total weight	600 tons

acteristics are summarized in table 4.4.

When measuring with the spectrometer at 0°, a beam stop is placed inside the first dipole magnet in order to stop the $^3He^{++}$ particles. This was the only spectrometer angle setting used in the present experiment.

4.2.3 Ion-optics of beam line and spectrometer. Matching between beam line and spectrometer.

As already mentioned in section 4.1.2, a charged particle is transported along the beam line from the entrance point (the exit of the cyclotron) to the target position and, further, through the spectrometer, from the target position to the focal plane. Using the same coordinates as for the BBS (see section 4.1.2), the coordinates of the incident ^{3}He particle at the exit of the Ring Cyclotron (x_0, θ_0, δ_0) are changed by a transfer matrix, **B**, along the beam line to the target position (x_1, θ_1, δ_1). Another transfer matrix, **T**, which characterizes the reaction that takes place, will determine the coordinates of the outgoing particle at the target position (x_2, θ_2, δ_2). Finally, the transfer matrix, **S**, connects the coordinates of the outgoing tritons at the target position with the coordinates at the focal plane (x_{fp}, θ_{fp}, δ_{fp}). (see [Fuj97])

By combining **B**, **T** and **S**, the transformations of the x and θ coordinates from the entrance of the beam line to the focal plane of the spectrometer will be described by: [Wak02]:

$$\begin{aligned} x_{fp} &= x_0(s_{11}b_{11}T + s_{12}b_{21}) \\ &\quad +\theta_0(s_{11}b_{12}T + s_{12}b_{22}) \\ &\quad +\delta_0(s_{11}b_{16}T + s_{12}b_{26} + s_{16}C) \\ &\quad +\Theta(s_{12} + s_{16}K) \\ &\quad +higher\ order\ terms \end{aligned} \tag{4.4}$$

and

$$\begin{aligned} \theta_{fp} &= x_0(s_{21}b_{11}T + s_{22}b_{21}) \\ &\quad +\theta_0(s_{21}b_{12}T + s_{22}b_{22}) \\ &\quad +\delta_0(s_{21}b_{16}T + s_{22}b_{26} + s_{26}C) \\ &\quad +\Theta(s_{22} + s_{26}K) \\ &\quad +higher\ order\ terms \end{aligned} \tag{4.5}$$

The suffices 1, 2 and 6 of the matrix elements s_{ij} and b_{ij} $(i, j = 1, 2, 6)$ represent the respective coordinates in the focal plane x_{fp}, θ_{fp} and δ_{fp}. Θ is the effective scattering angle relative to the central ray. $\Theta = \theta_2 - \theta_1$, where θ_1 is the angle of an incident ^{3}He particle (see fig. 4.8) and θ_2 is the angle of the outgoing t particle relative to α. The last one is the angle between the direction of the incident beam at the target position and the central ray. K is the "first order" kinematic factor:

$$K = \frac{1}{p_{out}} \frac{\partial p_{out}}{\partial \alpha}, \tag{4.6}$$

where p_{out} is the momentum of the outgoing triton at the target position. The factor C is the "dispersion matching factor", defined as:

$$C = \frac{p_{in}}{p_{out}} \frac{\partial p_{out}}{\partial p_{in}}, \tag{4.7}$$

with p_{in} the momentum of the incident ^{3}He particle at the target position [Fuj97, Fuj01b]. For elastic scattering C=1. The target function,

$$T = \frac{cos(\alpha - \Phi_T)}{cos\Phi_T}, \tag{4.8}$$

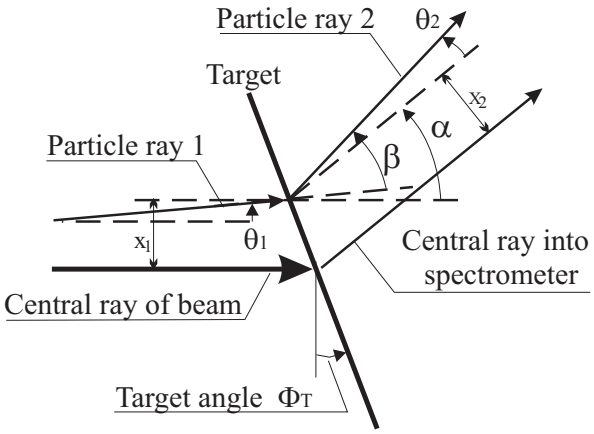

Figure 4.8 Schematic representation of the scattering of an incident particle with coordinates (x_1, θ_1) relative to the central ray of the beam and spectrometer; the coordinates of the outgoing particle are (x_2, θ_2). α is the scattering angle of the central ray. Φ_T is the angle made by the target and the normal to the beam direction. $\beta = \alpha + \theta_2 - \theta_1$ is the "absolute" scattering angle of a specific particle. The "effective" scattering angle of the particle relative to the central ray is $\Theta = \theta_2 - \theta_1$. Figure taken from ref. [Fuj02a].

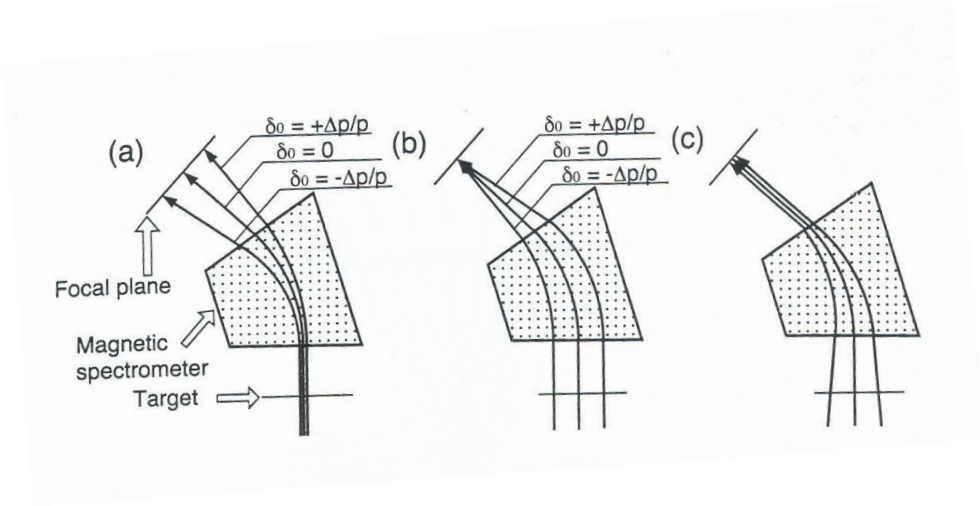

Figure 4.9 Illustration of ion trajectories under different matching conditions of beam line and magnetic spectrometer: (a) achromatic beam transportation; (b) *lateral dispersion matching* in the beam transportation is realized; (c) both *lateral dispersion matching* and *angular dispersion matching* are realized. The lines represent trajectories for particles with different Δp values within a beam. Taken from ref. [Fuj02a].

connects the scattering angle of the central ray α to the target angle Φ_T (see fig. 4.8).

In order to obtain the best resolving power of the system (the best resolution), the beam line settings should be matched to those of the spectrometer (as already mentioned in section 4.1). The matching conditions are schematically illustrated in fig. 4.9 for elastic scattering at 0° assuming a beam with very small emittance. At 0° the kinematic constant is $K = 0$.

Fig. 4.9(a) shows the beam with an achromatic focus at the target. Particles with different Δp values impinging on the same position at the target are "momentum analyzed" by the spectrometer and the achievable resolution is limited to the beam momentum spread. Fig. 4.9(b) shows the beam when *momentum dispersion matching* is realized. Particles with different Δp values hit the target at different positions on the target (dispersive monochromatic focus). The dispersion of the beam at the target is compensated by the dispersion of the spectrometer and the achromatic focus is realized in the focal plane of the spectrometer. The achievable resolution, therefore, is to first order not

affected by the beam momentum spread. But, due to the large beam spot size required for the momentum dispersion matching, particles with different Δp cross the focal plane with different angles θ_{fp}, so the angle measurements are loosing precision. Accurate angle measurements are possible by adjusting the incident angles of particles with different Δp values, by realizing *angular dispersion matching* (see fig. 4.9(c)). In this way, particles with different momenta that excites the same levels in the target nucleus and which are scattered at the same angle arrive at the same angle and the same position in the focal plane.

The transfer matrix that connects the coordinates of the tritons at the target position with the coordinates at the focal plane is given by a Taylor expansion around the central ray. In order to improve the vertical angle resolution, the ion-optical properties of the GR spectrometer in vertical direction in the transfer matrix formalism have to be considered:

$$\begin{aligned} y_{fp} &= (y|y)y_2 + (y|\phi)\phi_2 \\ &\quad +(y|yx)y_2x_2 + (y|y\theta)y_2\theta_2 + (y|y\delta)y_2\delta_1 \\ &\quad +(y|\phi x)\phi_2x_2 + (y|\phi\theta)\phi_2\theta_2 + (y|\phi\delta)\phi_2\delta_1 \\ &\quad + \textit{higher order terms}, \end{aligned} \tag{4.9}$$

where y_2 and ϕ_2 are the vertical position and vertical angle at the target location and x_2 and θ_2 are the horizontal position and angle at the target location. δ_1 is the fractional momentum spread of the incoming ^{3}He particles to the target. Because along the beam line the energy (implicit momentum) of the particles was not changed, the fractional momentum spread of ^{3}He particles at the target position will have the same value as at the entrance of the beam line ($\delta_1 = \delta_0$).

The results of the ion-optical calculations for three different settings are depicted in fig. 4.10:

(a) "focus mode" of GR: the term $(y|\phi)$ from eq. 4.9 is zero for the central ray (R=300 cm)

(b) "over-focus mode": the strength of the first quadrupole magnet, Q_1, of GR is increased and the term $(y|\phi) > 0$

(c) " under-focus mode": the strength of Q_1 is decreased and $(y|\phi) < 0$.

Practically in the "over-focus" and in the "under-focus" modes the particles with different outgoing angles from the target ϕ_t are transported to different vertical positions in the focal plane y_{fp}, therefore it is possible to obtain the ϕ_t values from the measured y_{fp} values. These ion-optical modes are called "off-focus modes".

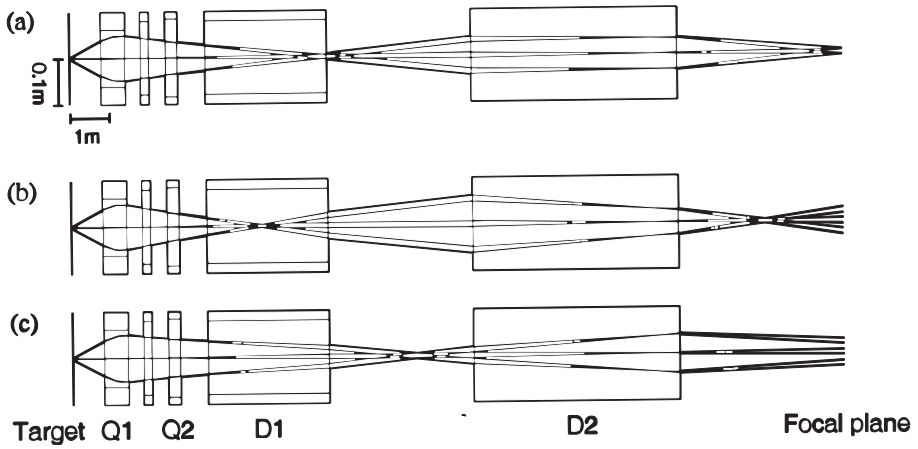

Figure 4.10 The vertical trajectories of the tritons with $\phi_t = 0, \pm 46$ mrad and $y_t = \pm 1$ mm for different focusing modes of the GR: (a) normal focus, (b) over-focus and (c) under-focus mode. Q_1, Q_2, D_1 and D_2, are the spectrometer quadrupole and dipole magnets (see fig. 4.7). Picture taken from ref. [Fuj01b].

For calibrating the vertical components of the scattering angle ϕ_t in "off-focus modes", the $(y|\phi)$ and the $(y|\phi\theta)$ terms of eq. 4.9 have to be known. The other terms and higher order terms are expected to induce ambiguities in relating the $(y|\phi)$ to ϕ_t. From ion-optical calculations for the GR, it is expected that the contributions of second order terms are small (less than 1 mm). The largest ambiguity comes from the vertical beam spot size as the vertical magnification is large ($(y|y) \sim 6$) [Fuj01b]. Also the horizontal beam spot size induces an ambiguity.

The accurate determination of ϕ_t from the y_{fp} measurements in "off-focus modes" depends on the proper adjustment of the Q1 strength and on finding the proper beam line settings (in principal, the settings of the quadrupole magnet placed between the last two sections of the WS beam line) in order to diminish the mentioned ambiguities.

Measurements with a multi-hole aperture ("sive-slit") were used for reconstructing the coordinates at the target from the measured coordinates at the focal plane and for diagnosing the angular dispersion matching.

Following Wakasa et al. [Wak02], the conditions for *lateral* and *angular dispersion matching* can be fulfilled by the following settings for the matrix

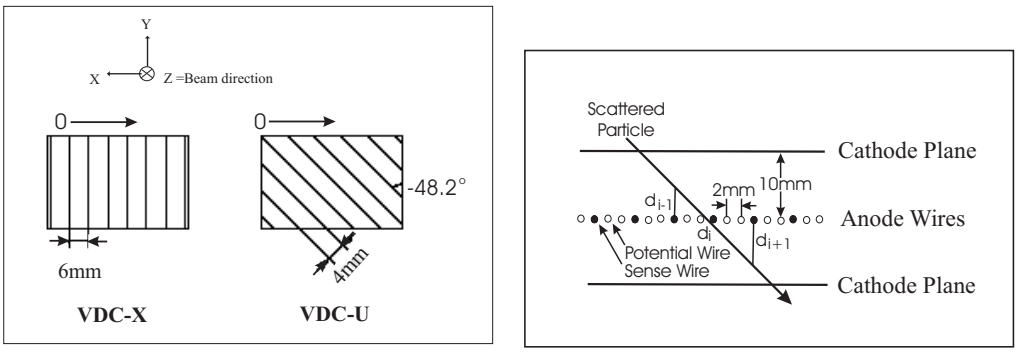

(a) (b)

Figure 4.11 *a*) Schematic representation of VDC's X and U planes; *b*) Cut through a VDC wire plane

elements of the beam line (see eq. 4.4,4.5):

$$b_{12} = -\frac{s_{12}}{s_{11}} b_{22} T \tag{4.10}$$

$$b_{16} = -\frac{s_{16}}{s_{11}}(1 + s_{11}s_{26}K - s_{21}s_{16}K)\frac{C}{T} \tag{4.11}$$

$$b_{26} = (s_{21}s_{16} - s_{11}s_{26}C) \tag{4.12}$$

At the same time, the spectrometer settings should be:

$$s_{12} = -s_{16}K \tag{4.13}$$

4.2.4 The detection and data acquisition system

The detector used in the (^{3}He, t) experiment has two vertical drift chambers (VDC's) [Nor91] used for position and angle measurement at the focal plane of the GR spectrometer and two plastic scintillators placed behind the VDC's, used for particle identification and fast timing trigger purposes.

The specifications of the VDC's are summarized in table 4.5. Each of them consists of two anode wire planes (X and U). The figure 4.11 shows the configuration and structure of each wire plane. The signals from the anode sense wires were fed to preamplifier cards and further discriminated by LeCroy 2735DC cards. Timing information was digitized by using LeCroy 3377 drift chamber TDC's.

The two plastic scintillators used for particle identification and triggering were very thin (3 mm and 10 mm) in order to reduce multiple scattering. They

Table 4.5 Specifications of the VDC's (from refs. [Nor91, Kaw02])

Planes	X,U
Wire configuration	X(0°=horizontal) U(-48.2°)
Active detection area	1150 × 120 mm^2
Number of sense wires	192(X), 208(U)
Cathode-anode gap	10 mm
Anode wire spacing	2 mm
Sense wire spacing	6 mm (X), 4 mm (U)
Sence wires thickness	20 μm
Potential wires thickness	50 μm
Cathode thickness	10 μm
Applied voltage	-5.6 kV (cathode)
	-350 V (X), -500 V (U) (potential wire)
Spatial resolution (X × Y)	45 μm × 80 μm
Gas mixture	71.4% argon + 28.6% isobutane
	+ evaporated iso-propyl-alcohol
Pre-amplifier	Le Croy 2735DC
Readout system	LeCroy
	3377 TDCs (FERA)

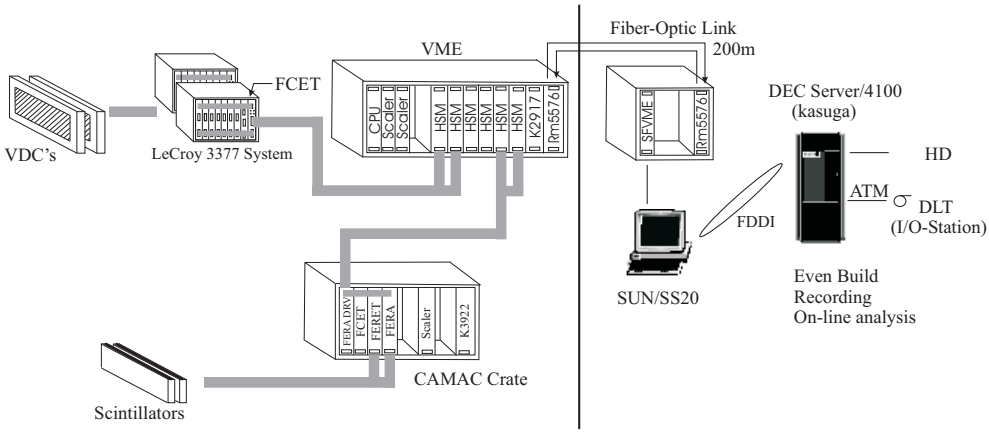

Figure 4.12 Illustration of the data acquisition system used in the $(^3\mathrm{He}, t)$ experiment at RCNP.

were placed in parallel with the VDC's. The scintillation light was detected by photo-multiplier tubes (PMT) on both sides of the scintillators. Signals from the PMT's were digitized by LeCroy FERA and FERET systems.

A schematic view of the acquisition system is presented in fig. 4.12. The digitized data from the detectors were transferred in parallel via the ECL busses to the high speed memory modules (HSM's) in the VME crate. Before the data transfer an event header, an event number and input register words were attached to the data by using the Flow Controlling Event Tagger (FCET) module. Further, through the VME bus, the data stored in the HSM's were copied to a VMIC5576 reflective memory module (Rm5576) by an MC68040 based CPU board with OS/9 operating system. The data from RM5576 in the experimental room were automatically copied to another RM5576 in the control room through a fiber-optic cable ring. The SUN work station readed the data from the RM5576 in the control room and transferred them to an IBM RS/6000 SP station via the FDDI line. Finally, the data were stored in a large hard disk connected to the work station. The event reconstruction and online data analysis were also performed on this computer.

A typical dead time for an event was less than 30 μs. The life time of the data acquisition system was about 97%. The intensity of the beam was kept around 30 nA.

Chapter 5

$(d,^2\mathrm{He})$ analysis procedure, results and discussion

The coincident measurement of the two protons from ^{2}He imposes a complex analysis procedure. In order to obtain correct cross sections, that have to be related to the B(GT)'s, a spectrum free of background is required. The background subtraction procedure is discussed in section 5.1. As absolute cross sections are needed, the spectra have to be corrected for the limited acceptance of the spectrometer. A detailed description of this procedure is given in section 5.2. The cross section calculations and the obtained excitation energy spectra, free of background and corrected for the spectrometer acceptance, are presented in section 5.3. The cross section of peaks corresponding to individual levels was determined by fitting the spectra obtained at different scattering angles (see section 5.4); their angular distributions have been analyzed in section 5.5. Finally, the $B(GT)$ for individual levels in the low excitation energy region have been calculated; the procedure and results are given in section 5.6. A discussion of the experimental results is given at the end of this chapter.

5.1 Background subtraction

For a deuteron beam of 170 MeV, the angular and momentum acceptance of the BBS (see tab. 4.1) limit the internal energy of the detected two-proton system to $\epsilon \leq 1$ MeV. At these internal energies, the two protons from ^{2}He are mainly in the $^1\mathrm{S}_0$ state with only a few percent contributions from higher partial waves [Kox93]. Therefore the spectrometer acts as a filter for GT transitions. Nevertheless, the software limitation $\epsilon \leq 1$ MeV is also imposed in the analysis.

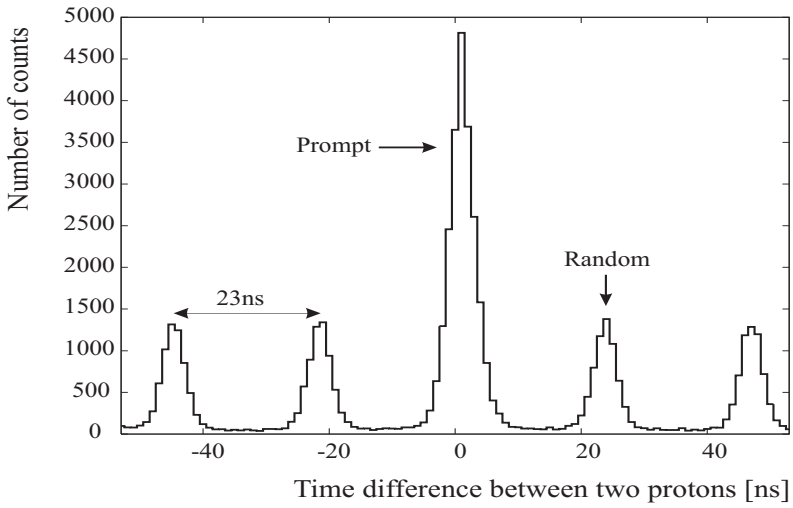

Figure 5.1 The time difference between the two detected protons. The resolution of a peak is about 2 ns. The difference between two consecutives centroids is of about 23 ns.

It was already discussed that, especially at very forward angles, the detection of the two protons from ^{2}He takes place in the presence of a huge proton background, due to the deuteron breakup reactions. The cross sections of these processes are several orders of magnitude higher than the ones for the (d,^{2}He) reaction [Rak02]. In order to realize the background reduction the timing information from the VDC's is used. Figure 5.1 shows the plot of the time difference Δt between the two detected protons in an event. The peak at Δt=0 ns represents the prompt coincidences and it corresponds mainly to (d,^{2}He) events. The other peaks, which are nearly equal in height, correspond to random coincidences. The time difference of 23 ns between two peaks is the same as the time difference between two consecutive cyclotron pulses (see 4.1). This indicates that the random peaks represent coincidences of protons from different beam pulses, that have mainly a deuteron breakup origin.

By gating on the Δt=0 ns peak, already an important reduction of background is obtained. However, the prompt peak contains also contributions from random coincidences. By imposing a gate on a random peak ($\Delta t \neq$0 ns), the shape of the background that has to be subtracted from the spectrum gated on the prompt peak is given. The correction of the measured ^{64}Ni(d,^{2}He)^{64}Co spectrum following this procedure is presented in fig. 5.2. The spectrum ob-

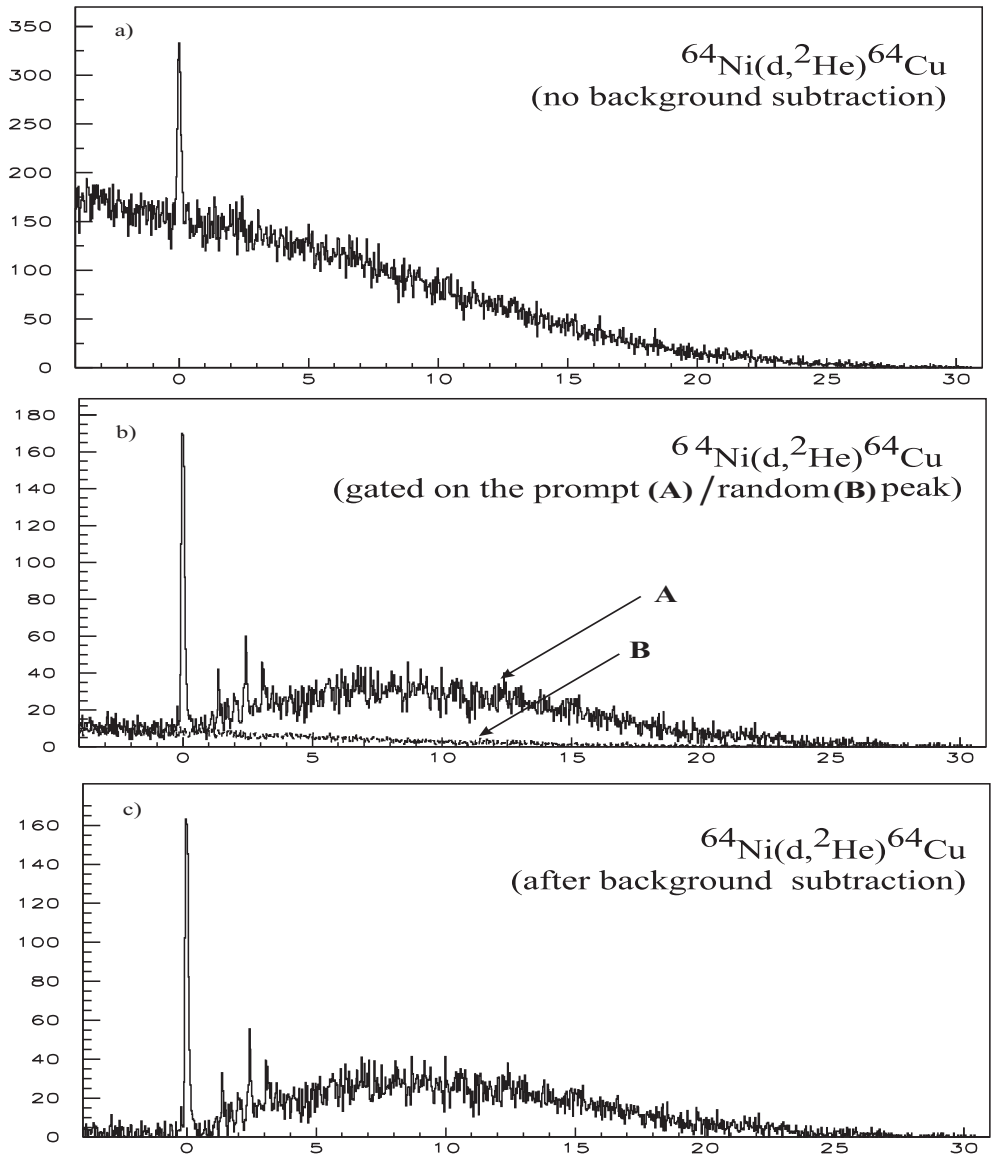

Figure 5.2 Illustration of the background subtraction procedure. a) the spectrum without any background subtraction. b) the spectrum (A) when a gate on the prompt coincidence is imposed and the spectrum (B) gated on a random coincidence peak. c) - the spectrum free of background (obtained by subtracting B from A).

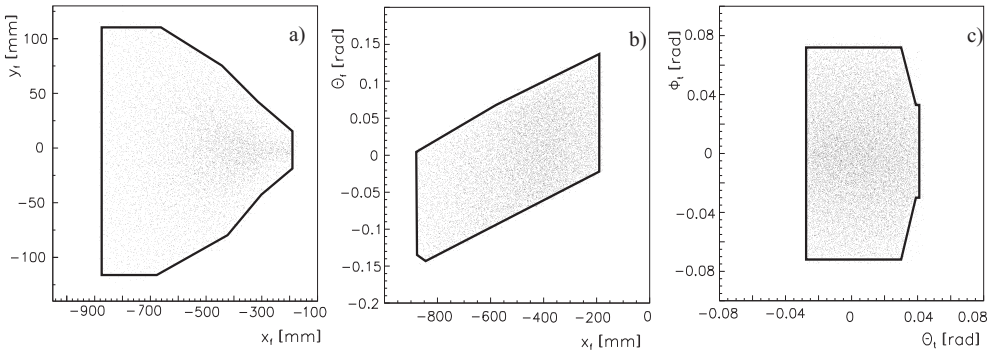

Figure 5.3 Grafical cuts defining the acceptance of the spectrometer. These cuts are used in the Monte Carlo simulation in order to determine the acceptance of the spectrometer for the two correlated protons from the ^{2}He in the ^{64}Ni(d,^{2}He)^{64}Co reaction. The figures show the accepted regions in the vertical position versus the horizontal position at the focal plane diagram (a), in the horizontal angle versus the horizontal position at the focal plane diagram (b) and in the vertical angle versus the horizontal angle at target position diagram (c). The applied two-dimensional cuts are shown as full lines.

tained by plotting a part of the raw data is given in fig. 5.2 a). A gate on the prompt peak was imposed and the resulting spectrum (A) is given in fig. 5.2 b). In this picture the background obtained by an average over the 4 neighbouring random peaks is also plotted (B). By subtracting the spectrum B from the spectrum A, the final background corrected spectrum is obtained - fig. 5.2 c). The lack of counts below E_x=0 MeV indicates that the procedure works well.

5.2 Acceptance corrections

In order to calculate absolute cross sections, the acceptance of the spectrometer for the two correlated protons has to be evaluated. This was done by using a Monte Carlo simulation.

The (d,^{2}He) three body reaction was treated as the result of two independent two-body reactions (see fig. 2.4). In the first step the ^{2}He is considered a bound particle, while it's decay into the two protons is assumed in the second step. For the first step the excitation energy of the residual nucleus, the internal energy of the ^{2}He (in the interval 0 - 1 MeV), the polar θ and azimuthal ϕ scattering angles are randomly generated. A supplementary condition on

the uniformity of the distribution in $cos\theta$ has to be accomplished for providing equal statistics in every solid-angle bin. For the second step, an isotropic angular distribution of the decay of ^{2}He into two protons in the ^{2}He center of mass is assumed.

In this way the complete set of kinematic variables for the two protons at the target position is obtained (x_t, y_t, θ_t, ϕ_t). By using the technique discussed in section 4.1.2 and the same experimentally determined coefficients, the transportation of the two protons from the target position through the spectrometer to the focal plane can be simulated. The coordinates in the focal plane are obtained in this way (x_{fp}, y_{fp}, θ_{fp}, ϕ_{fp}). By imposing two-dimensional gates on the focal plane coordinates of both protons "secure" regions can be selected for detecting the two protons. These gates have been defined by using the experimental data and are applied also in the analysis of the measured data. They are shown in fig. 5.3 *a*) and *b*). The set of kinematic variables for the two protons that can be detected at the focal plane will be obtained (x'_{fp}, y'_{fp}, θ'_{fp}, ϕ'_{fp}). Starting from these coordinates, the target coordinates of the protons are calculated again by transporting these focal-plane coordinates back to the target position, as done for the experimental data. An additional gate on the scattering angles at the target position (see fig. 5.3 *c*)) is applied. The complete set of variables for each proton after its transport from the target, through the spectrometer, to the detector and back is obtained (x'_t, y'_t, θ'_t, ϕ'_t). The new energy spectrum is produced . By dividing this spectrum by the simulated one, corresponding to (x_t, y_t, θ_t, ϕ_t), the correction function for the acceptance of the spectrometer is obtained.

As an example, fig. 5.4 shows the correction function for the case of the BBS angle setting at 0° and for ^{2}He scattering angles between 0° and 1°. In the analysis, this function is taken into account by defining an effective solid-angle

$$\Delta\Omega_{eff} = f_{corr}\dot{\Delta}\Omega, \tag{5.1}$$

which is then used in eq. 5.2 for calculating the experimental double-differential cross section. As for the experimental data a binning of $\Delta E_x = 35$ keV has been used, the same energy binning has to be used for the determined correction function. The solid angle intervals have also to coincide with the ones of the experimental situation ($\Delta\Omega_{sim} = \Delta\Omega$). As f_{corr} is known to be only slowly varying with E_x, in order to diminish the statistical uncertainty originating from the Monte Carlo simulation, the correction function was fitted with a Gaussian. The result of the fit is shown in fig. 5.4.

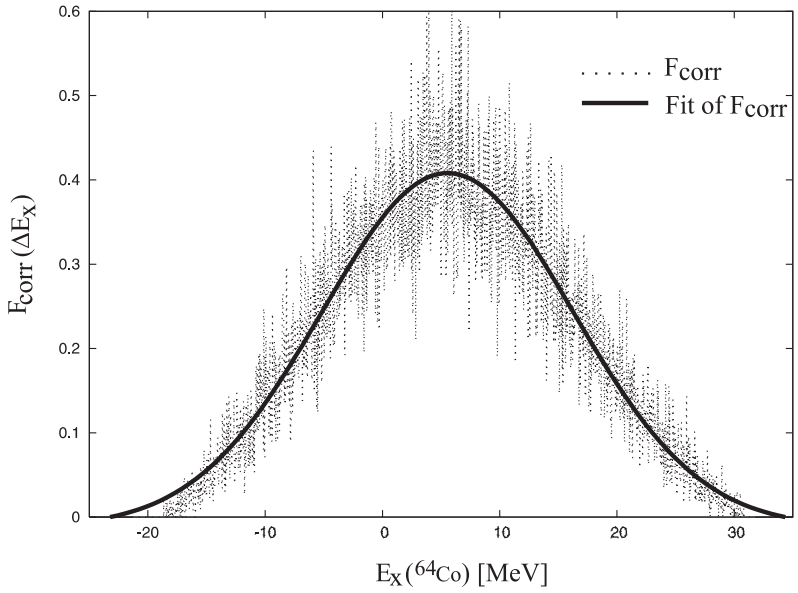

Figure 5.4 The acceptance function for ^{2}He particles scattered between 0° and 1° on the ^{64}Ni target for the BBS angle setting at 0°. A condition on the internal energy of ^{2}He is also imposed: $\epsilon \leq 1$ MeV.

5.3 Cross section calculation

The double-differential cross section for the (d,^{2}He) reaction in our typical experimental conditions and for the energy and solid angle bin ΔE and $\Delta\Omega$ was calculated by:

$$\frac{d^2\sigma}{d\Omega dE} = 0.266 \frac{A}{\mu} \frac{1}{Q(1-\tau)} \frac{N_{\Delta\Omega,\Delta E}}{\Delta\Omega_{eff}\Delta E} \frac{1}{D} \text{ [mb/sr/MeV]} \qquad (5.2)$$

where:

A = the mass of the target (in g/moll)
μ = the thickness of the target (in mg/cm^2)
$Q(1-\tau)$ = the effective charge
Q = the integrated charge (in nC)
τ = the dead time (in %)
$N_{\Delta\Omega,\Delta\ E}$ = the number of counts in the bin $\Delta\Omega\Delta E$
$\Delta\Omega_{eff}$ = the effective solid angle (in sr) as defined by eq. 5.1
$\Delta\ E$ = the energy bin (in MeV)
D = the detection probability (it was measured to be around 90% [Bäu04])

As already mentioned, the same energy and solid angle bin was used for determining the correction function for the acceptance of the system.

Calibration measurements by using a ^{nat}C target were done every 4 hours. The reference value for the cross section of the ^{12}C(d,^{2}He)^{12}B gs peak with $\Theta_{cm} \leq 1^\circ$ is dσ/dΩ = 2.22 mb/sr, as determined in ref. [Bäu04]. The cross section obtained for different runs of the present experiment was varying by about $\pm$15% around this value. Therefore an error on the cross section of 15% was deduced. This error accounts for different uncertainties, but the main is due to the determination of the correction function for the acceptance of the spectrometer (see section 5.2). The accuracy of the simulation was tested by M. de Huu [dH04] by comparing the ratio between excitation energy spectra taken at different magnetic field settings of the BBS with the result of the simulation for these settings. An accuracy of 10% was deduced. The uncertainty in measuring the integrated current and detector efficiency have also to be taken into account.

To produce angular distributions, spectra at four different scattering angles were produced by using measurements taken with three BBS angular settings. The $\theta_{BBS} = 0^\circ$ measurement was divided into two angular bins: 0° - 1° and 1° - 2°. For statistical reasons, the $\theta_{BBS} = 3^\circ$ measurement was used with only one angular gate: 2.5° - 4.5°. Similarly, the $\theta_{BBS} = 5^\circ$ measurement was also used with only one angular gate: 4.5° - 6.5°.

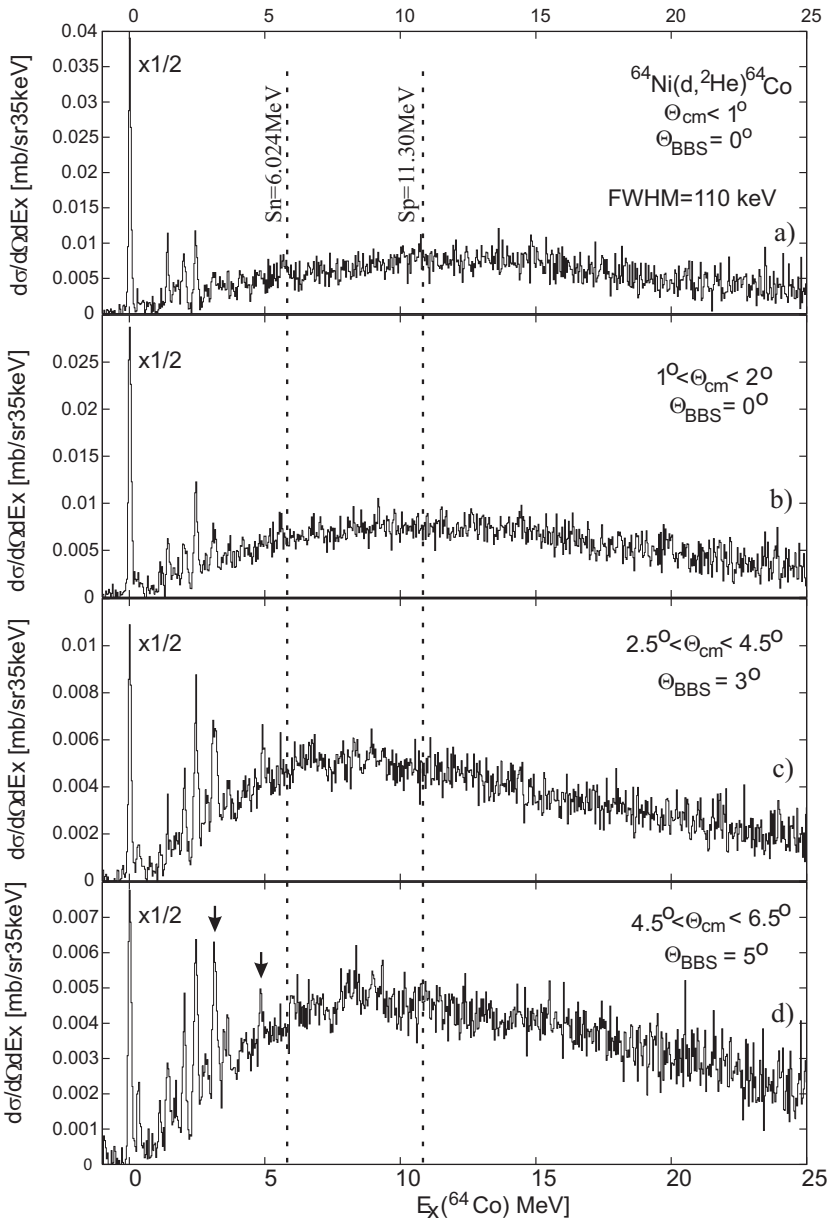

Figure 5.5 Double-differential cross sections of the ^{64}Ni$(d,^2\mathrm{He})^{64}$Co reaction for different scattering angle gates. The BBS angle settings as well as the scattering angle gates are indicated in the figure. The energy resolution for the 0° spectrum ($\Theta_{cm} \leq 1°$) is ∼110 keV. The neutron (S_n) and proton (S_p) separation energies are also indicated on the figure. Peaks corresponding to $\Delta L \geq 1$ levels are indicated by small arrows in the lowest pannel.

In this way, the spectra for $\Theta_{cm} = 0.5°$, $1.5°$, $3.5°$ and $5.5°$ were produced. They are plotted in fig. 5.5. Because of the considerable difference in intensities between the g.s. peak and the rest of the spectra, the g.s. peak was scaled by a factor of 1/2.

Several discrete states below 3 MeV can be observed. At higher excitation energies the level density is too high and broad structures become dominant.

5.4 Fit of the spectra

The program `fytik` [Sof] was used for fitting the spectra in the low excitation energy region. The fitting procedure is described below.

The energy resolution achieved in this experiment was around 110 keV allowing the separation of the g.s. peak from the other peaks corresponding to known levels. The peaks were fitted by using a Gaussian shape. As the particle threshold in ^{64}Co is at $E_x = 6.024$ MeV, it is not expected for the levels in the lower excitation energy region to have an observable natural width. Therefore, the width determined for the g.s. peak was imposed also for the others. There was no reason to include background contributions in this low energy region. This assumption is confirmed by the cross section for $\Theta_{cm} \leq 1°$ (see fig. 5.6) reaching 0 at $E_x = 2.6$ MeV.

All peak positions and intensities were allowed to vary when fitting the $\Theta_{cm} \leq 1°$ spectrum. The result of this fit is presented in fig. 5.6 and included in table 5.3 that shows the result from our ^{64}Ni(d,^{2}He)^{64}Co study. Apart from the 1.979 MeV level, all the obtained levels below 2.1 MeV had a counterpart in the literature. There is no information concerning higher energy states in the compiled data.

For higher angle spectra, a small number of constraints had to be used concerning the positions of several peaks, which were allowed to vary only in a narrow region around the value indicated in literature (below 2.05 MeV), or around the value obtained when fitting the $\Theta_{cm} \leq 1°$ spectrum.

The result of the fit of these spectra is presented in figs. 5.7 - 5.9 and table 5.3. The uncertainty on the obtained energies of the levels was determined by combining the information from the fit of the four spectra as well as the information from multiple fits of the same spectrum when imposing or not different constraints. The fitting error on the obtained peaks cross section varies from about 2% for the g.s. peak up to 50% for the very weakly excited components of the triplets at 1.7 MeV or at 2.4 MeV.

The four spectra were fitted also by using the program `FIT` [Str] and two different peak shapes: Gaussian and Gaussian plus exponential tails. The

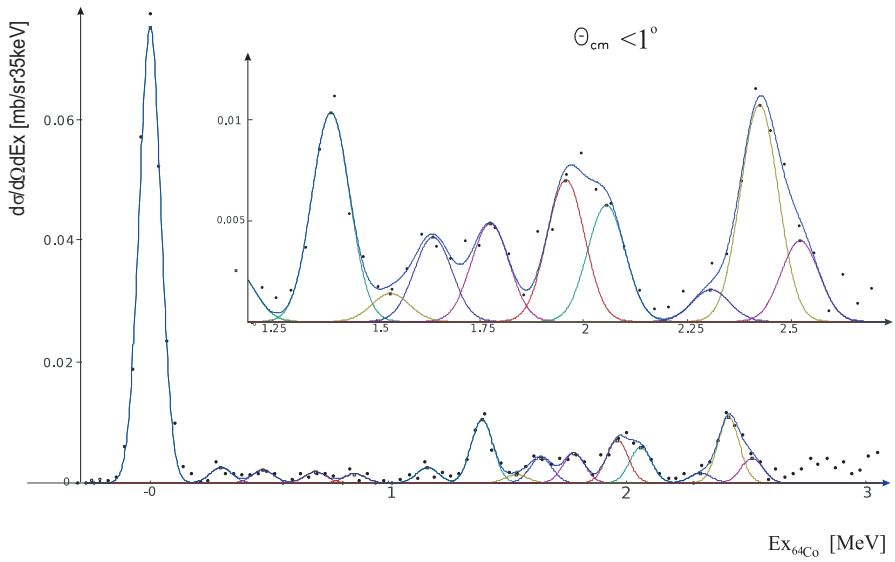

Figure 5.6 Fit of the ^{64}Co $\Theta_{cm} = 0.5°$ spectrum. The region between 1.2 and 2.7 MeV was enlarged and given as an insert in this figure.

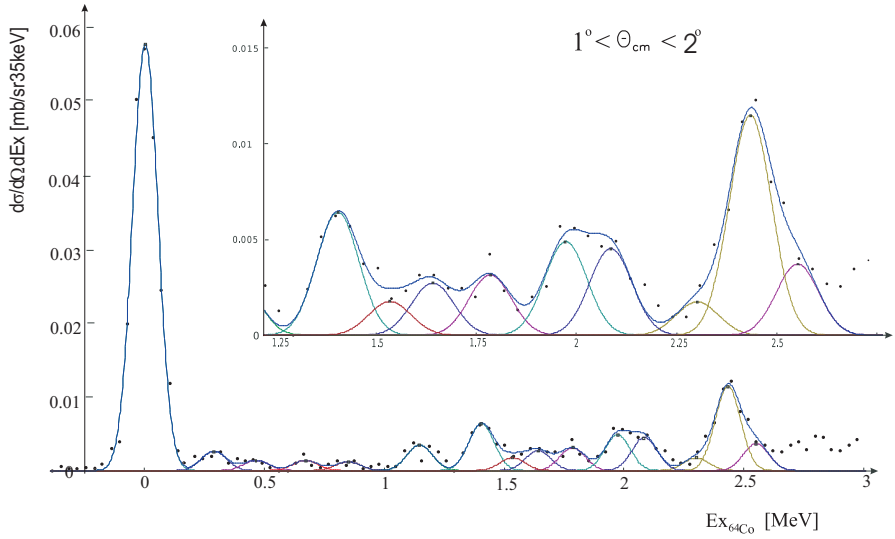

Figure 5.7 Fit of the ^{64}Co $\Theta_{cm} = 1.5°$ spectrum. The region between 1.2 and 2.7 MeV was enlarged and given as an insert in this figure.

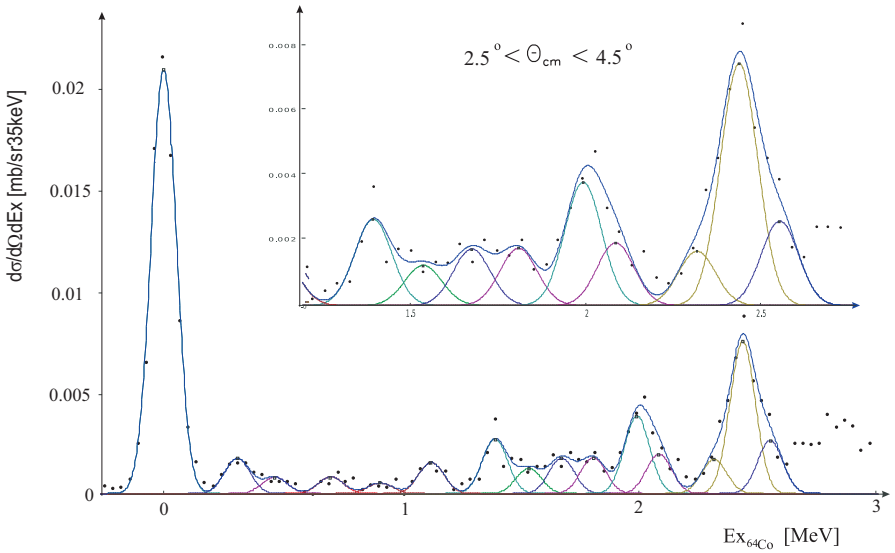

Figure 5.8 Fit of the ^{64}Co $\Theta_{cm} = 3.5°$ spectrum. The region between 1.2 and 2.7 MeV was enlarged and given as an insert in this figure.

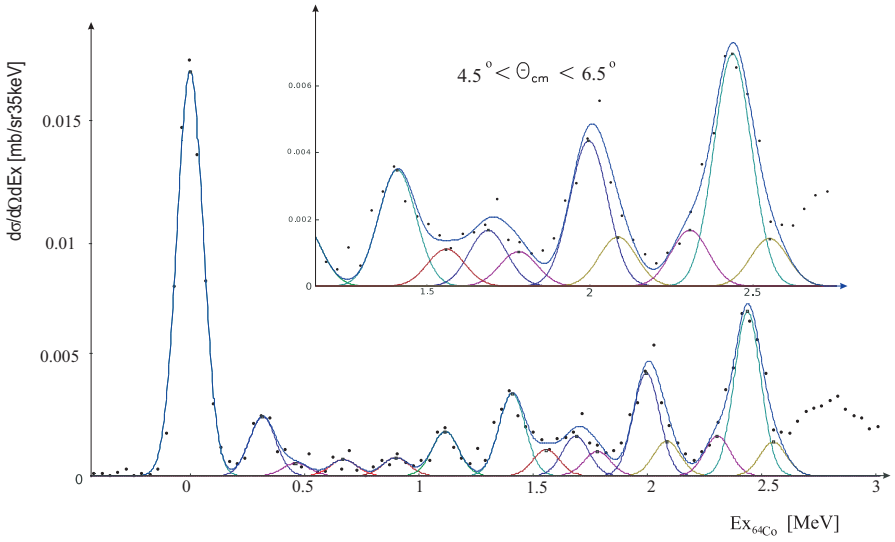

Figure 5.9 Fit of the ^{64}Co $\Theta_{cm} = 5.5°$ spectrum. The region between 1.2 and 2.7 MeV was enlarged and given as an insert in this figure.

results were the same within the error bars.

5.5 Angular distributions

Because no information is available in the literature concerning the spin and parities for levels in ^{64}Co except for the g.s. ($J^\pi = 1^+$) and the 0.311 MeV level (suggested to be $J^\pi = 1^+$), a multipole assignment will be done by analyzing the angular distributions of the cross sections of the peaks. As the reaction is spin-flip selective and because different ΔL components show different angular distributions, the $J^\pi = 1^+$ ($\Delta L = 0$) component can be distinguished.

Figure 5.10 shows the experimental data for 4 discrete transitions and 3 excitation energy intervals (1.50 - 1.86 MeV, 1.86 - 2.19 MeV and 2.19 - 2.65 MeV) together with the DWBA results obtained with the code `ACCBA` of H. Okamura [Oka99]. The cross sections for different ΔL components were obtained in the DWBA calculations as follows: the $\Delta L = 0$ component corresponds to the $J^\pi = 1^+$, the $\Delta L = 1$ to the $J^\pi = 1^-$ and the $\Delta L = 2$ to the $J^\pi = 3^+$ final state calculated cross sections. They were scaled to match the experimental cross section.

The input of the DWBA calculations is given below.

- for the effective two-body interaction the central and the tensor part from the T matrix parameterization at 100 MeV from Franey and Love [Fra85] were applied

- the optical potential parameters to create the distorted waves in the exit channel were calculated from a global fit to proton elastic scattering data for incident energies of 80-180 MeV [Nad81] (see table 5.1)

- for the incident channel, assuming a small variation with the mass number, the optical model parameters determined in a deuteron scattering experiment of ^{58}Ni [Bäu01] were used (see table 5.1)

- the spectroscopic amplitudes were calculated in the normal mode formalism by using the code `NORMOD` [vdW]. The *sd*-shell was assumed to be completely filled with 20 protons and 20 neutrons. The remaining 8 protons and 16 neutrons were distributed in the *fp*-shell as indicated in fig. 2.11. In this configuration, there is only one possibility for a 1p-1h state to be excited by a GT$^+$ transition: the ν1f5/2 state in ^{64}Co (see fig 2.11 *b*)).

- the occupation numbers and the binding energies for the shell model states used in the `NORMOD` and DWBA calculations are presented in table 5.2. The obtained wave functions are listed in appendix A.

Table 5.1 Optical model parameters used in the DWBA calculations. The deuteron parameters are assumed to be the same as for ^{58}Ni and taken from [Bäu01]; the proton parameters were calculated by using the global fit from [Nad81].

	V [MeV]	r_V [fm]	a_V [fm]	W_V [MeV]	W_D [MeV]	r_I [fm]	a_I [fm]	r_C [fm]
d+^{64}Ni	46.60	1.24	0.815	16.40	1.36	1.33	0.75	1.3
p+^{64}Ni	31.295	1.217	0.710	7.657	0.0	1.436	0.523	1.3

	V_{LS} [MeV]	r_{LS} [fm]	a_{LS} [fm]
d+^{64}Ni	1.60	1.01	0.79

Table 5.2 Ground-state v^2 and u^2 values (as the fullness of the proton shells and the emptyness of the neutron shells) and binding energies E_b of single-particle levels for the fp-shell in ^{64}Ni.

	protons		neutrons	
shell	v^2	E_b [Mai92]	u^2	E_b [Boh98]
$0g_{9/2}$			1.000	5.77 MeV
$1p_{1/2}$	0.0275	5.58 MeV	0.860	6.77 MeV
$0f_{5/2}$	0.0600	6.27 MeV	0.330	6.02 MeV
$1p_{3/2}$	0.08125	7.90 MeV	0.0	8.53 MeV
$0f_{7/2}$	0.9075	13.33 MeV	0.0	14.03 MeV

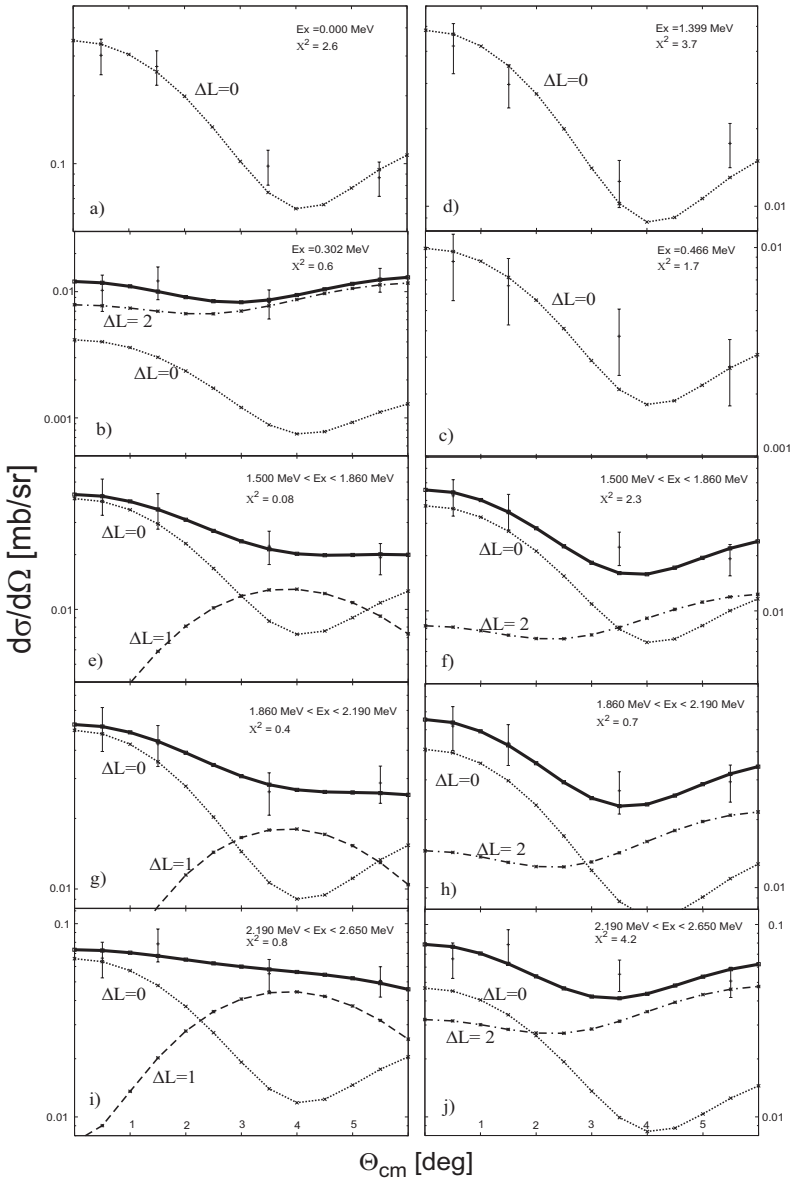

Figure 5.10 Fit of the experimental angular distributions of the differential cross section for the selected peaks and excitation energy regions. The ΔL=0, ΔL=1 and ΔL=2 shapes, corresponding to J^π values of, respectively, 1^+, 1^- and 3^+ states are obtained in a DWBA calculation (see text). The errors on the experimental points are also indicated. These error bars account for uncertainties in calculating the absolute cross section ($\approx$ 15%), statistical errors (varying from 2.3% for the g.s. peak up to 20% for the 0.466 MeV peak) and errors in the fitting procedure.

5.6 Gamow-Teller Strength

As discussed in section 2.2.1, at low momentum transfer the cross section of the ΔL =0 transitions to the $J^\pi = 1^+$ states can be connected to the GT strength, $B(GT^+)$. In the present analysis, for the calibration of the $B(GT^+)$, the ^{64}Ni(g.s.)$\longrightarrow$ ^{64}Co(g.s.) transition, for which the $\log ft = 4.3$ was measured in β-decay [Fir96], was used.

The ft-value is related to the GT strength [Tad87] by:

$$B(GT^-) = \frac{6166 \pm 2s}{(\frac{g_A}{g_V})^2 ft} = 0.209 \pm 0.012 \tag{5.3}$$

where $(\frac{g_A}{g_V})$ = 1.260±0.008 is obtained from the beta decay of the free neutron [Wil82] for which $B(GT)$=3. The value of $B(GT^+)$ of the inverse transition, appearing in the ^{64}Ni(d,^{2}He)^{64}Co reaction, is related to $B(GT^-)$ by eq. 2.12:

$$B(GT^+) = \frac{2J_f + 1}{2J_i + 1} B(GT^-) = 0.627 \pm 0.036 \tag{5.4}$$

where J_i and J_f are the spins of the initial and final states in the ^{64}Ni(d,^{2}He)^{64}Co reaction.

By applying eq. 2.9 for the g.s. transition, the unit cross section is obtained:

$$\widehat{\sigma}_{GT} = \frac{\sigma(q,\omega)}{F(q,\omega)B(GT^+)} = 0.75 \pm 0.06 \tag{5.5}$$

The function $F(q,\omega)$ is used for extrapolating the measured cross section to low momentum transfer q and energy loss ω ($= E_x - Q_{gs}$). It was determined as the ratio of two calculated cross sections:

$$F(q,\omega) = \frac{\sigma^{\Theta_{cm}=0.5^\circ}(q,\omega)}{\sigma^{\Theta_{cm}=0.0^\circ}(q=0,\omega=0)} \tag{5.6}$$

The calculations have been done by using the code `ACCBA` [Oka99] (see section 5.5). The result is a smooth curve as function of the energy loss; it is presented in fig. 5.11.

By using the results of the angular distribution analysis, the determined extrapolation function $F(q,\omega)$ and the unit cross section from eq. 5.5, the GT strengths for ΔL=0 transitions in ^{64}Co have been calculated. The results are summarized in table 5.3. The experimental GT strength distribution in the low excitation energy region of ^{64}Co is plotted in figure 5.13 (see next section).

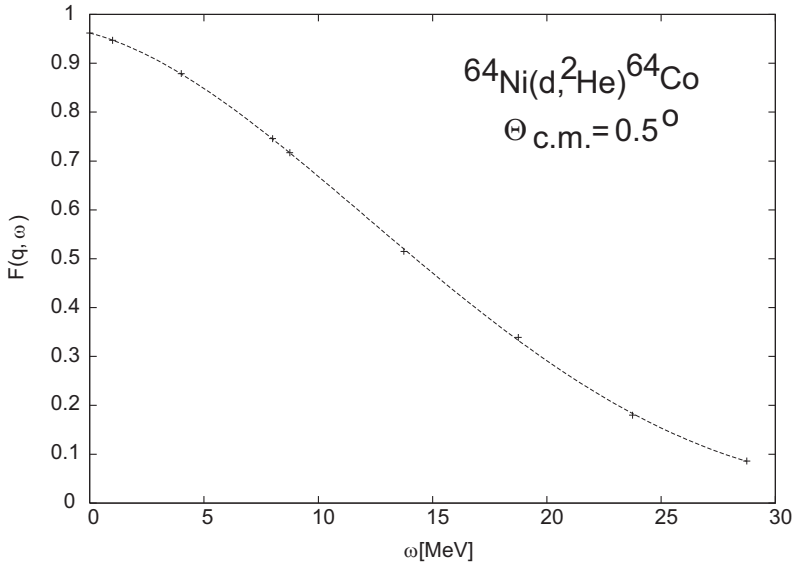

Figure 5.11 The DWBA calculations for the momentum-transfer and energy-loss dependence $F(q,\omega)$ of the ^{64}Ni$(d,^2$ He$)^{64}$Co reaction cross section as function of the energy-loss ω. The points represent the ratio of two calculated cross sections: $\sigma^{\Theta_{cm}=0.5^\circ}(q,\omega)$ / $\sigma^{\Theta_{cm}=0.0^\circ}(q=0,\omega=0)$

Table 5.3 Gamow-Teller strength of transitions to $J^\pi = 1^+$ states in ^{64}Co observed in the ^{64}Ni(d,^{2}He)^{64}Co reaction. The ratio $\sigma^{\Delta L=0}(0.5^\circ)/\sigma^{tot}$ denotes the $\Delta L = 0$ fraction of the total cross section at $\theta_{scatt} = 0.5^\circ$.

$E_x^{literature}$ (MeV)	$E_x^{(d,^2He)}$ (MeV)	$\sigma^{\Delta L=0}_{(d,^2He)}(0.5^\circ)$ (mb/sr)	$\sigma^{\Delta L=0}_{(0.5^\circ)}/\sigma^{tot}$	B(GT$^+$)
0.000	0.000	0.339±0.030	1.00	0.627±0.075
0.311(15)	0.302(15)	0.004±0.004	0.33	0.007±0.007
0.463(15)	0.466(15)	0.010±0.002	1.00	0.018±0.005
0.703(15)	0.684(20)	0.006±0.002	0.75	0.012±0.004
0.867(15)	0.878(32)	0.005±0.002	0.71	0.009±0.003
1.144(15)	1.138(25)	0.008±0.004	0.67	0.015±0.008
1.423(15)	1.399(15)	0.047±0.005	1.00	0.093±0.019
1.541(15)	1.541(24)	[a]0.039±0.008	[a]0.93	[a]0.080±0.017
1.687(15)	1.660(27)	[b]0.036±0.009	[b]0.82	[b]0.074±0.020
1.806(30)	1.787(21)			
	1.979(23)	[a]0.048±0.009	[a]0.92	[a]0.100±0.021
2.051(15)	2.077(30)	[b]0.039±0.011	[b]0.74	[b]0.082±0.025
	2.307(20)	[a]0.064±0.013	[a]0.88	[a]0.135±0.030
	2.433(15)	[b]0.045±0.016	[b]0.58	[b]0.096±0.035
	2.544(25)			

[a] Accepting the fit from fig. 5.10 *e), g) and i)*

[b] Accepting the fit from fig. 5.10 *f), h) and j)*

5.7 Discussion

The ^{64}Ni(d,^{2}He)^{64}Co study presented in this thesis reveals not only information concerning the GT$^+$ strength of transitions starting from ^{64}Ni g.s., but also spectroscopic information.

It was already mentioned that the level scheme of ^{64}Co is not well known. There are only indications of a small number of levels, mostly from a ^{64}Ni(t,^{3}He)^{64}Co study [Fly72]. In our experimental spectrum the excitation energy region below 2.6 MeV was fitted, most of the levels observed in the ^{64}Ni(t,^{3}He)^{64}Co study of E.R. Flynn and J.D. Garrett [Fly72] were also found in the present ^{64}Co spectrum. Our results are presented in table 5.3.

Above E$_x$ = 2.6 MeV the density of levels is too high and our energy resolution is insufficient to separate individual levels. Around the particle threshold energy (S_n = 6.02 MeV) background contributions generated by the quasi-free scattering have to be taken into account. The giant resonances (the GTGR, the SGDR and the SIVGMR) overlapping in this continuum give rise to the huge bump that dominates the ^{64}Co spectrum. However, looking at the spectra gated on different scattering angles (fig. 5.5) a peak corresponding to a level around 3.14 MeV as well as a peak corresponding to a level around 4.9 MeV can easily be observed coming up on top of the huge bump. They are indicated by the arrows in fig. 5.5 *d*). The evolution of these two levels in the spectra at different scattering angles suggest a $\Delta L > 0$ character.

As it was expected, the peak corresponding to the transition to the ^{64}Co gs (a $J^\pi = 1^+$ state) shows the shape of a $\Delta L = 0$ angular distribution. This is the strongest GT transition to an individual level in ^{64}Co that appears in our spectrum.

It was suggested by Runte et al. [Run85] in a study of the β-decay of ^{64}Fe to ^{64}Co, that a second 1^+ level is present at about 311 keV in ^{64}Co. This level could correspond to a level observed at 296±15 keV in the ^{64}Ni(t,^{3}He)^{64}Co experiment by E. Flynn and J. Garrett [Fly72]. Surprisingly, there is no indication of a level in that excitation energy region in the γ -decay study of a T$_{1/2}$ = 6.4 ± 3 ns isomer in ^{64}Co of M. Asai et al. [Asa00]. With the energy resolution achieved in the (d,^{2}He) experiment presented here, the gs peak could be separated from this peak, indeed present in the ^{64}Co spectrum at E$_x$=302±1 keV. But the angular distribution analysis suggests a $\Delta L = 2$ character rather than $\Delta L = 0$ for the corresponding transition. Even if this transition would have also a $\Delta L = 0$ component, as assumed in the fit from fig. 5.10 *b*), the fraction of the GT strength exhausted by this weak transition would be extremely small and as a consequence the proportionality between the cross section and the $B(GT^+)$ would be questionable [Fuj99a].

The proton spectra in the ^{64}Ni$(n,p)^{64}$Co study at E_n=198 MeV of Williams et al. [Wil95] were obtained with the MRS (Medium Resolution Spectrometer) at TRIUMF. The energy resolution of the spectra was about 800 keV, therefore the g.s. peak was contaminated with the contribution of the level at 311 keV. By comparing the position of the centroid of the peak around E$_x$=0 MeV with the one of the ^{12}C g.s. peak and ^{1}H peak, present in the (n,p) spectrum, one estimates that the contribution of the 311 keV level was about 40%±16% of the g.s. peak. This assumption is in contradiction with our results. Therefore the unit cross section and, implicitly, the GT strengths determined in the (n,p) study might need to be reconsidered. This could explain also the unusual discrepancy between the experimental $\sum B(GT^+)$ and the Large Scale Shell Model (LSSM) theoretical calculations of E. Caurier et al. [Cau99a]. The theoretical results, corrected for quenching with a factor of 0.74, underestimate the experimental $\sum_{Ex\leq 8.5\ MeV} B(GT^+)$ by about 20%.

Fig. 5.12 presents a comparison of the spectroscopic information obtained in the present study with the information available in literature at the moment. The left column represents different levels obtained in the present (d,^{2}He) analysis. The central column indicates levels obtained in the (t,^{3}He) study [Fly72] and those from the right side column levels deduced in the γ-decay study [Asa00]. The width of the lines indicates the uncertainty on the determined excitation energies. A good agreement is observed between the (d,^{2}He) and the (t,^{3}He) results. This agreement was expected, as both reactions are of (n,p) type and therefore very probably the same levels in ^{64}Co will be excited. The energy resolution achieved in the (t,^{3}He) study was 50 keV (FWHM). The low incident energy of about 23 MeV makes the reaction mechanism to play an important role, therefore the intensity of the peaks could not be compared with those from (d,^{2}He). The level spacing between the 867, 804, 703, 463 and 0 keV states determined through the (t,^{3}He) reaction are similar to the 64-97-232-441 keV cascade γ-ray energies measured in the study of Asai et al. By normalizing the 830 keV isomeric state from the γ study to the 867 keV level from (t,^{3}He), all the levels except the g.s. agree in energy within the experimental uncertainties. The energy difference between the lowest-lying state of the γ-decay measurement and the g.s. measured in the (t,^{3}He) and (d,^{2}He) reactions is +33 keV and could be explained by the existence of an additional state at 33 keV above the g.s. This hypothesis is supported by the following aspects: the experimental setup used in the γ-decay measurement could not detect 33 keV γ-rays [Asa00] and, on the other hand, the energy resolution achieved in the (t,^{3}He) and (d,^{2}He) reactions (50 keV and 110 keV) are not sufficient to separate a level at 33 keV from the g.s.

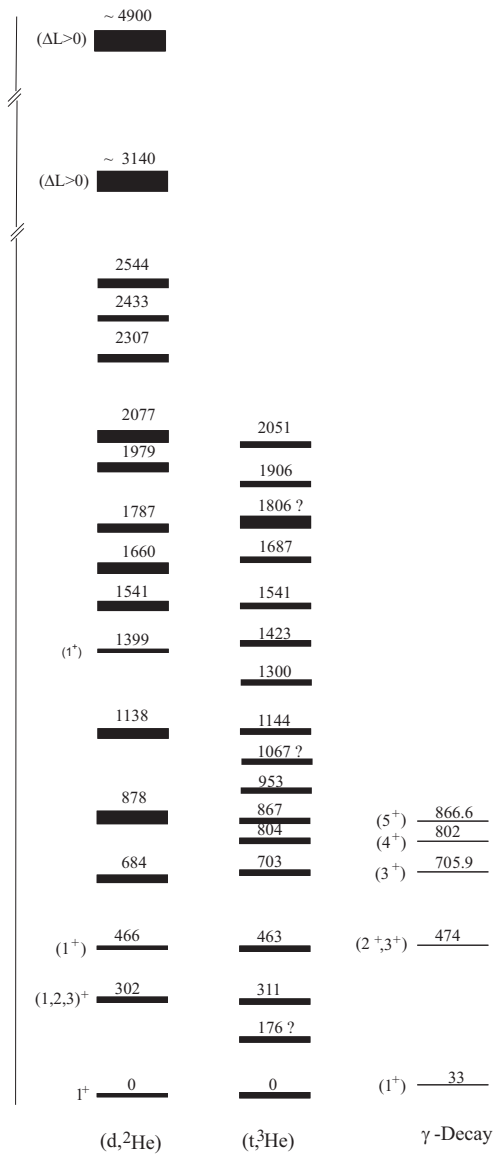

Figure 5.12 Comparison of the ^{64}Co level scheme obtained in the ^{64}Ni(d,^{2}He) experiment with the ^{64}Ni(t,^{3}He) results from ref. [Fly72] and the results of the γ-decay study of Asai et al. [Asa00] shifted by 33 keV (see text). The lines represent different observed levels and the indicated energies are in keV. The width of the lines indicates the error on the determined excitation energies. The suggested J^π values are indicated on the left side of each level.

The angular distributions presented in fig. 5.10 give indications concerning the nature of levels in ^{64}Co. The experimental angular distribution of the g.s. peak was well fitted by the calculated $\Delta L = 0$ shape. A similar character is shown by the angular distribution of a rather well separated peak at 1.399±0.015 MeV as well as of a peak corresponding to a weak transition at 0.466±0.015 MeV. Therefore we suggest a spin and parity of $J^\pi = 1^+$ for these levels.

The suggested 1^+ character of the 466±15 keV state observed in the present experiment contradicts the $(2^+, 3^+)$ assignment of the corresponding state in the γ measurement of Asai et al. [Asa00]. This aspect favors the above explanation, as the spin and parity deduced in the γ-decay study is done by starting from the assumption that the lowest-lying state of the γ measurement is the ^{64}Co g.s., known from β-decay studies to be a 1^+ state [Fir96].

Furtheron, the fig. 5.10 presents also the angular distributions for three excitation energy intervals: 1.50 MeV $\leq$ E$_x$ $\leq$ 1.86 MeV, 1.86 MeV $\leq$ E$_x$ $\leq$ 2.19 MeV and 2.19 MeV $\leq$ E$_x$ $\leq$ 2.65 MeV. The fit of the spectra for these energy regions is presented in detail on figs. 5.6 - 5.9. There are several peaks overlapping and especially the cross section deduced from the small peaks is strongly dependent on the fitting procedure. Therefore the error on these cross sections is very large and it was preferred to determine the angular distributions for the three energy regions rather than for individual peaks. The multipole character of these bunches of levels is clearly shown in fig. 5.10 $e) - j)$. The experimental distributions could be fitted by assuming a mixture of $\Delta L = 0$ and $\Delta L = 1$ contributions (fig. 5.10 $e)$ $g)$ $i)$) but they could as well be fitted by a mixture of $\Delta L = 0$ and $\Delta L = 2$ contributions (fig. 5.10 $f)$ $h)$ $j)$) . Although the χ^2 values favor the assumption of $\Delta L = 1$ contributions, it would be not surprising to have the presence of a strong $\Delta L = 2$ component due to the tensorial forces. This could indicate also that the tensor part of the interaction used in the DWBA calculations for $\Delta L = 0$ is somehow underestimated.

The B(GT$^+$) values corresponding to the $\Delta L = 0$ cross sections deduced in the angular distribution analysis have been calculated. As discussed in section 5.6, the g.s. transition, for which a ft value was measured in β-decay studies [Fir96], was used for calibration. The calculated B(GT$^+$)'s are given in table 5.3.

Fig. 5.13 compares the present results with the theoretical LSSM calculations of Caurier et al. employing a slightly monopole-corrected version of the KB3 interaction [Cau99a]. The correction for quenching was included. In both distributions, experimental and theoretical, most of the strength is con-

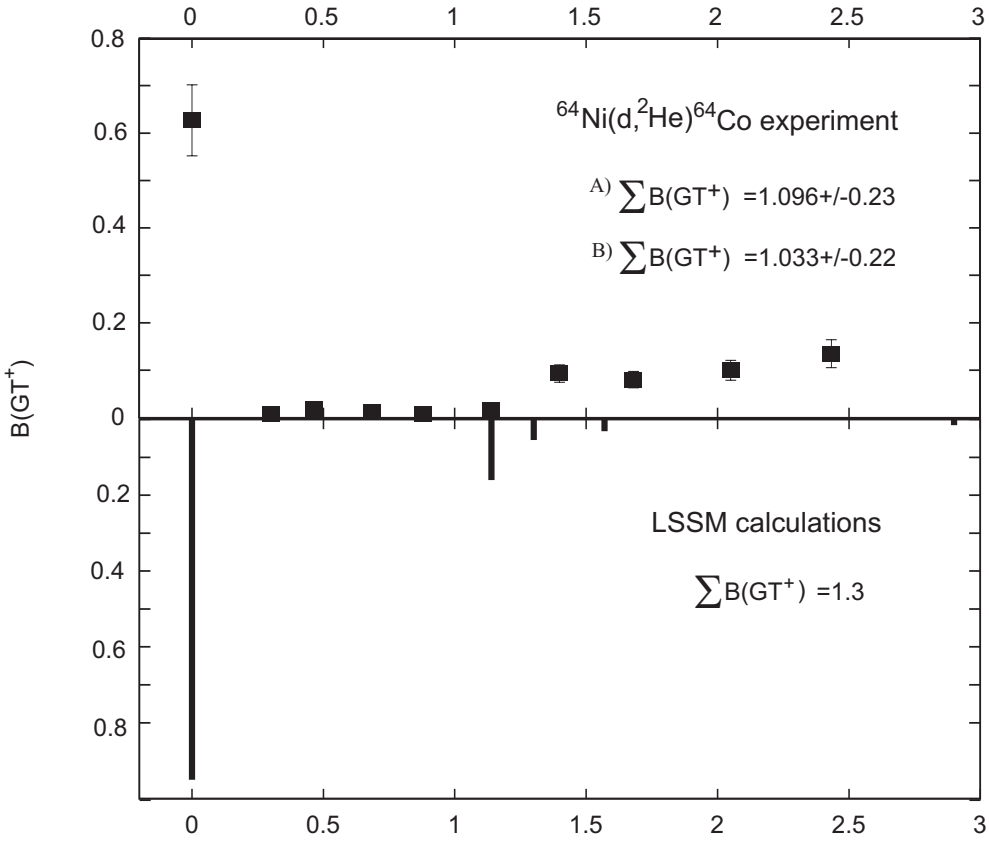

Figure 5.13 The experimental $B(GT^+)$ distribution for $E_x \leq 3$ MeV together with the LSSM calculations of the GT^+ strength from ^{64}Ni to individual levels [Cau99a]. The sum of calculated and experimental strengths (A) using the $B(GT^+)$ values from tab. 5.3 a) and (B) using the $B(GT^+)$ values from tab. 5.3 b) are indicated. A quenching factor q = 0.74 was taken into account.

centrated in the gs transition, but the shell model calculations overestimate the strength of this transition. The difference in strength is found fragmented over several states in the experimental data. The two distributions agree also in terms of integrated strength. The calculated integrated strength is 1.3 $B(GT)$ units - not far from the 1.033±0.22 (1.096±0.23) value obtained experimentally when taking into account the mixture of ΔL=0+2 (ΔL=0+1) components in the cross section (see tab. 5.3). By looking at the angular distribution of the broad bump-like structure present in the (d,^{2}He) ^{64}Co spectrum at about 12 MeV, there is no doubt that it contains a ΔL=0 component, this indicating that part of GT strength is located here. But for a proper estimation of this component, an estimation of the multi-step processes contribution is needed. This requires a rigorous theoretical description of the scattering process which is not available for the moment. The estimation of the contribution of the ΔL=0 component characterizing the SIVGMR ($2\hbar\omega$-excitations) is also required.

Chapter 6

$(^3\mathrm{He}, t)$ analysis procedure, results and discussion

Compared to the $(d,^2\mathrm{He})$ case, the analysis procedure simplifies for the $(^3\mathrm{He}, t)$ reaction, as the triton is a bound system and so no coincidence measurement is required in this case. The energy loss information from the scintillators is used for the determination of the identity of the detected particles. A gate on the region corresponding to tritium particles has to be set in the off-line analysis. The resulting spectra are free of experimental background.

6.1 Software corrections

In order to obtain the best energy resolution for the $(^3\mathrm{He}, t)$ spectra, corrections have to be made for the kinematic and optical aberrations (see Chapter 4). The correction functions are implemented in the analysis software and their parameters are determined by using the distributions of the horizontal projection θ_{fp} and the vertical projection ϕ_{fp} of the scattering angle Θ_{scatt} measured in the focal plane versus the position in the focal plane: θ_{fp}/x_{fp} and ϕ_{fp}/x_{fp}. Fig. 6.1 *a*) and *b*) show the two dimensional histograms θ_{fp} and ϕ_{fp} versus x_{fp}. These histograms are plotted before and after performing the software corrections. In the first case, fig. 6.1 *a*), a fourth order polynomial function is needed for this correction. A second order polynomial function was sufficient for correcting the aberrations on the ϕ_{fp} angle, fig. 6.1 *b*), which is directly connected with the vertical position in the focal plane (see section 4.2). The plots were done for the very low excitation energy region in ^{64}Cu, which corresponds to the high momentum side of the focal plane. The lines correspond to levels in ^{64}Cu. The straight lines from the right side of the

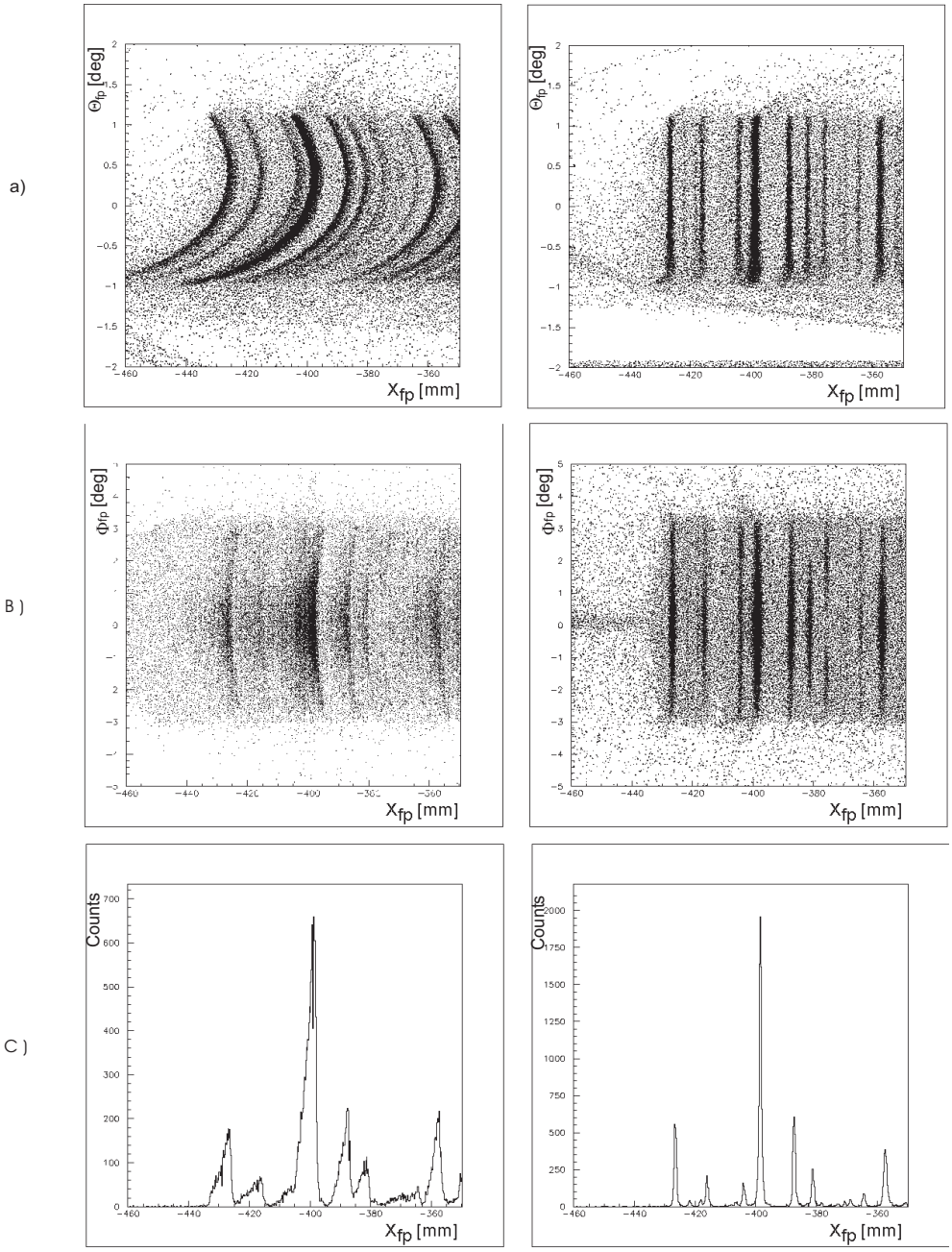

Figure 6.1 *a*) and *b*): The plot of the horizontal scattering angle θ_{fp} and of the vertical scattering angle ϕ_{fp} versus the horizontal position in the focal plane before and after applying the corrections (see text for details). *c*) The ^{64}Co spectrum for scattering angles below 0.3° before and after performing the corrections.

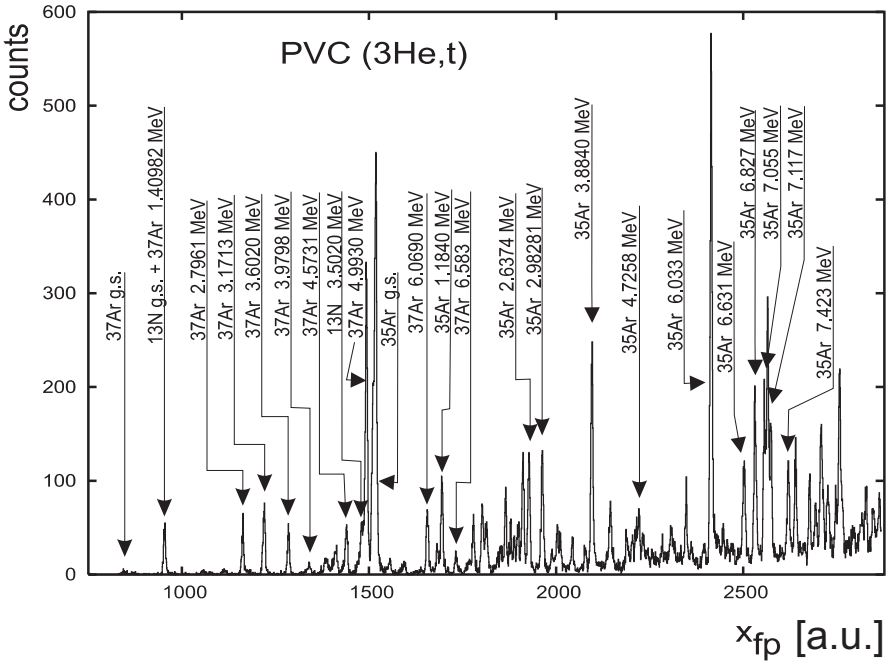

Figure 6.2 The PVC(^{3}**He**, t) calibration spectrum for scattering angles between 0° and 0.5°

figure prove that the correction is done properly.

The improvement in the energy resolution is considerable. This is illustrated in fig. 6.1 *c*), where the ^{64}Cu spectrum gated on a narrow scattering angle around 0° is plotted before and after performing the corrections. Of course, the improvement is much larger for higher scattering angle spectra.

The best energy resolution, FWHM = 32 keV, was obtained for the low energy region of the spectrum gated on $0° \leq \Theta_{scatt} \leq 0.3°$. Starting from around 7.2 MeV ($= S_p$) the density of peaks increases. There are no intense transitions in this region, therefore the corrections could not be done with the same accuracy anymore. This directly affects the energy resolution.

6.2 Energy calibration

Calibration measurements using different calibration targets were done during this experiment. For calibrating the ^{64}Cu spectrum, a (^{3}He, t) measurement on a *Polyvinyl Chloride* (PVC) target was used. The reason for choosing this

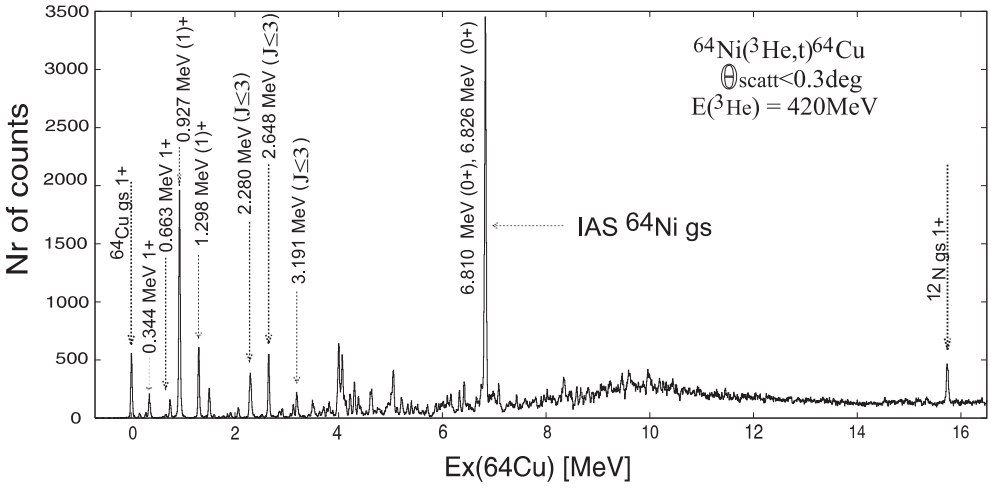

Figure 6.3 The energy calibrated ^{64}Cu spectrum for scattering angles between 0° and 0.3°. Some $L = 0$ states are indicated by their excitation energies. The most intense peak was identified to be the isobaric analog of the ^{64}Ni ground state with $J^\pi = 0^+$. The peak appearing at 15.7 MeV corresponds to the ^{12}N g.s. originating from a ^{12}C contamination of the target.

calibration target was that it contains many components with known levels well distributed over the full focal plane. Peaks due to the scattering on excited levels in ^{37}Cl, ^{35}Cl, ^{13}C and ^{12}C were identified in the PVC(^{3}He, t) spectrum, shown in fig. 6.2. Moreover, the ^{37}Cl(^{3}He, t)^{37}Ar Q-value (= -0.832 MeV) is close to the one of ^{64}Ni(^{3}He, t)^{64}Cu (= -1.693 MeV). Therefore the position of the ^{64}Cu g.s. peak in the focal plane is well calibrated by the low excitation energy levels in ^{37}Ar.

Figure 6.2 shows part of the calibration (^{3}He, t) spectrum for which a gate $\Theta_{scatt} \leq 0.5°$ was imposed. Several levels could be identified and they are indicated in the figure by their nature and excitation energies. The dependence of the position in the focal plane, x_{fp}, on the outgoing particle energy, E_t, can be deduced from here. As this dependence is not linear, it is imperative to calculate the $B\rho$ ($=\frac{p}{q} \sim \sqrt{E_t}$) value for each identified peak and to determine the $B\rho$ dependence on the x_{fp}. This is done via kinematic calculations, by taking into account the reaction on the target to which the respective peak corresponds. The same kinematic calculations have to be done for the ^{64}Ni(^{3}He, t)^{64}Cu reaction and the $B\rho$ values related to the excitation energy of levels in ^{64}Cu, $E_x(^{64}Cu)$. Further, by combining the two determined de-

pendences and by calibrating on the position of the g.s. peak in ^{64}Cu, the positions in the focal plane can be converted in excitation energies in ^{64}Cu.

The obtained ^{64}Cu excitation energy spectrum is given in fig. 6.3. The estimated uncertainty induced by the energy calibration is about 4 keV. The calibration was checked by several levels known in the literature that were identified at the expected excitation energies in our spectrum.

6.3 Fit of the spectra

As the measurements were done with only one angular setting $\theta_{GR} = 0°$, for obtaining an angular distribution of peaks in ^{64}Cu, the data were divided into four sets corresponding to four different scattering angle gates:

- $0.0° \leq \Theta_{scatt} \leq 0.3°$
- $0.5° \leq \Theta_{scatt} \leq 1.0°$
- $1.0° \leq \Theta_{scatt} \leq 1.5°$
- $1.5° \leq \Theta_{scatt} \leq 2.0°$

The four resulting spectra were fitted by using `hfPfit2` program developed by H.Fujita in 1999 based on the 1988 revised version, by Y. Fujita, of the `Pfit` program [Mor]. The spectra are decomposed, by using a given response function, into individual peaks.

Four different response functions have been determined, one for each of the four spectra. Figure 6.4 shows the response function used to fit the spectrum gated by $\Theta_{scatt} < 0.3°$. The experimental points for the g.s. peak are included in the figure for comparison. This function was obtained by combining the shape of the g.s. peak, of the 0.927 MeV peak and of the 1.298 MeV peak. All these three peaks are quite well separated, the contributions from the neighboring excited levels being rather small. The response functions used for fitting higher angle spectra were determined in the same way. The estimated uncertainty on the peak position induced by the definition of the response function is below 3 keV.

No background contributions were assumed for the low excitation energy region. Starting from about the proton separation energy (S_p = 7.2 MeV), background contributions from the QFS have to be taken into account (see section 3.4). Contributions from giant resonances like GDR or IVGMR, which are very broad resonances, expected respectively at about 25 MeV and at about 35 MeV in ^{64}Cu have also to be taken into account (see sections 3.3 and 3.2). The tails of these resonances could be considerable even at low excitations energies. It was discussed in sections 3.4 and 5.7 that the shape

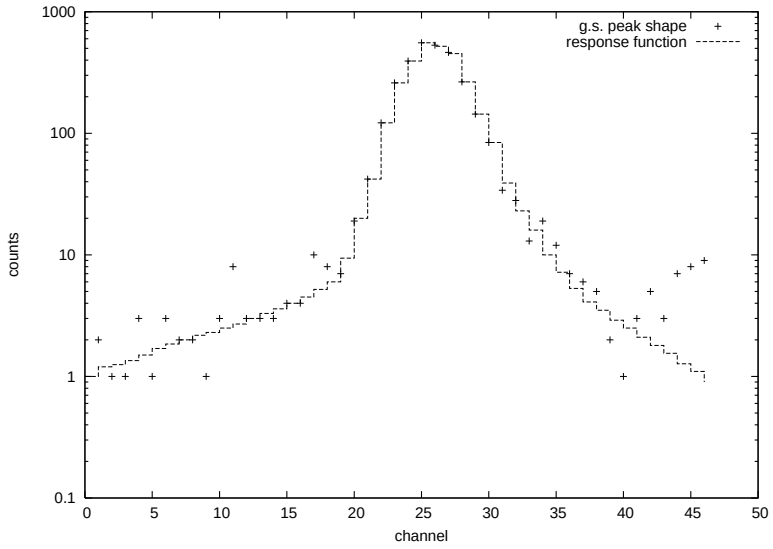

Figure 6.4 The response function used for the fit of the $\Theta_{scatt} < 0.3°$ ^{64}Cu spectrum. The points correspond to the ^{64}Cu g.s. peak. Remark the logarithmic scale for the number of counts.

and angular distribution of the QFC region from the QFS processes is not completely understood. The parametrisation of Erell et al. [Ere86], discussed in section 3.4 could be used successfully for (^{3}He, t) experiments performed with a poorer energy resolution than in our case [Jän93]. Unfortunately, this formula could not describe well the background in our ^{64}Cu spectra. Therefore we assumed for the background a line connecting the minima's in the spectrum starting at about 3.4 MeV (as will be shown in fig. 6.19). This "background" accounts both for QFS and for higher order giant resonances, allowing the extraction of the GT strength in the excitation energy region below the IAS of ^{64}Ni g.s. and in the region around 10 MeV, where the GTGR is expected (see section 3.1).

The low energy region of the $\Theta_{scatt} < 0.3°$ spectrum decomposed into individual levels is shown in fig. 6.5. The position of several levels is indicated by their known excitation energy (from the compiled data). More than 100 levels were found in the excitation energy region $E_x \leq 7.2$ MeV. A good agreement with the information existent in literature was observed. These results will be discussed in section 6.6. A complete list of the obtained levels will be given in tables 6.1- 6.5.

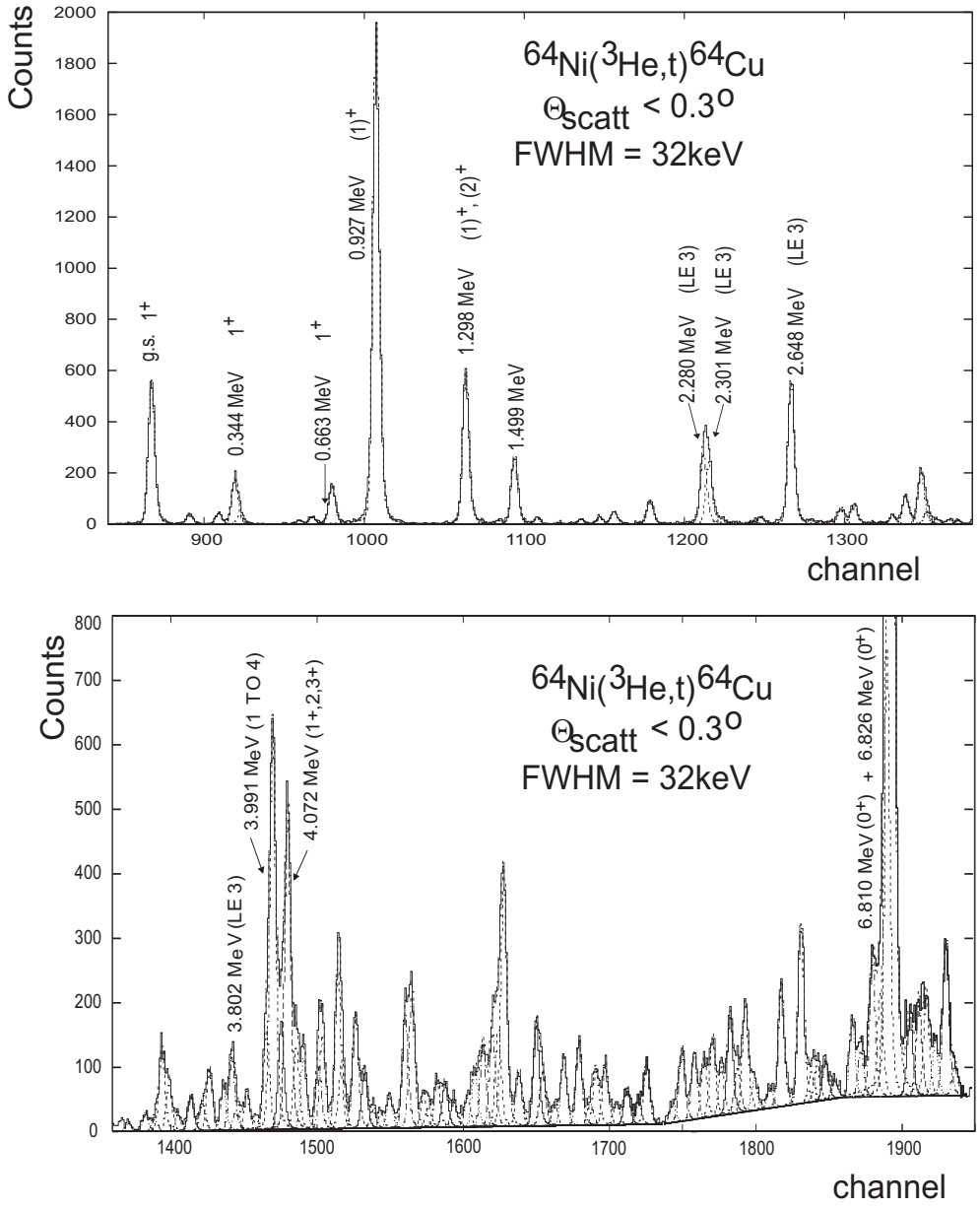

Figure 6.5 The fit of the ^{64}Cu spectrum for scattering angles between 0° and 0.34° in the low excitation energy region $E_x \leq 7.2$ MeV. The thin full line corresponds to the experimental spectrum.

6.4 Angular distributions. Identification of Gamow-Teller transitions

Similar to the case of our (d,^{2}He) study, the identification of the GT transitions in ^{64}Cu was done via an angular distribution analysis. The four spectra obtained for different scattering angle gates, as discussed in section 6.3, were used for producing the experimental angular distributions.

The theoretical shape of the cross section dependence on the scattering angle for the $J^\pi = 1^+$ ($\Delta L = 0$), $J^\pi = 1^-$ ($\Delta L = 1$) and $J^\pi = 3^+$ (ΔL =2) states was determined via DWBA calculations by using the code `DW81` of J.R. Comfort [Com].

The input of the `DW81` calculations is given below:

-for the effective two-body interaction the form derived from Schaeffer [Sch71] through the folding procedure was used. The strength used for the central part of the interaction was $V_\tau^C = 0.75$ MeV and $V_{\sigma\tau}^C$ = -2.1 MeV; for the spin-orbit part $V_\tau^{LS} = 0$ MeV was used and for the tensor part V_τ^T = -1.5 MeV.

-the $(1\nu f_{7/2}^{-1}, 1\pi f_{5/2})$, $(2\nu p_{3/2}^{-1}, 2\pi p_{3/2})$ and $(2\nu p_{3/2}^{-1}, 2\pi p_{1/2})$ configurations were considered for the $\Delta J^\pi = 1^+$ transitions, the transition amplitudes being calculated in the normal-modes formalism by using the `NORMOD` code [vdW]. This code receives as input the ocupation numbers for the 1p-1h states and the configurations pf importance for our work. It calculates the matrix elements by exhausting the complete strength that is contained in the 1p-1h basis associated with the spherical tensor operator acting on the g.s.

-the optical potential parameters for the incident channel were considered to be the same as in the case of the ^{58}Ni(^{3}He, t)^{58}Cu reaction. The parameters determined by T. Yamagata et al. [Yam95] were used.

-for the exit channel, the well depths were multiplied by a factor of 0.85 keeping the geometrical parameters the same (see ref. [Wer89] for details).

A good agreement between the calculated shape for the $\Delta L = 0$ distribution and the experimental results was observed for the g.s. peak as well as e.g. for the 0.344 MeV, 0.926 MeV, or the 1.296 MeV peaks, corresponding to known or suggested $J^\pi = 1^+$ levels at 0.344 MeV, 0.927 MeV and 1.298 MeV. Also good agreement was observed between the calculated shape for the ΔL = 2 angular distribution and e.g. the distribution for the peaks corresponding to the 0.159 MeV and 0.278 MeV levels, which are known to have $J^\pi = 2^+$.

Because the angular acceptance of the spectrometer is large in the vertical direction, the angular distribution of some strong well separated levels can be directly deduced by analyzing the two dimensional plot of the vertical angle

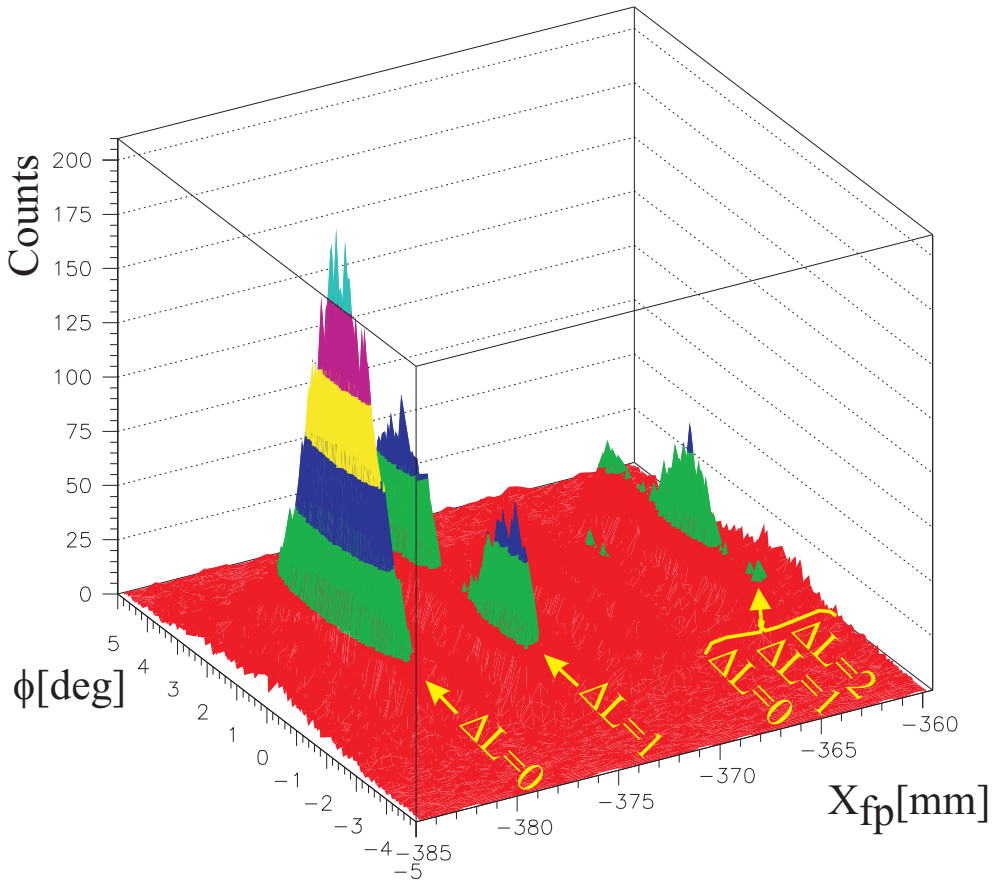

Figure 6.6 Three dimensional plot (number of counts versus vertical scattering angle and position in the focal plane) showing directly the angular distributions in ^{64}Cu.

versus the position in the focal plane (see e.g. the plot from fig. 6.1). A similar, but three dimensional plot (with the third dimension represented by the number of counts) is shown in the fig. 6.6, for a small region in the focal plane. The peaks corresponding to levels located in this region have different multi-polarities. The peak around x_{fp}=-379 mm has a characteristic $\Delta L = 0$ shape of the angular distribution, with the largest cross section at 0° and decreasing with increasing the angle. A characteristic $\Delta L = 1$ shape is shown by the distribution of a peak appearing at about x_{fp}=-375 mm. The cross section of this peak has a minimum around 0° and increases with increasing the angle. A mixture of $\Delta L = 0$ with a $\Delta L = 1$ or $\Delta L = 2$ component can be seen in the angular distribution of the doublet at about x_{fp}=-364 mm. The cross section of this doublet has a maximum at 0°, decreases with increasing the angle and increases again at about 2.5°.

The angular acceptance of the GR Spectrometer is illustrated in the two dimensional plot from fig. 6.7. Only the central part of the acceptance was used ($\theta_{fp} \leq 0.8°$ for the horizontal projection of the scattering angle and $\phi_{fp} \leq 2°$ for the vertical projection), as aberrations effects can be still present at the limit of the angular acceptance. The defined gates on the scattering angle Θ_{scatt}, which were imposed for obtaining the four spectra, are indicated by the four different colored regions.

The easiest and the most direct way to distinguish between $\Delta L = 0$ and $\Delta L \geq 1$ transitions is by looking at the evolution of the cross sections at different scattering angles for different peaks relative to the values for the g.s. peak (well known $\Delta L = 0$ transition). Therefore the ratios R1 = $\frac{\sigma(0.5° \leq \Theta_{scatt} \leq 1°)}{\sigma(\Theta_{scatt} \leq 0.3°)}$, R2 = $\frac{\sigma(1° \leq \Theta_{scatt} \leq 1.5°)}{\sigma(\Theta_{scatt} \leq 0.3°)}$ and R3 = $\frac{\sigma(1.5° \leq \Theta_{scatt} \leq 2°)}{\sigma(\Theta_{scatt} \leq 0.3°)}$ where calculated and normalized to the values for the g.s. peak. The result is given in the fig. 6.8 and will be discussed in section 6.6.

6.5 Gamow-Teller Strength

The proportionality between the (^{3}He, t) reaction cross section extrapolated to zero momentum transfer and the $B(GT^-)$ was discussed in section 2.2.2. For the ^{64}Ni(^{3}He, t)^{64}Cu reaction, the unit cross section $\widehat{\sigma}_{GT}$ can be directly measured experimentally, as the g.s of ^{64}Cu has $J^\pi = 1^+$ and decays via a GT β transition to the $J^\pi = 0^+$ g.s. of ^{64}Ni. A $\log ft$ value of 4.973 ± 0.004 was measured for the β^+ decay of ^{64}Cu (g.s.) to ^{64}Ni(g.s.) [Fir96]. This ft-value allows to deduce the GT strength [Tad87]:

$$B(GT^+) = \frac{6166 \pm 2s}{(g_A/g_V)^2 ft} = 0.0413 \pm 0.0012 \tag{6.1}$$

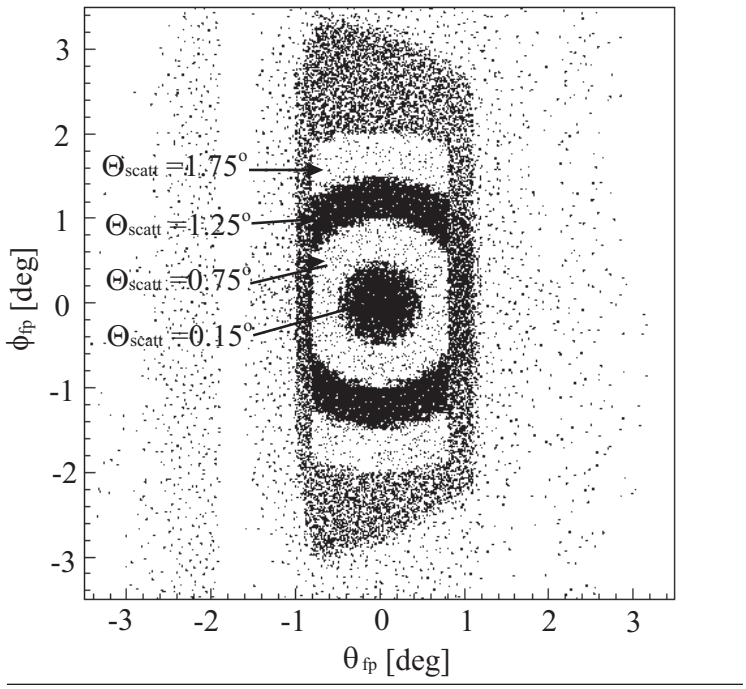

Figure 6.7 Vertical scattering angle ϕ_{fp} versus the horizontal scattering angle θ_{fp} plot showing the angular acceptance of the GR spectrometer. The areas in different colors correspond to the defined angular gates around the indicated scattering angle Θ_{scatt} values which were imposed when producing the spectra. It can be easily remarked that only the central part of the acceptance was used.

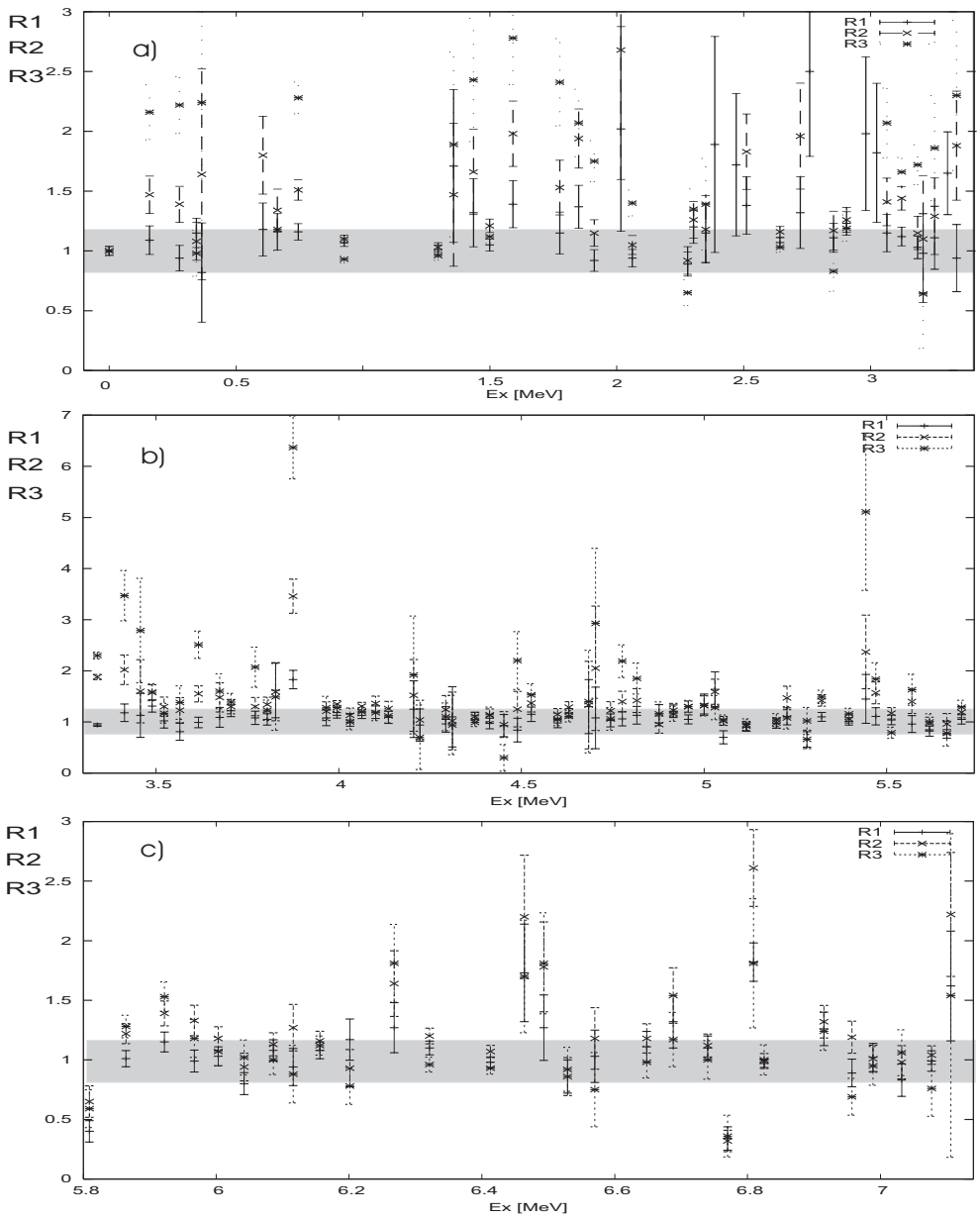

Figure 6.8 Angular distributions of levels in ^{64}Cu as ratios of relative cross sections: R1 = $\frac{\sigma(0.5^\circ \leq \Theta_{scatt} \leq 1^\circ)}{\sigma(\Theta_{scatt} \leq 0.3^\circ)}$, R2 = $\frac{\sigma(1^\circ \leq \Theta_{scatt} \leq 1.5^\circ)}{\sigma(\Theta_{scatt} \leq 0.3^\circ)}$ and R3 = $\frac{\sigma(1.5^\circ \leq \Theta_{scatt} \leq 2^\circ)}{\sigma(\Theta_{scatt} \leq 0.3^\circ)}$ normalized to the g.s. peak. The points in the shaded regions correspond to the accepted $\Delta L = 0$ transitions.

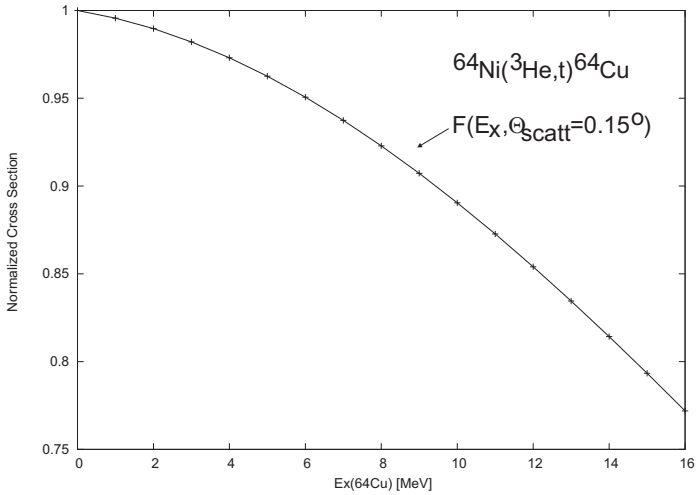

Figure 6.9 The DWBA calculated function for extrapolating the $\theta_{scatt} = 0.15°$ reaction cross section to zero momentum transfer.

The $B(GT^-)$ value of the corresponding transition observed in the $(^3\mathrm{He}, t)$ experiment is obtained by correcting for the statistical weight $2J + 1$ factors of the initial and final states:

$$B(GT^-) = \frac{2J_f + 1}{2J_i + 1} B(GT^+) = 0.124 \pm 0.0037 \tag{6.2}$$

where J_i and J_f are the spins of the initial and final states in the $(^3\mathrm{He}, t)$ reaction. By simply dividing the g.s. peak cross section extrapolated to zero momentum transfer by $B(GT^-)$, one obtains $\widehat{\sigma}_{GT}$, the unit cross section (see eq. 5.5).

The ^{64}Cu spectrum gated with $\Theta_{scatt} \leq 0.3°$ was used for determining the $B(GT^-)$ distribution. For correcting these cross sections for the extrapolation to zero momentum transfer and energy loss, the $F(q, E_x)$ function plotted in fig. 6.9 was used. This function was determined via DWBA calculations by using the `DW81` code [Com]. It represents the ratio of two calculated cross sections: one for $\Theta_{scatt} = 1.5°$ and $E_x \geq 0$ and the other one for $\Theta_{scatt} = 0°$ and $E_x = 0$. As the $\widehat{\sigma}_{GT}$ was measured experimentally, from the g.s. transition, we have directly determined the dependence of the function F on the excitation energy and normalized it to the g.s. transition. The corrections in the low energy region are small (less than 5% for $E_x \leq 5$ MeV).

The strengths of the assumed GT states below $E_x = 5$ MeV have been calculated. A plot will be given in fig. 6.17.

6.6 Discussion

The results of the (^{3}He, t) experiment presented in this thesis can be divided into three groups, according to the degree of confidence of the obtained values. First the low energy region of the spectrum, for which our results are given with good accuracy, is considered. Due to the high level density, with as a consequence the still insufficient energy resolution and due to the assumptions and estimations that have to be made for the background contributions, the results in the region starting from about 3.4 MeV to about 7.2 MeV are less precise; for this second group of results supplementary uncertainties of about 10% (even larger for the weak transitions), have to be considered. Finally, the third group deals with the high excitation energies, where only indications, both concerning the GT strength and the spectroscopic information, can be given.

⋆ **^{64}Cu excitation energy region $E_x \leq$3.4 MeV**

The excellent energy resolution of about 35 keV (32 keV for the 0° spectrum) achieved in our experiment made possible the separation of individual peaks in the excitation energy region from 0 to about 3 MeV. In the compiled data, existing at the moment [NDC], correspondent levels were found for all the levels that we obtained in this excitation energy region. The complete list is given in tables 6.1 and 6.2.

As the Fermi strength is expected to be concentrated exclusively in the transition to the IAS of the target g.s., we will assume that all the identified ΔL = 0 transitions in this low energy region are of Gamow-Teller type. The ΔL = 0 assignment is based on an angular distribution analysis as discussed. Transitions that followed an angular distribution similar to the one corresponding to the g.s. transition were selected (see fig. 6.8). It has been shown from a study of mirror GT transitions in ^{27}Al(^{3}He, t)^{27}Si and ^{27}Si$\longrightarrow{}^{27}$Al β-decay [Fuj99a] that, at this beam energy, the proportionality between the reaction cross section and the transition strength is valid if the $B(GT^-)$ values are larger than 0.04. In our study the proportionality factor was determined from the g.s. transition, for which the $B(GT^-)$ was calculated by using the logft value measured in β-decay experiments [Fir96] (see section 6.5). The determined $B(GT^-)$ values for GT transitions to the excited levels are also given in tables 6.1 and 6.2. For the weak transitions, with $B(GT^-) < 0.04$, this proportionality becomes questionable. Therefore the corresponding $B(GT^-)$ values are indicated between brackets.

Generally a good agreement with the information in literature was obtained.

Table 6.1 Levels and $B(GT^-)$ values for transitions to $J^\pi = 1^+$ states in ^{64}Cu observed in the ^{64}Ni(^{3}He, t)^{64}Cu reaction for $E_x \leq 3.4$ MeV. The indicated uncertainty of the peak position contains both statistical and systematical uncertainties. The indicated errors on the calculated $B(GT^-)$ values don't include sytematic uncertainties.

$E_x^{compilation}$ (MeV)	$E_x^{(3He,t)}$ (MeV)	$(J^\pi)^{compilation}$	$(\Delta L)^{(3He,t)}$	$B(GT^-)^{(3He,t)}$
0.000	0.000(5)	1^+	0	0.124±0.013
0.159282(3)	0.159(5)	2^+	≥1	
0.278257(8)	0.277(5)	2^+	≥1	
0.343898(9)	0.344(5)	1^+	0	0.038±0.006
0.362231(6)	0.365(6)	3^+	≥1	
0.608784(9)	0.606(5)	2^+	≥1	
0.66300(3)	0.663(5)	1^+	0	(0.006±0.002)
0.746245(11)	0.745(5)	$(3)^+$	≥1	
0.927079(10)	0.926(5)	$(1)^+$	0	0.430±0.042
1.298123(14)	1.296(5)	(1^+)	0	0.130±0.013
1.35425(3)	1.357(6)	$(3)^+$	≥1	
1.43869(3)	1.435(5)	$(1)^+$	(≥1)	
1.49918(3)	1.499(5)	$(2)^-$	0	0.060±0.007
1.59438(3)	1.591(5)	$(1^+, 2)$	≥1	
1.68312(3)	1.683(5)	≤ 3	≥1	
1.77954(4)	1.775(5)	$(1^+, 2^+)$	≥1	
1.85265(3)	1.850(5)	$(1^+, 2^+)$	≥1	
1.905093(15)/1.918(1)	1.911(5)	$(1^+, 2)$ / ≤ 4	≥1	
2.0212(5)	2.016(6)	$(1^+, 2^+, 3^+)$	≥1	
2.060(2)/2.065(2)	2.061(5)	≤ 3 / ≤ 4	≥1	
2.27975(6)	2.279(5)	≤ 3	0	0.115±0.017
2.30109(6)	2.302(5)	≤ 3	0	
2.35462(7)	2.350(6)	≤ 3	(0)	(0.005±0.001)
2.38795(15)	2.386(6)	(1^+)	≥1	
2.46547(10)	2.470(6)	$(1^-, 2^-)$	≥1	
2.50729(12)	2.511(5)	(≤ 3)	≥1	
2.64791(11)	2.643(5)	≤ 3	0	0.126±0.013
2.71797(10)	2.723(6)	$(1^-, 2^-)$	≥1	
2.76419(11)	2.760(6)	$(1^-, 2^-)$	≥1	
[a] 2.83054(7)	2.821(6)	≤ 3	≥1	

[a] seen at 2.823 MeV in ^{63}Ni(d, p) and ^{66}Zn(d, α) studies. [NDC]

Table 6.2 Continuation of table 6.1

$E_x^{compilation}$ (MeV)	$E_x^{(3He,t)}$ (MeV)	$(J^\pi)^{compilation}$	$(\Delta L)^{(3He,t)}$	$B(GT^-)^{(3He,t)}$
2.854(11)	2.854(6)	$(0^+ to\ 3^+)$	0	(0.014±0.002)
[a)]2.89684(7)	2.905(5)	(1^+)	0	(0.017±0.002)
2.985(11)	2.981(6)	$(1^-, 2^-)$	≥1	
3.03376(13)	3.024(6)	$(0^-, 1^-, 2^-)$	≥1	
3.072(2)	3.064(5)	$(2^-, 3^-, 4^-)$	≥1	
3.1255(3)	3.122(5)	(≤ 3)	≥1	
3.19107(12)	3.185(5)	(≤ 4)	≥1	
3.20759(9)	3.207(6)	$(0, 1, 2)$	≥1	
3.25761(7)	3.252(6)	$(0, 1, 2)$	≥1	
3.313(6)	3.303(6)	$(1^-, 2^-)$	≥1	
3.34392(17)	3.339(6)	(≤ 3)	≥1	

[a)] seen at 2.913 MeV in ^{63}Ni(d, p) and ^{66}Zn(d, α) studies. [NDC]

However, the peak observed at 1.499±0.005 MeV shows a clear ΔL=0 angular distribution (see fig. 6.8 and fig. 6.10). This is a rather strong and well separated peak, therefore its angular distribution was determined with good accuracy. By checking the information existent in literature [NDC], the only level that can be associated to this peak is at 1.49918±0.00003 MeV and it's indicated as having $J^\pi = (2)^-$. This contradicts our result.

The fit of the region 1.2 MeV≤ E_x ≤2.5 MeV of the spectra obtained for different scattering angles is given in fig. 6.10. The number of counts in the different spectra is not corrected for the solid angle acceptance. Therefore the following discussion is based on relative values compared to the g.s. peak and, e.g., the peak at 1.296±0.005 MeV, which correspond to transitions with $\Delta L = 0$. A peak growing in intensity with increasing the scattering angle is easily observed at about 1.683±0.005 MeV; this peak follows a $\Delta L \geq 1$ angular distribution. In contrast, the doublet at about 2.29 MeV follows a $\Delta L = 0$ angular distribution, decreasing in intensity with increasing scattering angle. The energy resolution is insufficient to separate the two levels: one at 2.279±0.005 MeV and the other at 2.302±0.005 MeV, therefore their cross sections determined in the fit might be less precise. Following the fit of the doublet at different scattering angles, it can be seen that the strength slightly moves from the first peak of the doublet to the second one when increasing the scattering angle. Therefore the cross section of the 2.279±0.005 MeV peak seems to decrease faster than that of, e.g., the g.s. peak and the cross section

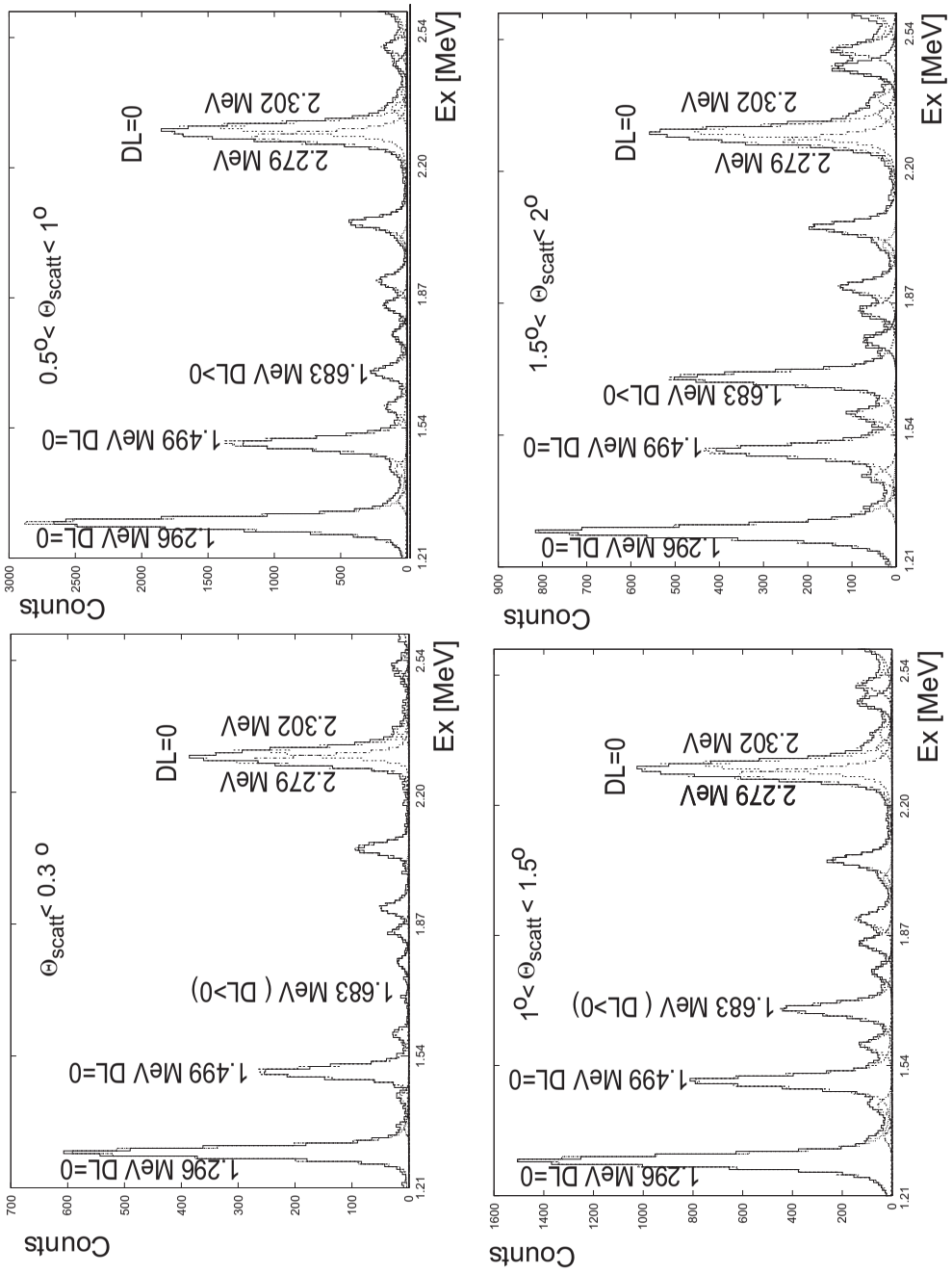

Figure 6.10 ^{64}Ni(^{3}He, t)^{64}Cu reaction: Fit of the 1.2 MeV$\leq$ E_x $\geq$2.6 MeV region in ^{64}Cu spectra.

of the 2.302±0.005 MeV peak decreases slower than that of the g.s. peak. This "anomaly" is observed in the plot from fig. 6.8. However, the $\Delta L = 0$ character of the doublet is clear, therefore the $B(GT^-)$ (= 0.115±0.017) was calculated for the doublet and not separately for the two peaks.

A similar "anomaly" is observed in the region around 2.87 MeV (see figs. 6.11 and 6.8), which is analyzed as a triplet containing contributions from peaks at 2.821 MeV, 2.854 MeV and 2.905 MeV. The information in literature [NDC] indicates a 2.83054±0.00007 MeV level , with $J^\pi \leq 3$, a 2.854±0.011 MeV level, with a suggested J^π value of 0^+, 1^+, 2^+ or 3^+, and a 2.89684±0.00007 MeV level, with a suggested J^π value of 1^+ for these peaks (see table 6.1). The first peak shows a $\Delta L \geq 1$ angular distribution and the others a $\Delta L = 0$ angular distribution. Due to the fitting procedure, it might be that part of the cross section of the peak at 2.854±0.006 MeV is wrongly included in the 2.821±0.006 MeV peak. This explains why the cross section of the 2.854±0.006 MeV peak decreases faster than the one of the g.s. peak. Anyway, the cross section of the 2.854±0.006 MeV peak is too small to rely on the proportionality with the transition strength. Therefore the calculated $B(GT^-)$ is indicated between brackets. A similar indication was used for the peak at 2.905±0.005 MeV.

The obtained GT strength distribution in this low excitation energy region is included in fig. 6.5. The obtained strength is

$$\sum_{0 \leq E_x \leq 3.4\ MeV} B(GT^-) = 1.065 \pm 0.052$$

when including also the determined $B(GT^-)$ values for the weak transitions.

⋆ ^{64}Cu excitation energy region 3.4 MeV $\leq E_x \leq$7.2 MeV

A decomposition of multiplets into individual peaks was tried for the complete excitation energy region up to the proton separation energy in ^{64}Cu (S_p = 7.2 MeV). But from about 3.4 MeV the spectra start to have background contributions. The background in the region below 7.2 MeV was fitted by a line connecting the minimum values in the spectrum. This assumption and estimation of the background induces an additional uncertainty in the determined peak positions and cross sections. From multiple fits, by using different estimations of the background, the additional induced uncertainty in the obtained peak positions was deduced to be less than 1 keV for the strong peaks. For the cross sections of the peaks the uncertainty is larger for higher scattering angle spectra than at 0°. In the spectrum for $\Theta_{scatt} \leq 0.3°$ the background is very low (e.g. it amounts to 10 counts at 5.7 MeV). Therefore the induced uncertainty in the determined $B(GT^-)$ values is rather low (less than 0.001

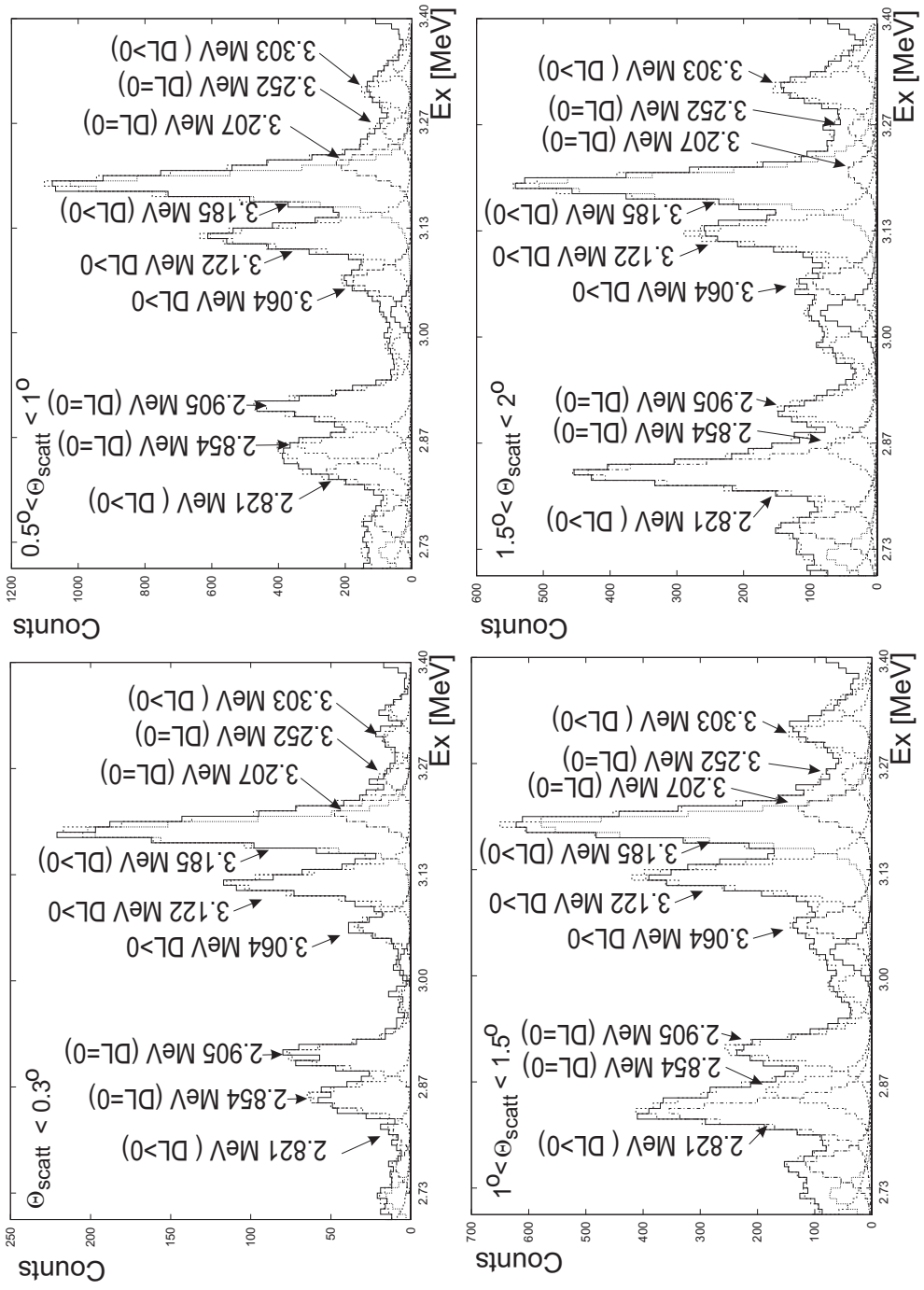

Figure 6.11 ^{64}Ni(^{3}He, t)^{64}Cu reaction: Fit of the 2.6 MeV$\leq$ E_x $\geq$3.4 MeV region in ^{64}Cu spectra.

Table 6.3 Levels and $B(GT^-)$ values for transitions to $J^\pi = 1^+$ states in ^{64}Cu observed in the ^{64}Ni(^{3}He, t)^{64}Cu reaction. The indicated uncertainty of the peak position contains both statistical and systematical uncertainties. The indicated error on the calculated $B(GT^-)$ values doesn't include systematic uncertainty.

$E_x^{compilation}$ (MeV)	$E_x^{(^3He,t)}$ (MeV)	$(J^\pi)^{compilation}$	$(\Delta L)^{(3He,t)}$	$B(GT^-)^{(^3He,t)}$
3.41219(9)	3.413(5)	(≤ 3)	$\geq$1	
3.46557(12)	3.457(6)	(≤ 3)	$\geq$1	
3.49337(20)	3.489(5)	(≤ 3)	($\geq$1)	
3.52470(11)	3.522(5)	(≤ 4)	0	(0.016$\pm$0.003)
	(3.565)			
	3.616(6)		$\geq$1	
3.686(10)	3.674(6)	-	(0)	(0.010$\pm$0.002)
3.71192(15)	3.705(5)	(≤ 3)	(0)	(0.021$\pm$0.003)
3.763(10)	3.771(6)		($\geq$1)	
3.80274(13)	3.804(5)	(≤ 3)	0	(0.026$\pm$0.004)
3.82692(10)	3.827(5)	($1^+, 2, 3$)	(0)	(0.007$\pm$0.003)
	3.875(5)		$\geq$1	
	3.966(5)		(0)	0.377$\pm$0.049
3.99085(21)	3.995(5)	(1 *to* 4)	(0)	
4.03403(8)	4.031(6)	($0, 1, 2$)	(0)	
4.07159(10)	4.063(5)		(0)	
	4.101(5)		(0)	
4.14083(83)	4.136(5)	($0^-, 1^-, 2^-$)	(0)	
	4.205(6)		($\geq$1)	
	4.222(6)		0	[a] (0.032$\pm$0.011)
	4.293(5)		0	0.079$\pm$0.008
4.32767(12)	4.311(6)	($1^+, 2, 3^-$)	(0)	
	4.373(5)		0	0.069$\pm$0.007
	4.413(5)		0	
4.44448(17)	4.452(8)	(≤ 3)	0	
	4.489(6)		$\geq$1	
	4.527(5)		($\geq$1)	
	4.599(5)		0	0.085$\pm$0.008
	4.630(5)		0	

[a] if the doublet (4.205$\pm$0.0053 MeV plus 4.222$\pm$5.4 MeV) is $\Delta L = 0$, $B(GT^-) = 0.055\pm0.006$ is obtained.

Table 6.4 Continuation of table 6.3

$E_x^{compilation}$ (MeV)	$E_x^{(^3He,t)}$ (MeV)	$(J^\pi)^{compilation}$	$(\Delta L)^{(3He,t)}$	$B(GT^-)^{(^3He,t)}$
	4.684(6)		(0)	(0.010±0.004)
	4.703(6)		(≥1)	
	4.744(6)		0	(0.017±0.003)
4.76339(12)	4.776(6)	(≤ 4)	≥1	
	4.816(6)		≥1	
	4.877(6)		0	
	4.916(6)		0	
	4.957(6)		0	
5.000	5.000(6)	(0 to 4^-)	(0)	0.237±0.024
	5.030(6)		(0)	
	5.053(5)		0	
	5.116(5)		0	
	5.198(5)		(0)	(0.057±0.006)
	5.227(5)		0	
	5.282(6)		0	(0.008±0.002)
	5.322(5)		(≥1)	
	5.397(5)		0	(0.030±0.004)
	5.443(6)		≥1	
	5.470(5)		≥1	
	5.513(5)		(0)	(0.021±0.003)
	5.569(6)		(≥1)	
	5.617(6)		0	(0.013±0.002)
	5.665(6)		0	(0.008±0.002)
	5.705(5)		0	(0.022±0.003)
	(5.809)		0	(0.007±0.002)
	5.864(5)		(≥1)	
	5.922(5)		(≥1)	
	5.967(5)		(0)	(0.020±0.003)
	6.003(5)		0	(0.027±0.004)
	6.042(6)		0	(0.017±0.003
	6.086(5)		0	(0.034±0.005)
	6.116(6)		(0)	(0.016±0.003)
	6.156(5)		0	0.039±0.005
	6.201(6)		0	(0.011±0.002)

Table 6.5 Continuation of table 6.4

$E_x^{compilation}$ (MeV)	$E_x^{(^3He,t)}$ (MeV)	$(J^\pi)^{compilation}$	$(\Delta L)^{(3He,t)}$	$B(GT^-)^{(^3He,t)}$
	6.268(6)		(≥1)	
	6.321(5)		0	0.044±0.005
	6.413(5)		0	0.066±0.007
	6.464(6)		(≥1)	
	6.493(6)		(≥1)	
	6.529(6)		0	(0.014±0.003)
	6.570(6)		0	(0.007±0.002)
	6.648(5)			
	6.688(6)			
	6.740(5)		(0)	(0.048±0.007
	(6.770)			
6.810(6)	6.809(6)	(0^+)	(0)	[a]
6.826(6)	6.825(5)	(0^+)	0	
	(6.915)			
	(6.957)			
	(6.989)			
	7.032(6)			
	7.077(5)		(0)	(0.057±0.007)
	(7.106)			
	...			

[a]) $B(GT^-)$=(0.163±0.023) if this level would have $J^\pi = 1^+$

$B(GT)$ units for the transitions with $B(GT^-) \geq 0.04$). The complete systematic uncertainty accounts for the error due to the background subtraction, the fitting procedure to decompose the multiplets into individual peaks, the shape of the response functions which were used and the possible deterioration of the energy resolution. It was estimated to be less than 10% for the transitions with $B(GT^-) \geq 0.04$.

Many of the obtained levels in the region 3.4 MeV $\leq E_x \leq$ 7.2 MeV have a counterpart in the literature [NDC]. A complete list of levels obtained in our study for this energy region is given in tables 6.3 - 6.5.

The angular distributions of these levels are analyzed in the middle and lower panels of fig. 6.8. As mentioned above, the background subtraction induces additional uncertainties in the determined cross sections, which can become very large, especially for the very weak peaks at scattering angles $\Theta_{scatt} > 0.3°$. The error bars on the values plotted in fig. 6.8 don't include these uncertainties. The possible overestimation of the background for $\Theta_{scatt} > 0.3°$ explains why some of the calculated ratios for these peaks become smaller than the ones for the g.s. peak. However, we are interested especially in the cross section of peaks corresponding to rather strong GT transitions ($B(GT^-) \geq 0.04$).

The decomposition of the ^{64}Cu spectra into individual peaks in the region 3.5 MeV$\leq E_x \leq$4.5 MeV is given in fig. 6.12. Complex multiplets are present and their decomposition is not always unambiguous. Six peaks around 4 MeV are grouped in a bump that behaves mostly like a $\Delta L = 0$ peak. The GT strength for the transitions to this group of levels was calculated by assuming no higher order multipole contributions. We estimate that not including possible $\Delta L \geq 1$ components induces an uncertainty in the obtained $B(GT^-)$ value of less than 10%. Therefore we indicate a value $B(GT^-) = 0.377 \pm 0.049$ for this group (see table 6.3).

Following the fit shown in fig. 6.12 and assuming a $\Delta L \geq 1$ character for the 4.205±0.006 MeV component of the doublet at about 4.2 MeV, a $B(GT^-)$ value of 0.032±0.011 is calculated for the second component at 4.222±0.006 MeV. By checking the compiled data, no information can be find for a level in this excitation energy region, therefore we don't have any indication concerning the character of the observed transitions. But the angular distribution of this doublet can suggest a $\Delta L = 0$ character, therefore an "artificial" shift of the cross section from one peak to the other, due to the fitting procedure, can be considered. A $B(GT^-)$ value of 0.055±0.006 is deduced for the doublet in this case.

Because they couldn't be separated with the present energy resolution, we

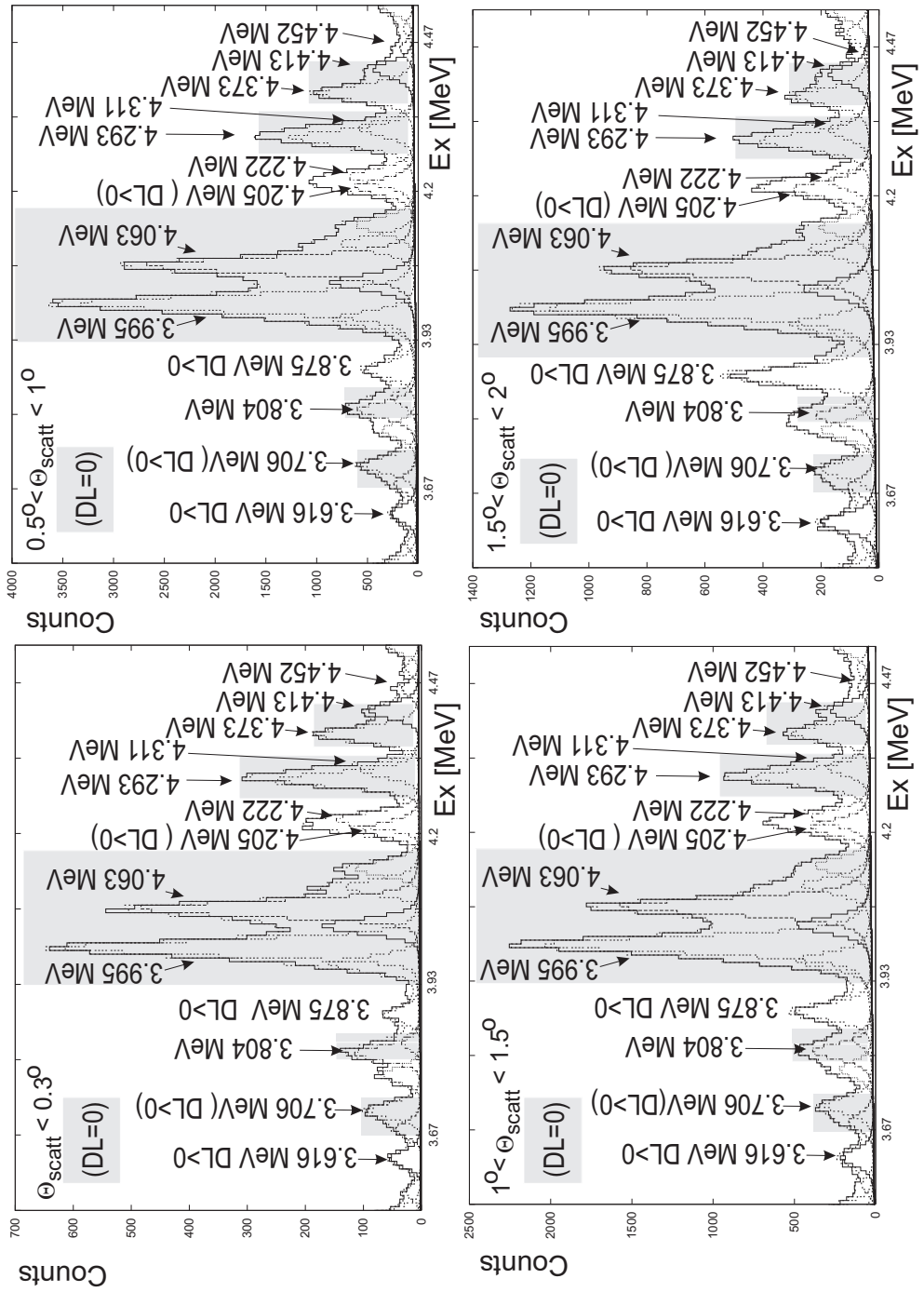

Figure 6.12 ^{64}Ni(^{3}He, t)^{64}Cu reaction: Fit of the 3.5 MeV$\leq E_x \geq$4.5 MeV region in ^{64}Cu spectra.

proceeded in the same way and calculated the strength for the triplet containing the peaks at: 4.373±0.005 MeV, 4.413±0.005 MeV and 4.452±0.008 MeV. This last peak almost disappears in the background for $1.5° \leq \Theta_{scatt} \leq 2°$ (see fig. 6.12).

The fit in the region 4.465 MeV$\leq E_x \leq$5.8 MeV is shown in fig. 6.13. A $B(GT^-) = 0.085 \pm 0.006$ value was calculated for the doublet containing the peaks at 4.599±0.005 MeV and at 4.630±0.005 MeV and showing a ΔL=0 angular distribution. Similarly, $B(GT^-) = 0.057 \pm 0.006$ for the doublet at 5.21 MeV, containing the 5.198±0.005 MeV and 5.227±0.005 MeV peaks. If in the first spectrum ($\Theta_{scatt} \leq 0.30°$) the peak at 5.116±0.005 MeV can be separated from the multiplet in the left side, this is impossible at higher angles, especially for the $1.5° \leq \Theta_{scatt} \leq 2°$ spectrum. Our decomposition of the multiplet around 5 MeV is to a large extend arbitrary. A level at 5.000 MeV is indicated in literature for this excitation energy region and the position of a peak in the spectra with $1.5° \leq \Theta_{scatt} \leq 2°$ and $1° \leq \Theta_{scatt} \leq 1.5°$ was allowed to vary by ±10 keV around this excitation energy. No constraints were imposed for the fit for the $\Theta_{scatt} \leq 0.30°$ and $0.5° \leq \Theta_{scatt} \leq 1°$ spectra in this energy region. Although the level at 5.000 MeV is suggested to have $J^\pi = 0$ *to* 4^- [NDC], the peak corresponding to it in our spectra doesn't seem to follow a $\Delta L \geq 1$ angular distribution. The complete multiplet shows an angular distribution similar to those of the two doublets discussed above and deduced to have $\Delta L = 0$. If we assume that no higher order components contribute to this multiplet, a $B(GT^-) = 0.237 \pm 0.024$ value is calculated. The 5.116±0.005 MeV peak is taken into account in this estimation.

The angular distribution of some other peaks suggests a GT character, but all these are weak transitions. By contrast, we notice that the doublet containing the 5.443±0.006 MeV and 5.470±0.005 MeV peaks, for the cross section increases with the angle, showing a $\Delta L \geq 1$ character.

The fit of the region 5.8 MeV$\leq E_x \leq$6.6 MeV is shown in fig. 6.14. The presence of the 5.809±0.007 MeV peak is questionable, therefore it was indicated between brackets in table 6.4. The background is high in this energy region and the peaks are not very intense. The region looks to be dominated by peaks corresponding to $\Delta L = 0$ transitions. Two strong peaks at 6.321±0.005 MeV and at 6.413±0.005 MeV are present here. The calculated strengths are given in table 6.5.

Figure 6.15 shows the fit in the region where the IAS of the target (^{64}Ni) g.s. is located. The lower panel of fig. 6.8 suggests a $\Delta L = 0$ character for almost all the peaks in this part of the spectrum. But, apart from the IAS of the ^{64}Ni g.s. and the 6.810 MeV peaks, most of the peaks are rather weak.

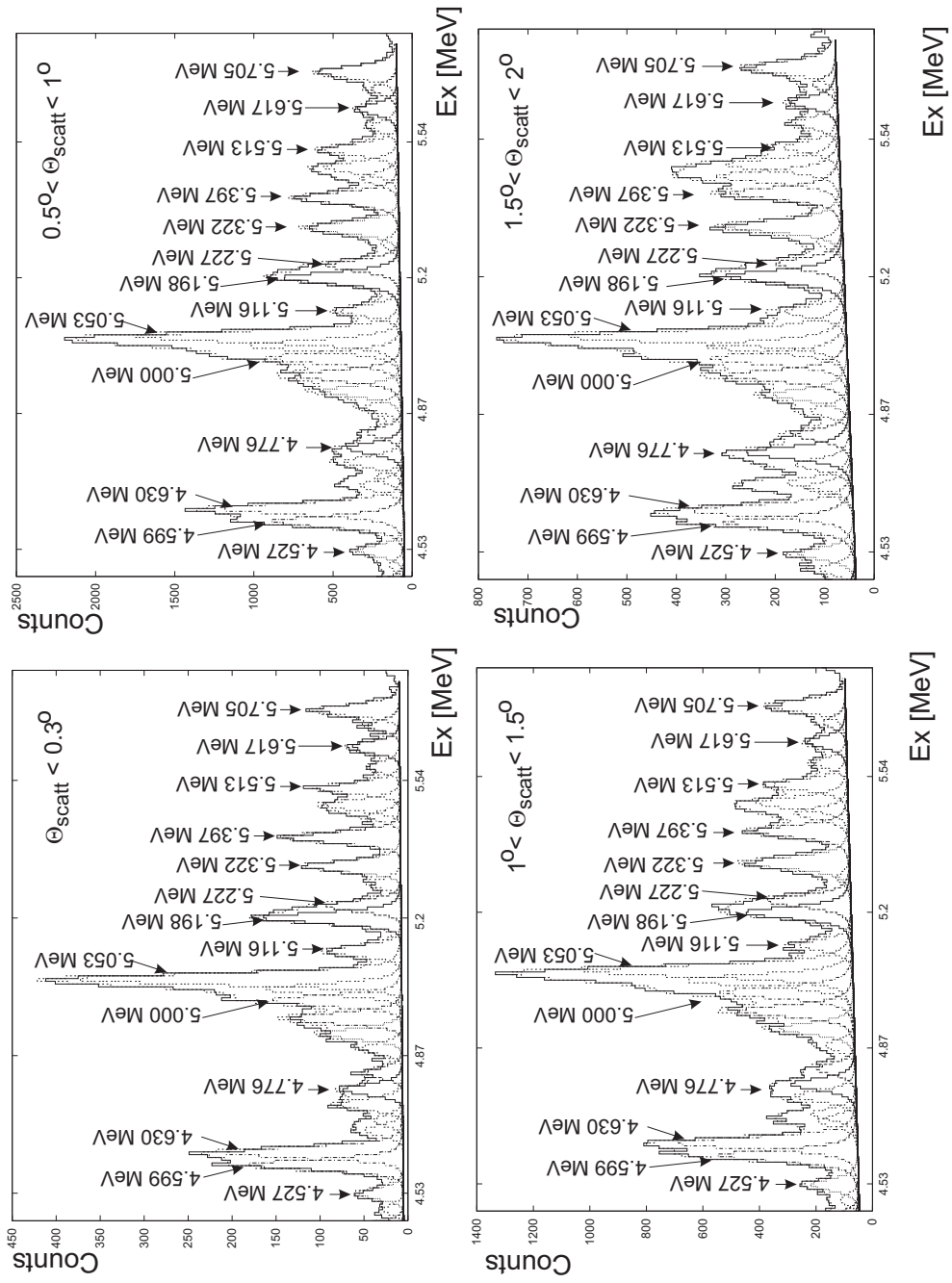

Figure 6.13 ^{64}Ni(^{3}He, t)^{64}Cu reaction: Fit of the 4.465 MeV$\leq E_x \geq$5.8 MeV region in ^{64}Cu spectra.

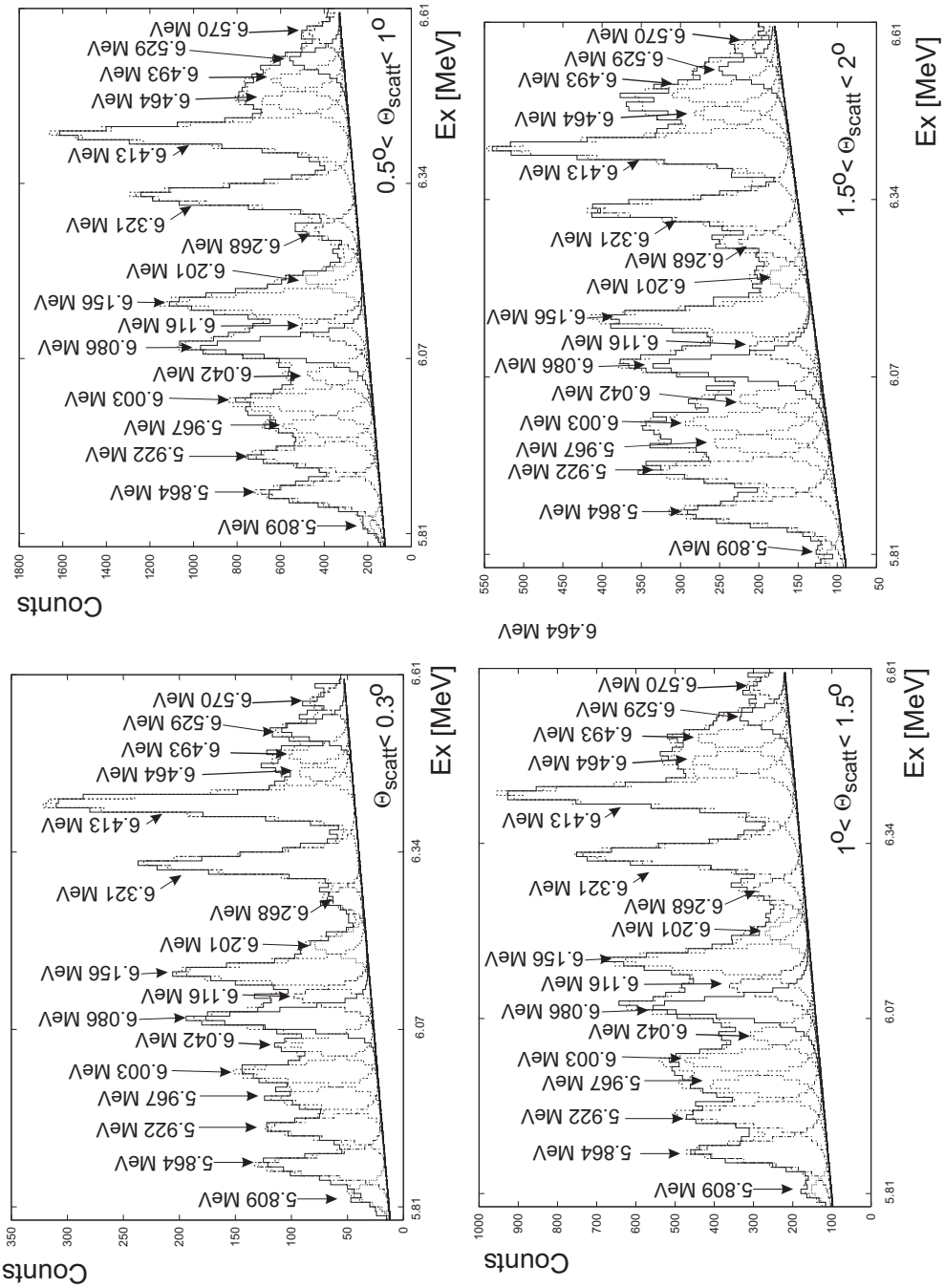

Figure 6.14 ^{64}Ni(^{3}He, t)^{64}Cu reaction: Fit of the 5.8 MeV$\leq E_x \geq$6.6 MeV region in ^{64}Cu spectra.

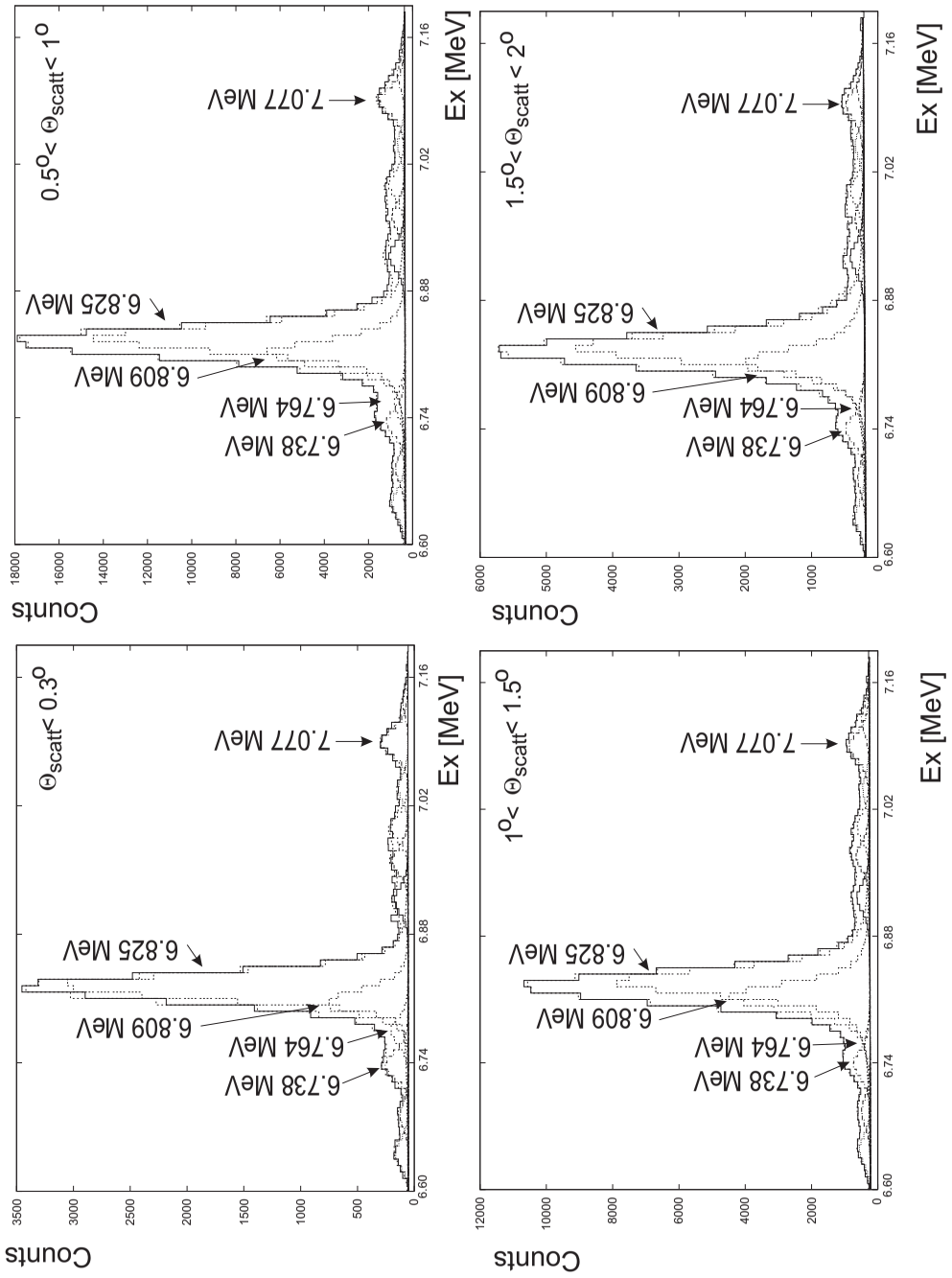

Figure 6.15 ^{64}Ni(^{3}He, t)^{64}Cu reaction: Fit of the 6.6 MeV$\leq E_x \geq$7.2 MeV region in ^{64}Cu spectra.

However, we notice a peak at 6.738 MeV and a peak at 7.077 MeV for which $B(GT^-) > 0.04$.

The transition to the IAS of the ^{64}Ni g.s. is the strongest transition in the spectrum, appearing at 6.825±0.005 MeV. It is not expected to have other very intense transitions at these excitation energies. Nevertheless the analysis of the peak shows a second level, at about 16 keV below the IAS, which is very well populated. This peak amounts about 23% of the IAS peak being stronger than, e.g., the g.s peak. The two levels were observed in a previous ^{64}Ni(^{3}He, t)^{64}Cu measurement with a 24.6 MeV ^{3}He beam by Becchetti et al. [Bec70]. The energy resolution for their spectrum is about 8 keV, therefore the peaks corresponding to the two levels could be clearly separated. They appear at 6.810 MeV and at 6.826 MeV, although observed with poor statistics. Due to the insufficient beam energy, the results of Becchetti et al. could give no information about the transition strengths. They explain the presence of this second strong transition by the isospin mixing of the $T = T_0$ IAS of the target g.s. with the $T = T_0 - 1$ state at 6.810 MeV, due to a charge-dependent part of the interaction, like the Coulomb term. The condition is that the 6.810 MeV level has the same spin and parity as the IAS, which, for ^{64}Cu, is $J^\pi = 0^+$. Therefore the Fermi strength is fragmented over the IAS of ^{64}Ni g.s. and the nearby other 0^+ state at 6.810 MeV. Thus, when determining the F strength, we should include the cross section of the doublet.

Although it isn't favored, the $\Delta L = 0$ character of the 6.809 MeV peak is not excluded by our analysis. A very plausible explanation for the unclear behavior of the angular distribution of this level (see fig. 6.8) is an inaccurate fit of the doublet. E.g, part of the cross section of the peak at 6.764 MeV, which almost disappears at scattering angles larger than 1°, could be wrongly attributed to the 6.809 MeV peak. At scattering angles $\Theta_{scatt} \geq 0.5°$, for which the energy resolution deteriorates, part of the cross section of the IAS peak could artificially shift to this peak. As the two levels could not be distinguished when determining the coefficients for the corrections of the angular aberrations (see section 6.1) the applied corrections might be less accurate. Therefore the energy resolution for this region can be larger than the one determined for the low excitation energy region of each spectrum. As a consequence, the fit of the doublet, by using the shape of the g.s. peak and a fixed width, becomes less accurate in this case.

Considering the fragmentation of the Fermi strength over the two states is very important if we want to determine the R^2 ratio of GT and F unit cross sections discussed in section 2.2.2. A value of R^2=9.12±1 is obtained based on this assumption. The value R^2=11.2±1.2 is obtained when assuming that

the Fermi strength is concentrated exclusively in the peak at 6.825 MeV. The determined uncertainties include statistical and systematic errors. Fig. 6.16 shows the fit of the R^2 distribution obtained when including our experimental result: *a*) R^2=9.12±1 and *b*) R^2=11.2±1.2. The previous fit (without including the value for ^{64}Ni) is given for comparison. The figure suggests that the R^2 for ^{64}Ni should, in fact, be somewhere in between the two determined values. Large uncertainties are induced by the background substraction and the possible overestimation of the 6.810 MeV peak cross section.

The GT strength distribution for $E_x \leq$7.2 MeV obtained in our study is given in fig. 6.17. The indicated uncertainties include only statistical errors. The sum $B(GT^-)$ as function of excitation energy is plotted in fig. 6.18. The maximum strength obtained in the excitation energy region 3.4 $MeV \leq E_x \leq$ 7.2 MeV is:

$$\sum_{3.4\ MeV \leq E_x \leq 7.2\ MeV} B(GT^-) \approx 1.6$$

⋆ **^{64}Cu excitation energy region $E_x \geq$7.2 MeV**

In order to estimate the GT strength at even higher excitation energies, a reasonable estimation of the background has to be given. If we assume the background as shown in fig. 6.19 and if we assume that this background includes, in the excitation energy region from about 7.2 MeV to about 15.4 MeV, the contributions of higher multipole structures and the remaining part is exclusively the GTGR, the strength of this giant resonance can be calculated. A value of $B(GTGR) \approx 5$ is obtained. It has to be noticed that this is only a rough estimation in order to get an idea of the maximum strength that is found in our study. A maximum total strength of $\sum B(GT^-) \approx$8 is obtained in this way. This value represents only about one third of the total strength predicted by the Ikeda sum rule (see section 3.4): $S_{\beta^-} = 3$(N-Z) + $S_{\beta^+} \geq$ 24. Missing of the strength compared to the predicted GT strength is a well known phenomenon. It was discussed in detail in section 3.1. An investigation at still higher excitation energies, could bring more information.

Some more spectroscopic information can be deduced from our data. Apart from a suggested 2^+ level at 8.170 MeV (the isobaric analogue of the first 2^+ state in ^{64}Ni), there is no further information of levels above the IAS of ^{64}Ni g.s. in the compiled data. Although the spectrum obtained in our measurement is dominated at this excitation energies by the huge bump of the GTGR around 10 MeV, there are several peaks that could be clearly identified. They are indicated by their excitation energy in table 6.6. We estimate the accuracy of the indicated energies of about 30 keV.

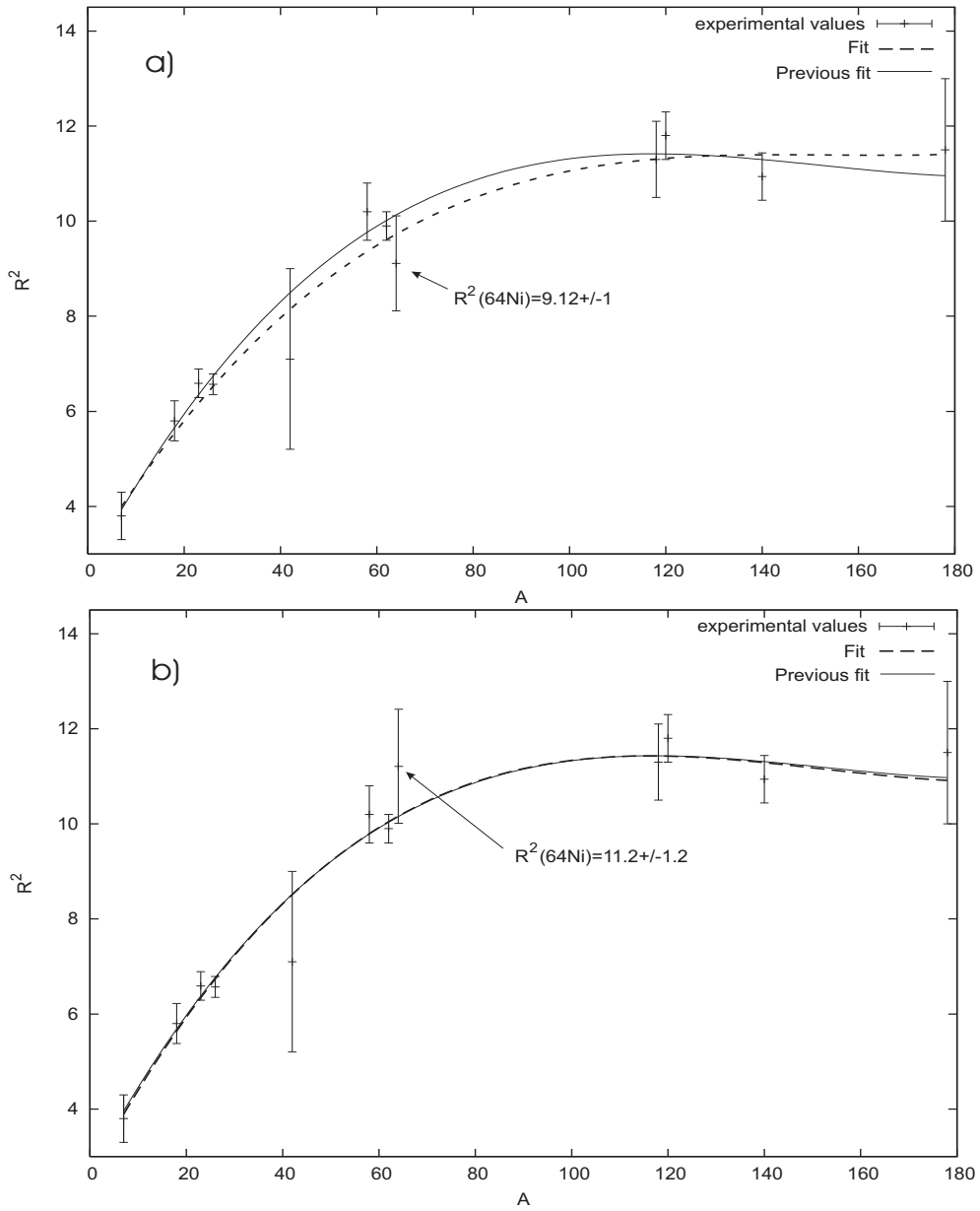

Figure 6.16 The dependence of R^2 on the mass number (see fig. 2.8). *a*) The obtained $R^2(^{64}\mathrm{Ni}) = 9.12\pm1$ value is taken into account. *b*) The obtained $R^2(^{64}\mathrm{Ni}) = 11.2\pm1.2$ value is taken into account (see text for details). The full line represents the fit from the fig. 2.8.

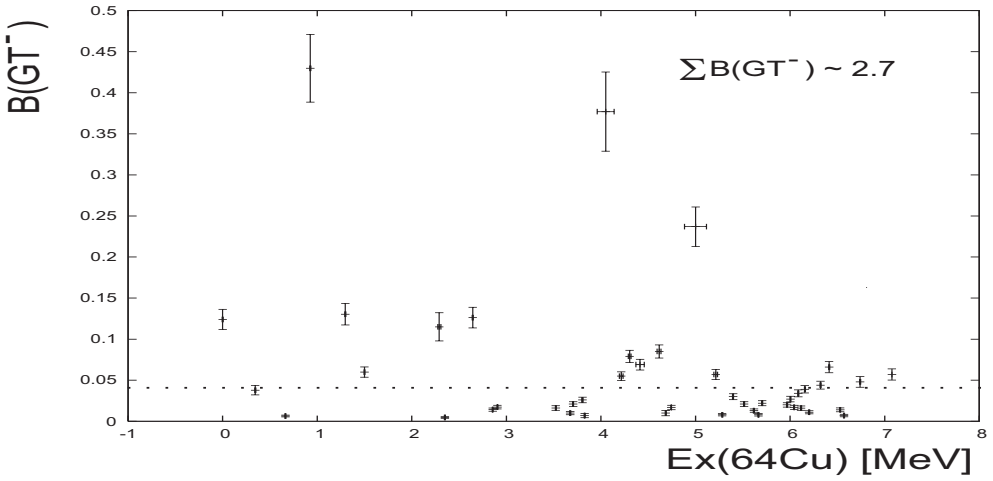

Figure 6.17 The $B(GT^-)$ distribution in the low excitation energy region of ^{64}Cu, assuming that transitions showing $\Delta L = 0$ behavior have GT character. The dotted line corresponds to $B(GT^-) = 0.4$

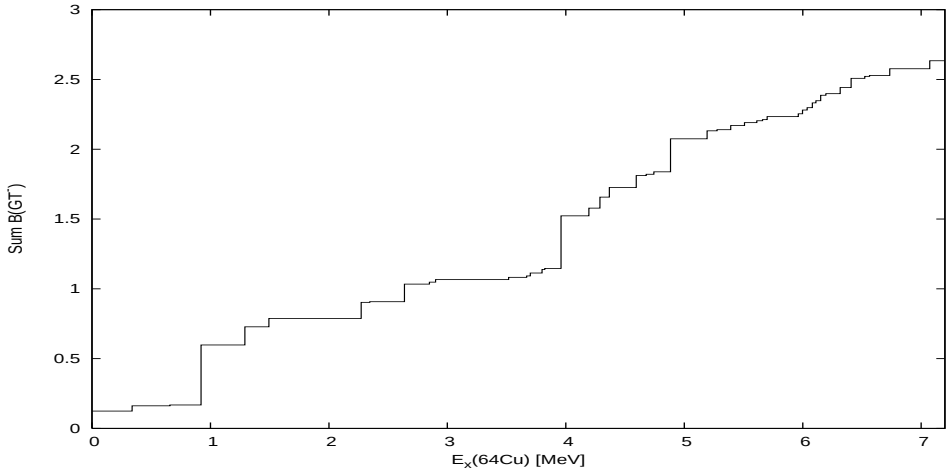

Figure 6.18 The sum of the $B(GT^-)$ found in the low excitation energy region of ^{64}Cu.

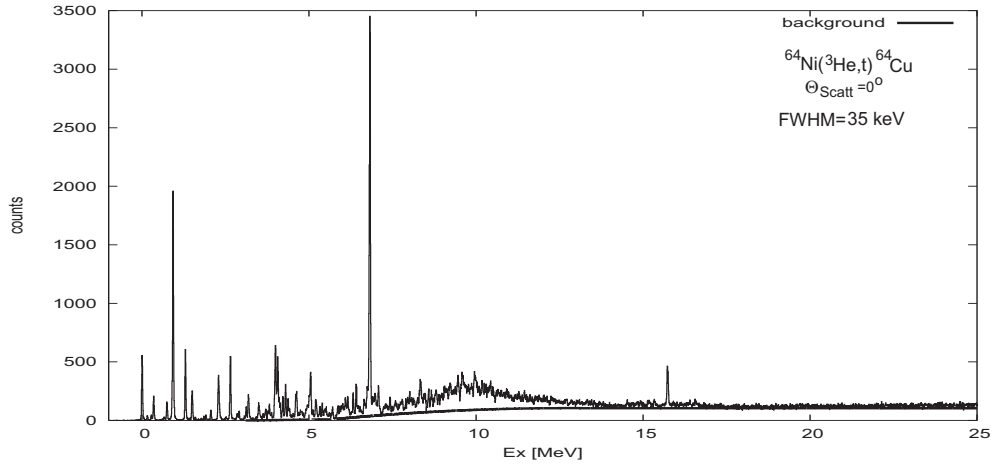

Figure 6.19 Estimation of the background in the ^{64}Cu 0° spectrum.

Table 6.6 Indication of peaks in the $E_x \geq 7.2$ MeV region. The energies are given in MeV. An accuracy of the order of 30 keV was estimated.

7.425	8.330	9.590	10.503
7.588	8.582	9.970	10.608
7.677	8.668	10.187	11.445
7.895	8.890	10.256	
7.951	9.380	10.306	
8.011	9.457	10.430	

A part of these peaks can correspond to isobaric analogue states of states in ^{64}Ni. E.g. the states at 9.970 MeV, 10.256 MeV and 10.306 MeV could be the isobaric analogue states of the 3.163 MeV, 3.396 MeV and 3.482 MeV states in ^{64}Ni, having $J^\pi = 2^+$ [NDC]. The peak at 10.608 MeV can correspond to the isobaric analogue state of the 3.797 MeV (1^+ to 5^+) state in ^{64}Ni and the one at 11.445 MeV the isobaric analogue state of the 4.360 MeV 2^+ state in ^{64}Ni [NDC]. These attempts of identification of isobaric analogue states are based on the assumption that all the observed peaks in the spectrum belong to ^{64}Cu, which is a reasonable assumption as the enrichment of the measured target is 97.92%. The contributions from the ^{12}N levels, due to the ^{12}C contamination of the target, starts only at 15.663 MeV, where the ^{12}N g.s. peak is located.

Chapter 7

Conclusions and Outlook

This thesis presents a study of GT transitions starting from the g.s. of ^{64}Ni in the β^+ and β^- direction. The investigation was done via (d,^{2}He) and (^{3}He,t) CE reactions on ^{64}Ni. The (d,^{2}He) experiment was performed at the Big-Bite Spectrometer, KVI, Groningen, with a 170 MeV deuteron beam. The complementary reaction, (^{3}He,t), was studied at the Grand Raiden Spectrometer, RCNP, Osaka, with a 420 MeV ^{3}He beam.

The results of each of the two experiments have been discussed in sections 5.7 and 6.6. Due to the unprecedented energy resolution achieved in the two experiments, new spectroscopic information could be given both for ^{64}Co and ^{64}Cu.

Both transitions from ^{64}Co g.s. and from ^{64}Cu g.s. to ^{64}Ni g.s. are allowed GT β transitions, with $(\log ft)_{64Co->64Ni} = 4.3$ and $(\log ft)_{64Cu->64Ni} = 5$, as determined in β-decay studies [Fir96]. Therefore we are facing a unique situation that allows to measure directly the unit cross sections. In this way an absolute calibration connecting the reaction cross sections with the transition strengths becomes available in both cases, which allows a reliable determination of the transition strengths to excited states in ^{64}Co and ^{64}Cu. The two obtained unit cross sections will be used for determining the general dependence of the unit cross section on the mass number, both for (d,^{2}He) and (^{3}He,t) reactions.

The results of our study can be used for testing theoretical model calculations but also, by combining the obtained total strengths, S_{β^+} and S_{β^-}, the model independent Ikeda sum rule [Ike63] of GT strength can be checked. For this reason the total GT strength obtained in the two reactions has to be given.

Although characterized by the best energy resolution (FWHM$\approx$110 keV)

achieved at the moment in a CE reaction in the β^+ direction at intermediate beam energies, the ^{64}Co spectrum obtained in the (d,^{2}He) reaction is still dominated by unresolved collective excitations forming a huge bump around 11 MeV. Therefore only the lower limit of the summed strength can be given $S_{\beta^+} \geq$1.093 (or 1.033 - see section 5.7 for details). This value was obtained by including the transitions to individual states identified in the low energy region, $E_x \leq$2.6 MeV. On the other hand, the very good energy resolution, FWHM≈35 keV, that characterizes the ^{64}Cu spectrum obtained in the (^{3}He, t) reaction enabled, the good separation of peaks only in the excitation energy region $E_x \leq$3 MeV. Our attempt to decompose the spectrum into individual peaks up to E_x = 7.2 MeV (=S_p) was discussed in section 6.6. For the extraction of the strength contained by the GTGR, which lies around 10 MeV in the ^{64}Cu spectrum, the background containing contributions from the QFS processes, GDR and IVGMR has to be estimated. As the GDR and the IVGMR are expected at about 25 MeV and 35 MeV in ^{64}Cu, they will not contribute considerably to the bump located at about 10 MeV. The value $S_{\beta^-} \approx 8$ for the total GT strength extracted in our study is just an estimation of the maximum strength that is obtained in our measurement when assuming the background as in fig. 6.19. If however this background is overestimated, the GT strength located in the excitation energy region around 10 MeV might be larger that we deduced.

Even such a rough estimation cannot be given for the ^{64}Co spectrum obtained in the (d,^{2}He) reaction. In this case, the SGDR and SIVGMR are expected at about 8 - 9 MeV and 25 MeV in ^{64}Co, therefore they contribute substantially to the very broad bump located at about 10 MeV even for small scattering angles like $\theta_{scatt} \leq 1^\circ$.

From the two strengths, the value S_{β^-} - $S_{\beta^+} \approx 6.9$ was determined. This represents only about 29% of the strength predicted by the sum rule: 3(N-Z)=24 and could indicate the necessity of investigating even higher excitation energy regions. In a similar study on ^{58}Ni only 32% of the full sum rule prediction was obtained [Fuj01a].

The present results have important applications in astrophysics. The main processes which occur during the presupernova phase in the core collapse of a massive star are electron capture and β-decay [Bet79, Ful80] of nuclei in the iron mass region. These processes are mainly proceeding via GT (and F) transitions, therefore an accurate description of the GT strengths for the g.s. and the lowest excited states of fp-shell nuclei is required [Lan99]. Nowadays experimental techniques allow a good determination of GT strength distributions. But not all the nuclei in this mass region are accesible experimen-

tally. Therefore theoretical approaches are used employing the interacting shell model. Experimental results are highly demanded for tunning the theoretical models developed in the frame of the shell model, e.g., the Large Scale Shell Model (LSSM) [Lan99, Lan00, Lan01] or the Shell Model Monte Carlo (SMMC) [Hon96, Rad97, Ots98, Cau99b] by using different defined inteactions.

The experimental results presented in this thesis, are very important for the study mentioned above. Because of the insufficient energy resolution characterising the ^{64}Ni(n,p) studies [Wil95], the GT strengths of transitions to low lying individual states in ^{64}Co could not be measured. Therefore our study gives the first $B(GT^+)$'s for transitions to individual states in the low excitation energy region of ^{64}Co.

Although the stellar electron capture and β-decay are more senstive to the $B(GT^+)$, also the $B(GT^-)$ distribution is of importance in the calculations of the stellar weak interaction rates. [Sar03]. Our ^{64}Ni(^{3}He$,t$) study gives for the first time the $B(GT^-)$ distribution to states in ^{64}Cu.

The GT strengths obtained in our work provide also information that allows (in combination with ^{64}Zn(d,^{2}He) results [ea]) the calculation of the double β decay probability of ^{64}Zn. The double β decay is belived to proceed as a combination of two sequential virtual decays: from the parent nucleus to the intermediate nucleus (energetically forbidden in the ^{64}Zn $\longrightarrow$^{64}Cu case), followed by the decay to the daughter-nucleus, ^{64}Ni. It proceeds thus as a second-order transition of the weak interaction, and the transition matrix element is in principle the product of two ordinary β-decay matrix elements, both of GT-type, between the initial and intermediate state and between the intermediate and final state. To obtain the total transition probability a summation over all the involved intermediate states is needed (see ref. [Rak04]). This assumes thus knowledge of the matrix elements of the GT transitions between ^{64}Zn g.s. and ^{64}Ni g.s. and the low lying levels in ^{64}Cu.

The $B(GT^-)$ values in ^{64}Cu obtained in our ^{64}Ni(^{3}He$,t$) experiment will be combined with the $B(GT^+)$ values in ^{64}Cu obtained in the ^{64}Zn(d,^{2}He) experiment performed recently at KVI [ea]. This will enable to determine the $2\nu\beta\beta$ decay matrix elements and calculate the half-life of the parent nucleus ^{64}Zn in a similar way as done for ^{48}Ca (see ref. [Rak04]).

The two experiments presented in this thesis are also part of a complex study of the isobaric analogue states in ^{64}Co, ^{64}Ni, ^{64}Cu nuclei. As the isospin of the ^{64}Ni g.s is T=4, states in ^{64}Cu with T= 3, 4 and 5 are excited via CE reactions on ^{64}Ni in the β^- direction, states with T = 5 in ^{64}Co via CE

reactions on ^{64}Ni in the β^+ direction and states with T= 4 and 5 in ^{64}Ni via IE scattering reactions on ^{64}Ni. If we assume that the nuclear interaction is charge symmetric, the T = 5 states ideally appear in all three nuclei at the same excitation energies (after correction for the Coulomb displacement) and with corresponding strengths (depending on the isospin CG coefficients) as discussed in section 2.3. Similarly, the T = 4 states should appear at corresponding excitation energies and with corresponding strengths in ^{64}Cu and ^{64}Ni. The different isospin components are excited in different ways in the three reactions. Because of the rather high neutron excess, it turns out that each of the mentioned reactions is suitable only for the investigation of the lower isospin component excited in the respective reaction. Therefore all three type of experiments are mandatory for a complete study of the spin-isospin-flip transitions starting from the ^{64}Ni g.s.

To complete the investigation of T=5 spin-isospin (namely GT) excitations in ^{64}Co and T = 3, 4 and 5 GT excitations in ^{64}Cu by using the (d,^{2}He) and (^{3}He, t) CE reactions on ^{64}Ni, spin- and spin-isospin (M1) excitations of T=4 and 5 states in ^{64}Ni will be investigated by using the ^{64}Ni(p, p') reaction. Very forward angles measurements are imperative for determining the M1 transition strengths. Due to the typical difficulties of a 0° (p, p') measurement, only a few facilities in the world allow such a measurement. A very successful test run was done at the RCNP, Osaka. Important progress was also achieved in a test run at the iThemba LABS (Cape Town, South Africa). Thus, in the near future (p, p') 0° measurements are expected.

Some suggestions for the identification of isobaric analogue of ^{64}Ni states in ^{64}Cu have been discussed in section 6.6. An accurate identification of the T=4 and 5 states can only be made by comparing the ^{64}Ni$(^3$He$, t)^{64}$Cu and ^{64}Ni$(p, p')^{64}$Ni spectra. A previous ^{64}Ni(p, p') measurement, taken at 4° scattering angles by the group of Marty et al [Mar83], suggested that the first T=5 state in ^{64}Ni (the IAS of ^{64}Co g.s.) is located at 15.62 MeV. This result is confirmed by our 0° test measurement at RCNP. The 15.62 MeV state is shown very clearly, as a well populated state on top of the giant E1 resonance in ^{64}Ni. As the IAS of ^{64}Ni g.s. in ^{64}Cu is located at 6.826 MeV, the energy region $E_x \geq$ 22.4 MeV is expected for the transitions to T=5 states in ^{64}Cu. In the present ^{64}Cu$(^3$He$, t)$ spectra, no indication for the IAS of ^{64}Co g.s. can be found. This is in agreement with the expected very weak intensity, according to the isospin CG coefficients: only about 2% of the total GT strength in ^{64}Cu is expected to be contained by the transitions to T=5 levels. Therefore the IAS of ^{64}Co g.s. is hidden by the continuum background.

This study of the isobaric analogue states can be further extended to other

Ni isotopes for getting a systematic understanding of the energy spacing between different isospin components and their relative intensities. With this aim, we already measured the ^{60,62}Ni(^{3}He, t) reactions at RCNP. The data analysis is in progress. ^{60,62}Ni(p, p') 0° measurements are also planed for the near future. These data have to be further combined with ^{60,62}Ni(d,^{2}He) data.

A similar study was already completed by H. Fujita for ^{58}Ni (see ref. [Fuj01a]), by combining the ^{58}Ni(^{3}He, t) measurement performed at the RCNP [Fuj01a, Fuj02b], the ^{58}Ni(p, p') 0° measurement at the IUCF [Fuj01a] and the ^{58}Ni(d,^{2}He) measurement at the KVI [Hag01, Hag05].

Fig. 7.1 shows the theoretical expectations for the different isospin components excited in ^{58,60,62,64}Cu. The position of the centroids and the intensities for the different T components are indicated for the four nuclei. In a first approximation, without taking into account the coupling between the g.s. isospin T_0 and the isospin of the vibrational motion, the intensity ratios of the different isospin components are given by the square of the corresponding CG coefficients (see section 2.3) for those components. The intensities indicated in fig. 7.1 have been obtained in this way. The energy spacing between the three centroids was deduced from the symmetry energy term in the mass formula and calculated as indicated by Bohr and Mottelson [Boh98] (see section 2.3 for details).

The increase of the energy spacing with increasing the isospin is clearly observed also experimentally. Fig. 7.2 presents the ^{60,62,64}Cu spectra that we obtained in the mentioned (^{3}He, t) reactions. The first T_0 state, the IAS of the target g.s is used as a reference in the spectra. Because it is expected that most of the $T_0 - 1$ strength is located in the excitation energy region below the IAS of the target g.s., the predicted increase of the energy spacing with increasing the isospin number is clear.

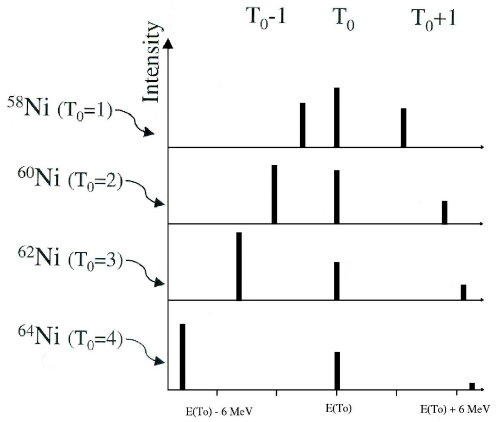

Figure 7.1 The relative position of the centroids and the relative intensities for different isospin components in ^{58,60,62,64}Cu. The value of the g.s. isospin for different target nuclei is indicated.

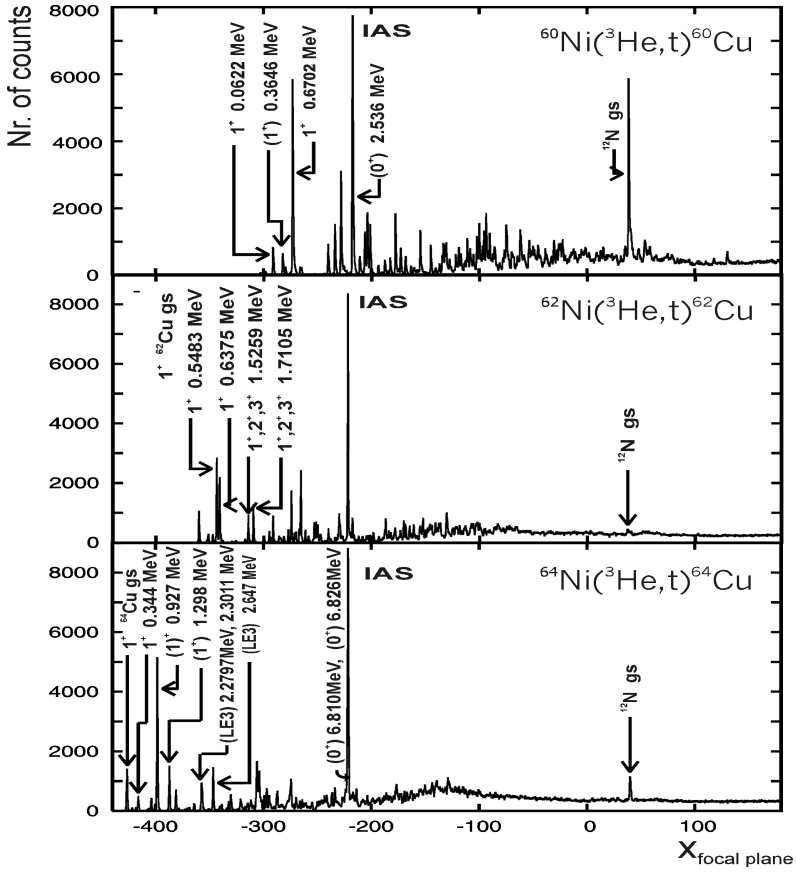

Figure 7.2 The 0° ^{60,62,64}Cu spectra obtained in the (^{3}He, t) reactions performed at RCNP.

Appendix A

Wave functions

In the following tables the 1p-1h matrix elements used to calculate the differential cross sections for the ^{64}Ni(d,^{2}He)^{64}Co reaction, are given. The calculations were carried out with the computer code `NORMOD` [vdW] and served as an input for the DWBA calculations performed with the computer code `ACCBA` [Oka99].

hole state (proton)	particle state (neutron)	matrix element $\Delta L = 0, \Delta J^\pi = 1^+, 0\hbar\omega$	$\Delta L = 2, \Delta J^\pi = 3^+$
$2p1/2$	$2p1/2$	-0.0121	–
$2p1/2$	$1f5/2$	–	0.0064
$2p1/2$	$2p3/2$	-0.0418	–
$1f5/2$	$1h11/2$	–	-0.1539
$1f5/2$	$2p1/2$	–	0.0045
$1f5/2$	$1f5/2$	-0.0941	0.0248
$1f5/2$	$2p3/2$	–	0.0099
$2p3/2$	$2p1/2$	0.0588	–
$2p3/2$	$1f5/2$	–	-0.0196
$2p3/2$	$2p3/2$	0.0804	-0.0595
$1f7/2$	$1h11/2$	–	0.3598
$1f7/2$	$2p1/2$	–	-0.1221
$1f7/2$	$1f5/2$	0.6547	-0.2035
$1f7/2$	$2p3/2$	–	-0.1293
$1d3/2$	$2d3/2$	–	-0.0248
$1d3/2$	$1g7/2$	–	-0.0960
$1d3/2$	$2d5/2$	–	-0.0810
$1d3/2$	$1g9/2$	–	-0.3918
$2s1/2$	$2d5/2$	–	0.2504
$1d5/2$	$3s1/2$	–	0.1197
$1d5/2$	$2d3/2$	–	0.0810
$1d5/2$	$1g7/2$	–	0.1109
$1d5/2$	$2d5/2$	–	0.1487
$1d5/2$	$1g9/2$	–	0.2653

Table A.1 The matrix elements for $\Delta L = 0, \Delta J^\pi = 1^+, 0\hbar\omega$ and $\Delta L = 2, \Delta J^\pi = 3^+$ transitions used to describe the ^{64}Ni(d,^{2} He)^{64}Co reaction.

hole state (proton)	particle state (neutron)	matrix element $\Delta L = 1, \Delta J^\pi = 1^-$
$2p1/2$	$3s1/2$	-0.0330
$2p1/2$	$2d3/2$	0.0309
$1f5/2$	$2d3/2$	-0.0327
$1f5/2$	$1g7/2$	0.0830
$1f5/2$	$2d5/2$	-0.0525
$2p3/2$	$3s1/2$	0.0401
$2p3/2$	$2d3/2$	-0.0950
$2p3/2$	$2d5/2$	-0.0712
$1f7/2$	$1g7/2$	-0.4968
$1f7/2$	$2d5/2$	0.1521
$1f7/2$	$1g9/2$	-0.3353
$1d3/2$	$2p1/2$	-0.0407
$1d3/2$	$1f5/2$	0.2124
$1d3/2$	$2p3/2$	-0.0891
$2s1/2$	$2p1/2$	-0.0910
$2s1/2$	$2p3/2$	-0.0787
$1d5/2$	$1f5/2$	-0.3405
$1d5/2$	$2p3/2$	0.0668

Table A.2 The matrix elements for $\Delta L = 1, \Delta J^\pi = 1^-$ transitions used to describe the ^{64}Ni(d,^{2} He)^{64}Co reaction.

hole state (proton)	particle state (neutron)	matrix element $\Delta L = 0, \Delta J^\pi = 1^+, 2\hbar\omega$
$2p1/2$	$3p1/2$	0.0185
$2p1/2$	$3p3/2$	0.0523
$1f5/2$	$2f5/2$	0.0555
$1f5/2$	$2f7/2$	0.0994
$2p3/2$	$3p1/2$	-0.0899
$2p3/2$	$3p3/2$	-0.1005
$1f7/2$	$2f5/2$	-0.3864
$1f7/2$	$2f7/2$	-0.3347
$1d3/2$	$2d3/2$	0.1497
$1d3/2$	$2d5/2$	0.2993
$2s1/2$	$3s1/2$	-0.2828
$1d5/2$	$2d3/2$	-0.2993
$1d5/2$	$2d5/2$	-0.2800
$1p1/2$	$2p1/2$	0.0272
$1p1/2$	$2p3/2$	0.0943
$1p3/2$	$2p1/2$	-0.0771
$1p3/2$	$2p3/2$	-0.1054

Table A.3 The matrix elements for $\Delta L = 0, \Delta J^\pi = 1^+, 2\hbar\omega$ transitions used to describe the ^{64}Ni(d,^{2} He)^{64}Co reaction.

Bibliography

[And80] B.D. Anderson, J.N. Knudson, P.C. Tandy, J.W. Watson, R. Madey, and C.C. Foster, Phys. Rev. Lett. **45** (1980) 699–702.

[Ari99] A. Arima, Nucl. Phys. **A649** (1999) 260c–270c.

[Asa00] M. Asai, T. Ishii, A. Makishima, I. Hossain, M. Ogawa, and S. Ichikawa, Phys. Rev. **C62** (2000) 054313.

[Aue71] N. Auerbach, Phys. Lett. **B36** (1971) 293–296.

[Aue89] N. Auerbach, F. Osterfeld, and T. Udagawa, Phys. Lett. **B219** (1989) 184–188.

[Bäu01] C. Bäumer, R. Bassini, A.M. van den Berg, D. De Frenne, D. Frekers, M. Hagemann, V.M. Hannen, M.N. Harakeh, J. Heyse, M.A. de Huu, E. Jacobs, M. Mielke, S. Rakers, R. Schmidt, H. Sohlbach, and H.J. Wörtche, Phys. Rev. **C63** (2001) 037601.

[Bäu04] C. Bäumer, *Faces of the* $(d,^2\mathrm{He})$ *charge-exchange reaction: from nucleon-nucleon studies to stellar electron-capture*, Ph.D. thesis, Institut für Kernphysik, Universität Münster, *in preparation*, 2004.

[Bec70] F.D. Becchetti, D. Dehnhard, and T.G. Dzubay, Nucl. Phys. **A168** (1970) 151–176.

[Ber77] G.F. Bertsch, J. Borysowicz, and H. McManus, Nucl. Phys. **A284** (1977) 399–419.

[Bet79] H.A. Bethe, G.E. Brown, J. Applegate, and J.M. Lattimer, Nucl. Phys. **A324** (1979) 487–533.

[Boh98] A. Bohr and B.R. Mottelson, *Nuclear Structure, Volume I and II*, second ed., World Scientific, 1998.

[Bow62] P.H. Bowen, C. Cox, G. Huxtable, J.P. Scanlon, J.J. Thresher, and A. Langsford, Nucl. Phys. **30** (1962) 475.

[Cau99a] E. Caurier, K. Langanke, and F. Nowacki G. Martínez-Pinedo, Nucl. Phys. **A653** (1999) 439–452.

[Cau99b] E Caurier, G Martinez-Pinedo, F Nowacki, A Poves, J Retamosa, and A P Zuker, Phys. Rev. **C59** (1999) 2033.

[Com] J.R. Comfort, computer program `DW81` by J.R. Comfort (1981) and updated version (1986), an extended version of `DWBA70` by R. Schaeffer and J. Raynal (1970).

[dH] M. de Huu, computer program `kinema`, unpublished.

[dH04] M. de Huu, *Experimental determination of the J^π components of the spin-dipole resonance in ^{11}B*, Ph.D. thesis, Kernfysisch Versneller Instituut, Universiteit Groningen, 2004.

[ea] D.Frekers et al., ^{64}Zn(d,^{2}He)^{64}Cu measurement at KVI, experiment nr. S51 (2005).

[Ell83] C. Ellegaard, C. Gaarde, J.S. Larson, C. Goodman, I. Bergqvist, L. Carlen, P.Ekstrom, B. Jakobsson, J. Lyttkens, M. Bedjidian, M. Chamcham, J.Y. Grossiord, A. Guichard, M. Gusakow, R. Haroutunian, J.R. Pizzi, D. Bachelier, J.L. Boyard, T. Hennino, J.C. Jourdain, M. Roy-Stephan, M. Boivin, and P. Radvanyi, Phys. Rev. Lett. **50** (1983) 1745–1748.

[Ell85] C. Ellegaard, C. Gaarde, J. S. Larsen, V. Dmitriev, O. Sushkov, C. Goodman, I. Bergqvist, A. Brockstedt, L. Carln, P. Ekstrm, M. Bedjidian, D. Contardo, J. Y. Grossiord, A. Guichard, R. Haroutunian, J. R. Pizzi, D. Bachelier, J. L. Boyard, T. Hennino, M. Roy-Stephan, M. Boivin, and P. Radvanyi, Phys. Lett. **B154** (1985) 110.

[Ere86] A. Erell, J. Alster, J. Lichtenstadt, M.A. Moinester, J.D. Bowman, M.D. Cooper, F. Irom, H.S. Matis, E. Piasetzky, and U. Sennhauser, Phys. Rev. **C34** (1986) 1822–1844.

[Fir96] R.B. Firestone and V.S. Shirley (eds.), *Table of Isotopes, 8th ed.*, Willey, New York, 1996.

[Fly72] E.R. Flynn and J.D. Garrett, Phys. Lett. **B42** (1972) 49–50.

[Fra85] M.A. Franey and W.G. Love, Phys. Rev. **C31** (1985) 488–498.

[Fuj96] M. Fujiwara, H. Akimune, I. Daito, H. Ejiri, Y. Fujita, M. B. Greenfield, M. N. Harakeh, T. Inomata, J. Jänecke, S. Nakayama, N. Takemura, A. Tamii, M. Tanaka, H. Toyokawa, and M. Yosoi, Nucl. Phys. **A599** (1996) 223c-244c.

[Fuj97] Y. Fujita, K. Hatanaka, G. P. A. Berg, K. Hosono, N. Matsuoka, S. Morinobu, T. Noro, M. Sato, K. Tamura, and H. Ueno, Nucl. Instrum. Meth. **B126** (1997) 274-278.

[Fuj99a] Y. Fujita, H. Akimune, I. Daito, Fujimura, M. Fujiwara, M.N. Harakeh, T. Inomata, J. Jänecke, K. Katori, A. Tamii, M. Tanaka, H. Ueno, and M. Yosoi, Phys. Rev. **C59** (1999) 90–100.

[Fuj99b] M. Fujiwara, H. Akimune, I. Daito, H. Fujimura, Y. Fujita, K. Hatanakaand H. Ikegami, I. Katayama, K. Nagayama, N. Matsuoka, S. Morinobu, T. Noro, M. Yoshimura, H. Sakaguchi, Y. Sakemi, A. Tamii, and M. Yosoi, Nucl. Instrum. Meth. **A422** (1999) 484.

[Fuj01a] H. Fujita, *Iospin Symmetry Structure od Spin-Isospin Excitations in A=58 Nuclei*, Ph.D. thesis, Department of Physics, Osaka University Toyonaka, Osaka 560-0043, Japan, 2001.

[Fuj01b] H. Fujita, G. P. A. Berg, Y. Fujita, Hatanaka, T. Noro, E.J. Stephenson, C.C. Foster, H. Sakaguchi, M. Itoh, T. Taki, K. Tamura, and H. Ueno, Nucl. Instrum. Meth. **A469** (2001) 55-62.

[Fuj02a] H. Fujita, Y. Fujita, G. P. A. Berg, A.D. Bacher, C.C. Foster, K. Hara, K. Hatanaka, T. Kawabata, T. Noro, H. Sakaguchi, Y. Shimbara, E.J. Shinada, E.J. Stephenson, H. Ueno, and M. Yosoi, Nucl. Instrum. Meth. **A484** (2002) 17-26.

[Fuj02b] Y. Fujita, H. Fujita, T. Adachi, G. P. A. Berg, E. Caurier, H. Fujimura, K. Hara, K. Hatanaka, Z. Janas, J. Kamiya, T. Kawabata, K. Langanke, G. Martinez-Pinedo, T. Noro, E. Roeckl, Y. Shimbara, T. Shinada, S.Y. van der Werf, M. Yoshifuku, M. Yosoi, and R.G.T. Zegers, Eur.Phys.J. **A13** (2002) 411-418.

[Fuj05] Y. Fujita, *private communication*, 2005.

[Ful80] G.M. Fuller, W.A. Fowler, and M.J. Newman, ApJS **42** (1980) 447–473, ApJS **48** (1982) 279–320; ApJ **252** (1982) 715–750; ApJ **293** (1985) 1–16.

[Gaa81] C. Gaarde, J. Rapaport, T.N. Taddeucci, C.D. Goodman, C.C. Foster, D.E. Bainum, C.A. Goulding, M.B. Greenfield, D.J. Horen, and E. Sugarbaker, Nucl. Phys. **A369** (1981) 258–280.

[Goo80] C.D. Goodman, C.A. Goulding, M.B. Greenfield, J. Rapaport, D.E. Bainum, C.C. Foster, W.G. Love, and F. Petrovich, Phys. Rev. Lett. **44** (1980) 1755–1759.

[Gre04] E.W. Grewe, C. Bumer, A.M. van den Berg, N. Blasi, B. Davids, D. De Frenne, D. Frekers, P. Haefner, M.N. Harakeh, M. Huynyadi, E. Jacobs, B. Junk, A. Korff, A. Negret, P. von Neumann-Cosel, L. Popescu, S. Rakers, , and H.J. Wrtche, Phys. Rev. **C69** (2004) 064325.

[Hag99] M. Hagemann, R. Bassini, A.M. van den Berg, F. Ellinghaus, D. Frekers, V.M. Hannen, T. Häupke, J. Heyse, E. Jacobs, M. Kirsch, B.A.M. Krüsemann, H. Sohlbach, and H.J. Wörtche, Nucl. Instrum. Meth. **A437** (1999) 459–470.

[Hag01] M. Hagemann, *Study of spin-isospin excitations in* ^{58}*Ni using the* $(d,^2\mathrm{He})$ *reaction.*, Ph.D. thesis, Vakgroep Subatomaire en Stralingsfysica, Universiteit Gent, 2001.

[Hag05] M. Hagemann, C. Bäumer, A.M. van den Berg, D. De Frenne, D. Frekers, V.M. Hannen, V.M. Harakeh, J. Heyse, M. A. de Huu, E. Jacobs, K. Langanke, G. Martnez-Pinedo, A. Negret, L. Popescu, S. Rakers, R. Schmidt, and H.J. Wörtche, Phys. Rev. C **71** (2005) 014606.

[Han01] V.M. Hannen, *A high-precision study of polarized proton scattering to low-lying states in* ^{11}B, Ph.D. thesis, Kernfysisch Versneller Instituut, Universiteit Groningen, 2001.

[Han03] V.M. Hannen, R. Bassini, A.M. van den Berg, N. Blasi, D. de Frenne, R. de Leo, F. Ellinghaus, D. Frekers, M. Hagemann, M.N. Harakeh, R. Henderson, J. Heyse, M.A. de Huu, E. Jacobs, B.A.M. Krüsemann, S. Rakers, R. Schmidt, H. Sohlbach, and H.J. Wörtche, Nucl. Instrum. Meth. **A500** (2003) 68.

[Har77] M.N. Harakeh, K. van der Borg, T. Ishimatsu, H.P. Morsch, A. Van Der Woude, and F.E. Bertrand, Phys. Rev. Lett. **38** (1977) 676–679.

[Har79] M.N. Harakeh, B. Van Heyst, K. Van Der Borg, and A. Van Der Woude, Nucl. Phys. **A327** (1979) 373–396.

[Hon96] M. Honma, T. Mizusaki, and T. Otsuka, Phys. Rev. Lett. **77** (1996) 3315-3318.

[Ike62] K. Ikeda, S. Fujii, and J.I. Fujita, Phys. Lett. **2** (1962) 169.

[Ike63] K. Ikeda, S. Fujii, and J.I. Fujita, Phys. Lett. **3** (1963) 271.

[Iro86] F. Irom, J. D. Bowman, G. O. Bolme, E. Piasetzky, U. Sennhauser, J. Alster, J. Lichtenstadt, M. Moinester, J. N. Knudson, S. H. Rokni, and E. R. Siciliano, Phys. Rev. **C34** (1986) 2231–2239.

[Jän93] J. Jänecke, K. Pham, D.A. Roberts, D. Stewart, M.N. Harakeh, G.P.A. Berg, C.C. Foster, J.E. Lisantti, R. Sawafta, E.J. Stephenson, A.M. van den Berg, S.Y. van der Werf, S.E. Muraviev, and M.H. Urin, Phys. Rev. **C48** (1993) 2828–2839.

[Kal90] C. Kalbach, Phys. Rev. **C41** (1990) 1656–1667.

[Kaw02] T. Kawabata, *Polarisation transfer in the* $^{16}O(p,p')$ *reaction at forward angles and structure of the spin-dipole resonances*, Ph.D. thesis, Department of Physics, Kyoto University Sakayo, Kyoto 606-8224, Japan, 2002.

[Knü80] W. Knüpfer, M. Dillig, and A. Richter, Phys. Lett. **B95** (1980) 349–354.

[Kox93] S. Kox, J. Carbonell, T. Motobayashi, C. Perrin, C. Wilkin, J. Arvieux, J.P. Bocquet, A. Boudard, G. Gaillard, M. Garçon, L. Ghedira, G. Guillaume, F. Merchez, D. Rebreyend, and J. Yonnet, Nucl. Phys. **A556** (1993) 621–640.

[Krü00] B.A.M. Krüsemann, R. Bassini, C. Bäumer, A.M. van den Berg, N. Dressnandt, D. Frekers, M. Hagemann, V.M. Hannen, R. Henderson, J. Heyse, E. Jacobs, M. de Huu, M. Newcomer, S. Rakers, B. Reitz, R. Schmidt, H. Sohlbach, and H.J. Wörtche, IEEE Trans. Nucl. Sci **47** (2000) 2741–2747.

[Lan99] K. Langanke and G. Martínez-Pinedo, Phys. Lett. **B453** (1999) 187–193.

[Lan00] K. Langanke and G. Martínez-Pinedo, Nucl. Phys. **A673** (2000) 481–508.

[Lan01] K. Langanke, Nucl. Phys. **A687** (2001) 303–310.

[Lis84] J. Lisantti, J. R. Tinsley, D. M. Drake, I. Bergqvist, L. W. Swenson, D. K. McDaniels, F. E. Bertrand, E. E. Gross, D. J. Horen, and T. P. Sjoreen, Phys. Lett. **B147** (1984) 23-26.

[Mai92] G. Mairle and M. Seeger, Nucl. Phys. **A593** (1992) 558–574.

[Mar83] N. Marty, C. Djalali, M. Morlet, A. Willis, J. C. Jourdain, N. Anantaraman, G. M. Crawley, and A. Galonsky, Nucl. Phys. **A396** (1983) 145–151.

[McD86] D. K. McDaniels, J. R. Tinsley, J. Lisantti, D. M. Drake, I. Bergqvist, L. W. Swenson, F. E. Bertrand, E. E. Gross, D. J. Horen, T. P. Sjoreen, R. Liljestrand, and H. Wilson, Phys. Rev. **C33** (1986) 1943–1954.

[MK94] T. Mayer-Kuckuk, *Kernphysik*, sixth ed., B.G. Teubner, 1994.

[Mor] S. Morinobu, computer program `Pfit`, unpublished.

[Nad81] A. Nadasen, P. Schwandt, P.P. Singh, W.W. Jacobs, A.D. Bacher, P.T. Debevec, M.D. Kaitchuck, and J.T. Meek, Phys. Rev. **C23** (1981) 1023–1043.

[Nak99] S. Nakayama, H. Akimune, Y. Arimoto, I. Daito, H. Fujimura, Y. Fujita, M. Fujiwara, K. Fushimi, H. Kohri, N. Koori, K. Takahisa, T. Takeuchi, A. Tamii, M. Tanaka, T. Yamagata, Y. Yamamoto, K. Yonehara, and H. Yoshida, Phys. Rev. Lett. **83** (1999) 690–693.

[NDC] http://www2.nndc.bnl.gov.

[Nor91] T. Noro, M. Fujiwara, O. Kamigaito, S. Hirata, Y. Fujita, A. Yamagoshi, T. Takahashi, H. Akimune, Y. Sakemi, M. Yosoi, H. Sakaguchi, and M. Tanaka, RCNP Annual Report (1991) 177–179.

[Oka99] H. Okamura, Phys. Rev. **C60** (1999) 064602.

[Ose79] E. Oset and M. Rho, Phys. Rev. Lett. **42** (1979) 47–50.

[Ost81] F. Osterfeld, Phys. Rev. **B105** (1981) 257.

[Ost82] F. Osterfeld, Phys. Rev. **C26** (1982) 762–765.

[Ost91] F. Osterfeld, *Giant Gamow-Teller Resonances*, Electric and Magnetic Giant Resonances in Nuclei (J.Speth, ed.), World Scientific Publishing Company, 1991, pp. 535–632.

[Ost92] F. Osterfeld, Rev. Mod. Phys. **64** (1992) 491–557.

[Ots98] T. Otsuka, M. Honma, and T. Mizusaki, Phys. Rev. Lett. **81** (1998) 1588.

[Pet80] F. Petrovich, W. G. Love, and R. J. McCarthy, Phys. Rev. **C21** (1980) 1718.

[Pet81] F. Petrovich and W. G. Love, Nucl. Phys. **A354** (1981) 499c.

[Pet86] F. Petrovich, J.A. Carr, and H.C. Manus, Annu. Rev. Nucl. Part. Sci. **36** (1986) 29.

[Rad97] P.B. Radha, D.J. Dean, S.E. Koonin, K. Langanke, and P. Vogel, Phys. Rev. **C56** (1997) 3079–3086.

[Rak02] S. Rakers, F. Ellinghaus, R. Bassini, C. Bäumer, A.M. van den Berg, D. Frekers, D. De Frenne, M. Hagemann, V.M. Hannen, M.N. Harakeh, M. Hartig, R. Henderson, J. Heyse, M.A. de Huu, E. Jacobs, M. Mielke, J.M. Schippers, R. Schmidt, S.Y. van der Werf, and H.J. Wörtche, Nucl. Instrum. Meth. **A481** (2002) 253–261.

[Rak04] S. Rakers, C. Bäumer, A.M. van den Berg, B. Davids, D. Frekers, D. De Frenne, Y. Fujita, E.-W. Grewe, P. Haefner, M.N. Harakeh, M. Hunyadi, E. Jacobs, H. Johansson, B.C. Junk, A. Korff, A. Negret, L. Popescu, H. Simon, and H.J. Wörtche, Phys. Rev. **C70** (2004) 054302.

[Ram91] S. Raman, L.W. Fagg, and R.S. Hicks, *Giant Magnetic Resonances*, Electric and Magnetic Giant Resonances in Nuclei (J.Speth, ed.), World Scientific Publishing Company, 1991, pp. 355–533.

[Rap94] J. Rapaport and E. Sugarbaker, Annu. Rev. Nucl. Part. Sci. **44** (1994) 109-153.

[Rho74] M. Rho, Nucl. Phys. **A231** (1974) 493–503.

[Ric66] P. Richard, C.F. Moore, J.A. Becker, and J.D. Fox, Phys. Rev. **145** (1966) 971–981.

[Roz80] C.M. Rozsa, D.H. Youngblood, J.D. Bronson, Y.-W. Lui, and U. Garg, Phys. Rev. **C21** (1980) 1252–1260.

[Run85] E. Runte, K.-L. Gippert, W.-D. Schmidt-Ott, P. Tidemand-Peterson, L. Ziegeler, R. Kirchner, O. Klepper, P.O. Larsson, E. Roeckl, D. Schardt, N. Kafrell, P. Peuser, M. Bernas, P. Drssagne, M. Langevin, and K.Rykaczewski, Nucl. Phys. **A441** (1985) 237.

[Sar03] P. Sarriguren, E. Moya de Guerra, and R. Álvarez Rodríguez, Nucl. Phys. **A716** (2003) 230-244.

[Sat80] G.R. Satchler, *Introduction to Nuclear Reactions*, The Macmillian Press Ltd., 1980.

[Sat83] G.R. Satchler, *Direct Nuclear Reactions*, Oxford University Press, 1983.

[Sch71] R. Schaeffer, Nucl. Phys. **A164** (1971) 145-175.

[Sch95] K. Schreckenbach, P. Liaud, R. Kossakowski, H. Nastoll, A. Bussiere, and J. P. Guillaud, Phys. Lett. **B349** (1995) 427-432.

[Sof] Open Source Software, computer program `fityk`, http://www.unipress.waw.pl/fityk.

[Str] S. Strauch and F. Neumeyer, Computer program `FIT`3.0, T.U. Darmstadt, 1996, unpublished.

[Tad87] T.N. Taddeucci, C.A. Goulding, T.A. Carey, R.C. Byrd, C.D. Goodman, C. Gaarde, J. Larsen, D. Horen, J. Rapaport, and E. Sugarbaker, Nucl. Phys. **A469** (1987) 125–172.

[Tow02] I.S. Towner and J.C. Hardy, Phys. Rev. **C66** (2002) 035501.

[vdB95] A.M. van den Berg, Nucl. Instrum. Meth. **B99** (1995) 637–640.

[vdW] S.Y. van der Werf, computer program `NORMOD`, unpublished.

[Wak] Wakasa, http://www.rcnp.osaka-u.ac.jp.

[Wak97] T. Wakasa, H. Sakai, H. Okamura, H. Otsu, S. Fujita, S. Ishida, N. Sakamoto, T. Uesaka, and Y. Satou, Phys. Rev. **C55** (1997) 2909–2922.

[Wak02] T. Wakasa, K. Hatanaka, Y. Fujita, G.P.A. Berg, H. Fujimura, M. Itoh, J. Kamiya, T. Kawabata, K. Nagayama, T. Noro, H. Sakaguchi, Y. Shimbara, H. Takeda, K. Tamura, H. Ueno, M. Uchida, M. Uraki, and M. Yosoi, Nucl. Instrum. Meth. **A482** (2002) 79–93.

[Wat86] J. W. Watson, P. J. Pella, B. D. Anderson, A. R. Baldwin, T. Chittrakorn, C. C. Foster, and I. J. Van Heerden, Phys. Lett. **B181** (1986) 47–51.

[Wer89] S.Y. Van Der Werf, S. Brandenburg, P. Grasduk, W.A. Sterrenburg, M.N. Harakeh, M.B. Greenfield, B.A. Brown, and M. Fujiwara, Nucl. Phys. **A496** (1989) 305.

[Wil82] D.H. Wilkinson, Nucl. Phys. **A377** (1982) 474.

[Wil95] A.L. Williams, W.P. Alford, E. Brash, B.A. Brown, S. Burzynski, H.T. Fortune, O. Husser, R. Helmer, R. Henderson, P.P. Hui, K.P. Jackson, B. Larson, M.G. McKinzie, D.A. Smith, A. Trudel, and M. Vetterli, Phys. Rev. **C51** (1995) 1144.

[Yam95] T. Yamagata, H. Utsunomiya, M. Tanaka, S. Nakayama, N. Koori, A. Tamii, Y. Fujita, K. Katori, M. Inoue, M. Fujiwara, and H. Ogata, Nucl. Phys. **A589** (1995) 425.

[You77] D.H. Youngblood, C.M. Rozsa, J.M. Moss, D.R. Brown, and J.D. Bronson, Phys. Rev. Lett. **39** (1977) 1188–1191.

[You81] D.H. Youngblood, P. Bogucki, J.D. Bronsonand U. Garg, Y.-W. Lui, and C.M. Rozsa, Phys. Rev. **C23** (1981) 1997–2007.

[Zeg00] R.G.T. Zegers, A.M. van den Berg, S. Brandenburg, F.R.R. Fleurot, M. Fujiwara, J. Guillot, V.M. Hannen, M.N. Harakeh, H. Laurent, K. van der Schaaf, S.Y. van der Werf, A. Willis, and H.W. Wilschut, Phys. Rev. Lett. **84** (2000) 3779–3782.

[Zeg03] R.G.T. Zegers, H. Abend, H. Akimune, A.M. van den Berg, H. Fujimura, H. Fujita, Y. Fujita, M. Fujiwara, G. Gales, K. Hara, M.N. Harakeh, T. Ishikawa, T. Kawabata, K. Kawase, T. Mibe, K. Nakanishi, S. Nakayama, H. Toyokawa, M. Uchida, T. Yamagata, K. Yamasaki, and M. Yosoi, Phys. Rev. Lett. **90** (2003) 202501.

Acknowledgements

First of all I would like to express my gratitude to my promoters Prof. Dr. Etienne Jacobs and Prof. Dr. Denis De Frenne for giving me the best opportunities to work and study in an international environment. Nothing would have been possible without their confidence in me. They have been not only my promoters, but also my English teachers and friends. I will always appreciate their guidance and kindness.

For the very helpful discussions and advices regarding the data analysis I want to thank also to other professors: Yoshitaka Fujita, Heinrich Wörtche, Dieter Frekers, Peter von Brentano, Kris Heyde, Cyrillus Wagemans and Georg Berg. For the experimental part of this work I would like to thank Dr. Ad van den Berg and Prof. Kichiji Hatanaka: due to their beam tuning the energy resolution achieved in the two experiments was unprecedented.

For various discussions facilitating me the understanding of several important physics aspects, I want to thank my colleague, Alexandru Negreţ. I thank Markus Hagemann (who showed me the first steps on the $(d,{}^2\mathrm{He})$ data analysis technique) and my other close colleagues from Ghent: Nadia Smirnovna, Jan Heyse, Liesbeth De Smet and Sofie Vermote.

These experiments could not have been done without the help of my colleagues from Münster, Groningen, Darmstadt, Osaka and Cape Town. I wish to thank Christian Bäumer, Eike Grewe, Petra Haefner, Björn Junk, Andreas Korff, Sven Rakers, Matyas Hunyadi, Marc de Huu, Hakon Johansson, Natasha Ryezayeva and Artem Shevchenko who helped me during the $(d,{}^2\mathrm{He})$ experiment. For the $({}^3\mathrm{He},t)$ experiment, I had the help of the Japanese collaborators. I want to mention especially Tatsuya Adachi, Kousuke Nakanishi, Yoshihiro Shimbara, Atsushi Tamii and Masaru Yosoi. I am grateful to Prof. Atsushi Tamii and Prof. Yoshitaka Fujita for giving the opportunity to perform the (p,p') test measurement in RCNP. I thank Hiroaki Matsubara for his help with translating different discussions and experimental notes written in Japanese. I want to thank also the collaborators from South Africa, where the second (p,p') test measurement was performed: Ricky Smit, John Carter,

Siegfrid Förtsch, Hirohiko Fujita and Retief Neveling.

My stay in Japan was extremely pleasant especially due to Prof. Yoshitaka Fujita, who accompanied me and my colleague in many excursions giving us the feeling of what Japan means. I want to thank also Keiko Yamamura, Yumiko Maeda, Arisa Nakanishi and Natsuko Arimoto for their kindness and friendship.

Although far from Romania, I could feel at home due to my Romanian friends in Ghent. I thank all of them for this atmosphere.

Vreau să mulţumesc parinţilor mei pentru efortul continuu de a-mi asigura cele mai bune condiţii de studiu. Încrederea lor în posibilităţile mele a fost un real suport. Vreau să mulţumesc sorei mele, Oana, precum şi întregii familii, care mi-a fost aproape încurajându-mă în toţi aceşti ani.

Finally, I want to express my special gratitude to my husband, Radu, for his invaluable help, patience, encouragement and respect of my studies. Without his help I would have never been able to complete this work.